Towards online MRI-guided radiotherapy

Gijsbert H. Bol

Cover:
Abstract version of Figure 6.3a of this thesis, created by Heike Kleinjan

Manuscript:
Layout: G.H. Bol, using LaTeX 2_ε typesetting
Printed by: Ipskamp Drukkers
ISBN: 978-90-393-6313-3

Financial support for publication of this thesis was kindly provided by Elekta B.V., Philips Healthcare, and Röntgenstichting Utrecht.

Towards online MRI-guided radiotherapy

Op weg naar online MRI-gestuurde radiotherapie

(met een samenvatting in het Nederlands)

Proefschrift

ter verkrijging van de graad van doctor aan de
Universiteit Utrecht
op gezag van de rector magnificus, prof. dr. G.J. van der Zwaan,
ingevolge het besluit van het college voor promoties
in het openbaar te verdedigen
op donderdag 25 juni 2015 des middags om 12.45 uur

door
Gijsbert Herman Bol
geboren op 13 maart 1979 te Meerkerk

Promotoren: Prof. dr. ir. J.J.W. Lagendijk
Prof. dr. B.W. Raaymakers

Contents

Acronyms

APMM Averaged Projection Matching Method

BFFE Balanced Fast Field Echo

bSSFP balanced Steady State Free Precession

CBCT Cone-Beam Computed Tomography

CPU Central Processing Unit

CTV Clinical Target Volume

CT Computed Tomography

DAO Direct Aperture Optimization

DICOM Digital Imaging and Communications in Medicine

DIWA Dynamic Importance Weight Assignment

DMPO Direct Machine Parameter Optimization

DRR Digitally Reconstructed Radiographs

DVH Dose Volume Histogram

EPID Electronic Portal Imaging Device

ERE Electron Return Effect

ESTRO European SocieTy for Radiotherapy and Oncology

FFF Flatting Filter Free

FIDO Fast Inverse Dose Optimization

FMEA Failure Mode and Effects Analysis

GPUMCD GPU Monte-Carlo Dose engine

GPU Graphical Processing Unit

GTV Gross Target Volume

HIFU High-Intensity Focused Ultrasound

IMRT Intensity Modulated RadioTherapy

kV kiloVoltage

MLC Multi-Leaf Collimator

MRI Magnetic Resonance Imaging

MRLTP MRL Treatment Planning system

MRL MRi Linear accelerator

MU Monitor Units

MV MegaVoltage

NEMA National Electrical Manufactures Association

NMI Normalized Mutual Information

OAR Organs At Risk

PET Positron Emission Tomography

PTV Planning Target Volume

QA Quality Assurance

RF Radio Frequency

RMI Relative Modulation Index

RPM Rotations Per Minute

RTT Radiation TherapisT

SD Standard Deviation

SE Spin Echo

SMM Stack Matching Method

SNR Signal-to-Noise Ratio

SWO Segment Weight Optimization

TE Echo Time

TPS Treatment Planning System

TR Repetition Time

TSE Turbo Spin Echo

VCS Virtual Couch Shift

VMAT Volumetric Modulated Arc Therapy

VOI Volumes Of Interest

1

General introduction

1.1 Introducing radiotherapy

Radiotherapy, or radiation therapy, aims to destroy malignant cells while sparing the surrounding tissue as much as possible. In order to achieve this goal, the tumor region is irradiated using ionizing radiation. Radiation can be delivered by implanting small radioactive sources in the patient (brachytherapy) or via external radiation beams. In this thesis we will focus on photon radiation which is produced externally by a mega-voltage (MV) linear accelerator or linac. This type of irradiation is most commonly used in the radiotherapy field, but electrons, protons, neutrons or heavy ions can also be used to deliver external radiation therapy.

In current clinical practice, a complete radiation treatment can be roughly divided in three sequential parts:

- Treatment preparation
- Treatment planning
- Treatment delivery

The next sections will briefly describe each component.

1.1.1 Treatment preparation: targets and organs-at-risk definition

When preparing a patient for treatment, a computed tomography (CT) scan is acquired to visualize patient anatomy. On this so-called planning CT, physicians delineate the tumor and the surrounding healthy organs-at-risk (OAR). In some cases, the positions of (implanted) fiducial markers are also delineated. These markers can later be used to verify the position of the tumor during treatment delivery.

Figure 1.1a and 1.1b respectively show typical CT-based delineations for a rectal cancer patient and a prostate cancer patient. The visible tumor tissue is also known as gross target volume (GTV). The area around the GTV is called the clinical target volume (CTV). The CTV is generated by adding a margin to the GTV to include microscopic

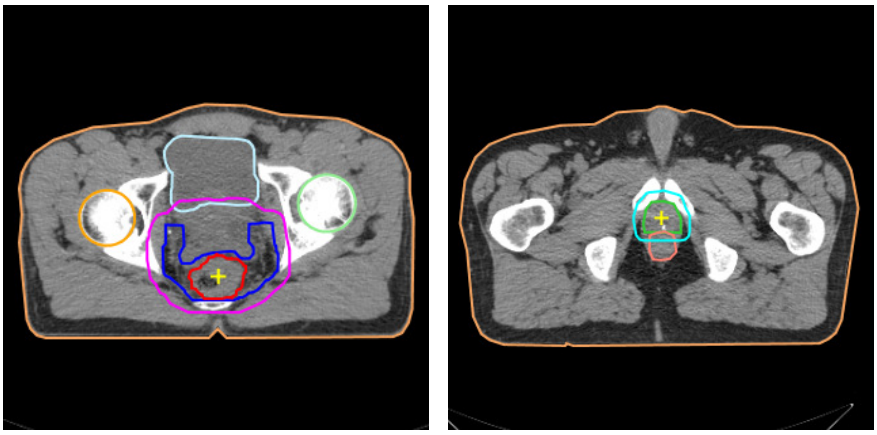

(a) CT-based rectum delineation (b) CT-based prostate delineation

Figure 1.1: Delineations of a rectal and prostate cancer patient on CT. The tumor volumes are indicated by the yellow cross. Also the OAR are delineated. Just below the yellow marker in the prostate case, an implanted fiducial marker is visible in white. For the rectal case the GTV is outlined in red, the CTV in blue and the PTV in magenta. For the prostate case, the GTV/CTV is shown in green and the PTV in light blue.

tumor infiltration and therefore has to be treated as well (ICRU Report No. 50, 1993). For the prostate case (Figure 1.1b) the GTV and the CTV are exactly the same structure. For both cases an additional margin has been applied to account for organ motion, delineation inaccuracies and patient setup errors. This planning target volume (PTV) is generated to ensure that the CTV receives the intended dose. The PTV is created by adding a three-dimensional margin around the CTV, ranging between a few millimeters up to centimeters. The exact margin is usually determined on population statistics (Van Herk *et al.*, 2000). Obviously, this approach results in the irradiation of regions containing much healthy tissue, which increases the risk of toxicity and therefore limits the dose that can be delivered to the tumor.

Motion characteristics can also be used to define targets and OAR. In current clinical practice, four-dimensional CT (4D-CT) (Low *et al.*, 2003; Ford *et al.*, 2003; Keall, 2004) can be used to study and quantify these characteristics. For example, based on such knowledge, the mid-ventilation position and the appropriate parameters for non-uniform margins for lung tumors can be derived (Wolthaus *et al.*, 2008; Hughes *et al.*, 2008).

1.1.2 Treatment planning

After defining the targets and the OAR in the treatment preparation phase, the treatment planning phase starts. The aim of this step is to create a treatment plan which delivers the desired dose to the PTV while at the same time makes sure that the dose tolerances of the OAR are not exceeded. In current clinical practice, treatment plans

are created using treatment planning systems (TPS). One of the main components of a TPS is the dose engine. A dose engine can calculate the delivered dose to the patient, given a set of beam characteristics, such as energy, angle, shape, and intensity profiles, and the electron densities of the patient anatomy. The electron densities of a patient are derived from the planning CT via a calibration curve. A TPS usually supports multiple radiation techniques, such as conformal radiation therapy and/or intensity modulated radiotherapy (IMRT) (Webb, 2005).

With conformal radiation therapy, multiple beams are delivered to the patient using an uniform beam profile for each beam. The shape of each beam can be modified using the multi-leaf collimator (MLC) mounted on the linear accelerator. Optimization of beam angles, shapes and profiles involves usually a trial-and-error procedure, which is highly dependent on the skill of the human operator.

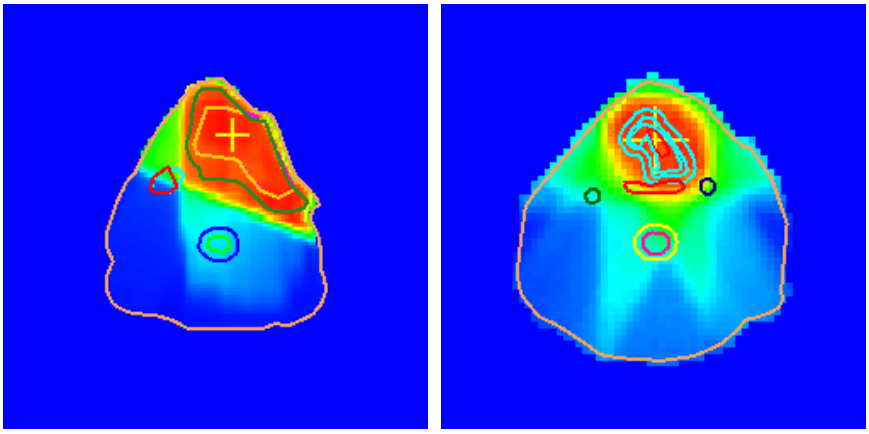

(a) Conventional head-and-neck plan (b) IMRT head-and-neck plan

Figure 1.2: Dose distributions after treatment planning for two head-and-neck patients. On the left a conventionally optimized plan and on the right a plan optimized using IMRT.

IMRT adds degrees of freedom to the optimization by allowing non-uniform beam profiles. This often allows better sparing of the OAR while maintaining or increasing the dose to the tumor. Furthermore inverse planning is used, rather than forward planning as used by conformal radiation therapy. The operator defines a set of dose objectives for the tumor regions and dose constraints for the OAR and the TPS tries to optimize the beam profiles in such a way that all objectives and constraints are met. Figure 1.2 illustrates the main difference between the two radiation techniques: the high dose region of the IMRT plan (as shown on the right image) is better conformed to the tumor volume compared to the dose distribution resulting from the conformal radiation technique. This lowers the dose to neighboring OAR, which can lead to a lower toxicity rate for a given tumor dose, or to an equivalent toxicity rate for an increased tumor dose.

The total dose to the tumor is usually not delivered in one treatment session, but in a fractionated fashion which allows healthy tissue to recover in between fractions. The

dose per fraction typically ranges from $1.5\ \mathrm{Gy}$ to $2.5\ \mathrm{Gy}$ for these fractionated treatment schemes. In current clinical practice a single treatment plan is used for all fractions. This means that all the uncertainties over the course of the treatment have to be incorporated into the PTV margin. In order to reduce the PTV margin, the "library of plans" concept was introduced (Murthy *et al.*, 2011). Instead of creating a single treatment plan, multiple treatment plans are generated for different anatomical configurations that can occur during treatment. By selecting the most appropriate one each day (i.e. the one that best matches the patient anatomy recorded that day), the PTV margin for each individual plan can be reduced.

1.1.3 Treatment delivery

After a treatment plan is approved by the physician, it is transferred to the linear accelerator for treatment delivery. Before each fraction, the patient has to be positioned as close as possible to the position on which the treatment plan was created. In order to do so, the patient is positioned on the treatment table guided by markers that are tattooed on the skin, which are linked to the coordinate system of the planning CT. Obviously, the tumor area will move relative to the skin markers and therefore additional position verification techniques have been developed to ensure the correct position of the tumor relative to the treatment beams.

One of the oldest position verification tools available is portal imaging. Portal imaging uses the treatment beam itself to visualize patient anatomy via a flat panel imager mounted opposite to the megavoltage (MV) source of the linear accelerator. The acquired MV transmission images have, however, fairly low contrast, which makes portal imaging only suitable for visualizing bones, high density landmarks or implanted fiducial gold markers (see Figure 1.3). By comparing the MV images with the digitally reconstructed radiographs (DRR) calculated from the planning CT, the position of the bony anatomy, the landmarks or the fiducial markers can be verified (Nederveen *et al.*, 2003; Van der Heide *et al.*, 2007).

A kilovoltage (kV) rather than a MV photon source can also be used for generating images for position verification. Due to the lower photon energies, kV images can show better contrast between low density tissues than MV images. The kV source is usually mounted on the gantry of the linear accelerator, orthogonal to the MV radiation source. A flat panel detector opposite to the kV source is used to digitally obtain the transmission images. Although the transmission images can be used directly for position verification purposes, the images are mainly used for volumetric reconstruction of the patient anatomy i.e. cone-beam computed tomography (CBCT). The CBCT dataset shows soft tissue landmarks that can be used for position verification purposes, but the image quality is generally not as good as that of a free-standing CT system (see Figure 1.4).

From all of the above position verification modalities, translational and rotational displacement vectors can be derived, which are the input for various patient set-up correction protocols (Bel *et al.*, 1993; De Boer *et al.*, 2001a). These protocols can be applied in an online or offline fashion. The online set-up correction protocols apply the calculated

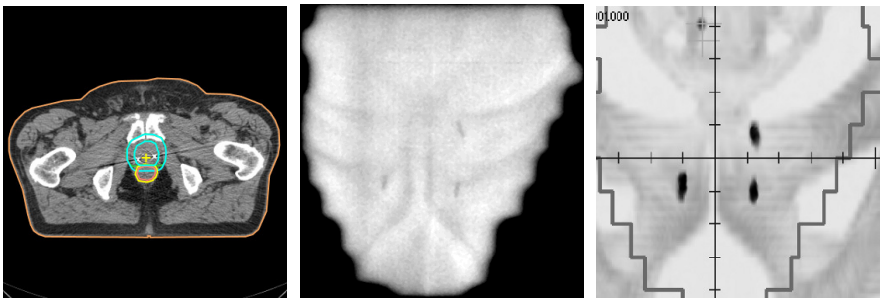

(a) Planning CT (b) Portal image (c) DRR image

Figure 1.3: On the left image the planning CT of a prostate cancer patient. Inside the prostate two of the three implanted fiducial gold marker are clearly visible on both sides of the yellow cross. On the middle image a portal image is showed. Besides bony structures, the three implanted fiducial gold markers are visible. The calculated DRR is shown on the right. This image also includes the outline of the treatment field.

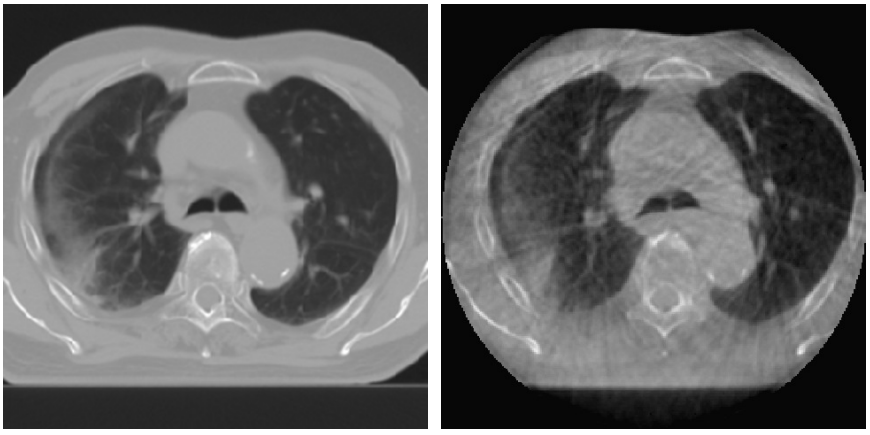

(a) Free-standing CT (b) CBCT

Figure 1.4: Contrast differences between a transversal free-standing CT and a CBCT image of a lung cancer patient. For clarity the free-standing CT image has been cropped approximately to the same field of view (FOV) as the CBCT.

patient displacement vectors directly to the patient before the actual fraction delivery starts. The offline protocols are used to implement patient displacement vectors for future fractions based on information gathered from previous fractions.

The calculated setup corrections are applied by moving the treatment couch in such a way that the location of the target volume matches the location in the treatment plan. Nowadays, it is possible to translate and rotate the treatment couch along and about the three principal axes whereas in the past only translations could be applied. However, the rotational corrections are limited to 3° in each direction for reasons of patient safety (Linthout *et al.*, 2007).

After positioning the patient, the radiation treatment is delivered to the patient, according to the pre-calculated treatment plan.

1.2 Offline MRI-aided radiotherapy

In the previous section we described how a typical radiotherapy treatment is implemented in current clinical practice. We have seen that image modalities based on photon attenuation differences are used extensively throughout the treatment. The planning CT plays a prominent role, as it is used for tumor delineation and accurate dose calculation and serves as a reference for position verification. However, one of the major drawbacks of CT is its limited soft tissue contrast compared to another major imaging modality: magnetic resonance imaging (MRI) (Brown *et al.*, 2014).

MRI uses magnetic fields and radio frequency (RF) pulses to form images of the patient anatomy, but also functional information can be obtained. The patient is placed in a strong magnet (typically ranging between 0.2 T and 7 T), and a RF pulse at the appropriate resonant frequency is applied. The excited hydrogen atoms re-emit the radio signal which is measured by a receiver coil. The contrast between different tissues is determined by the rate at which excited atoms return to the equilibrium state. Exogenous contrast agents may be given intravenously, orally or intra-articularly.

Figure 1.5 shows a typical example of the contrast differences between CT and MRI of a patient with a benign brain tumor. Compared to CT, MRI has more modes of operation. By varying its numerous parameters, a MRI sequence can be tailored to visualize different aspects of the tumor at hand, such as cell density, tissue oxygenation and perfusion. Since MRI does not use ionizing radiation, MRI sequences can be repeated without increasing the patient radiation burden.

MRI is not only very suitable for visualizing the tumor and the OAR during the preparation phase of a classical radiotherapy treatment scheme, the cine-MRI sequences allow assessment of the tumor movement, and this information can be used to determine the “average” tumor position and the accompanying patient specific PTV margin (Feng *et al.*, 2009). MRI is also very useful for assessing tumor response during and after treatment.

Although MRI provides better soft-tissue contrast, it currently does not provide the elec-

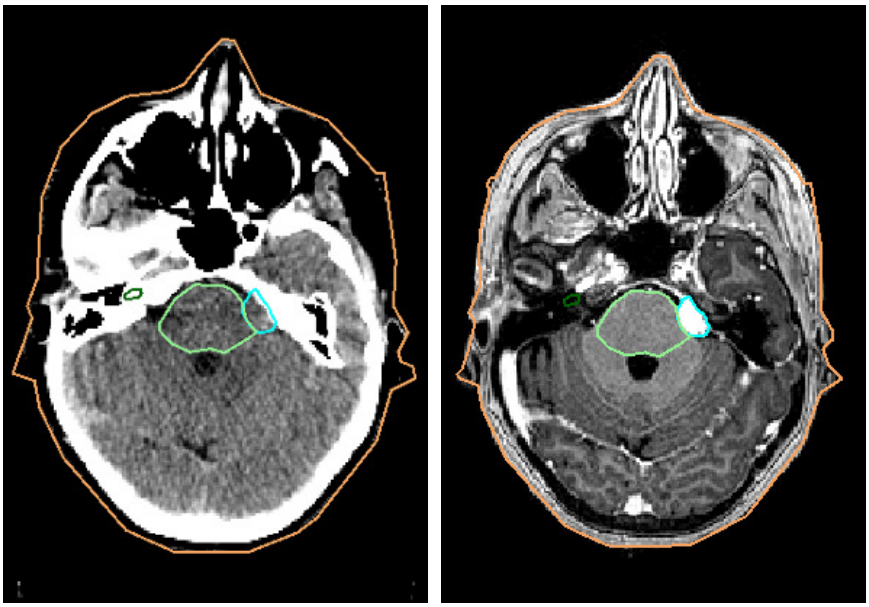

(a) CT brain (b) MRI brain

Figure 1.5: CT and a T1 3D TFE MRI scan of a patient with vestibular schwannoma. The tumor (delineated in light blue) is clearly visible on the MRI, while it is not visible on CT. Also the OAR brainstem (light green) and cochlea (dark green) are delineated.

tron density information needed for accurate dose calculation. As a surrogate, the MRI sequences are still registered to a planning CT and the MRI-based delineations are transferred to the planning CT accordingly before being used by a TPS. Furthermore, MRI can suffer from geometric and intensity distortions (Bakker *et al.*, 1992; Moerland *et al.*, 1995).

1.3 Towards online MRI-guided radiotherapy

Until now we have described how MRI adds value to current clinical practice, without considerable changes of the overall treatment regime. If we want to exploit the capabilities of MRI to the fullest, a radical treatment regime change is needed. Instead of using MRI as just a "CT-with-better-contrast" modality, online MRI-guided treatment delivery should be the next step to improve the effectiveness of external beam radiotherapy as a cancer therapy. The fact that MRI can acquire 2D and 3D datasets along arbitrary axes, and can depict patient anatomy changes within milliseconds using cine-MRI sequences, makes this modality the prime candidate to monitor treatment delivery and enable treatment adaptation on an inter- and intrafraction timescale. This means that the classical offline treatment preparation and planning phase should be integrated into the treatment delivery phase. We will discuss this in more detail in the general discussion chapter (Chapter 9) of this thesis.

Research developments towards online MRI-guided radiotherapy are underway with the installation of a "next door" 1.5 T MRI system, as described by Karlsson *et al.* (2009). The patient can be transported during treatment from the linac to the MRI and back with a custom made trolley. Another system, especially built for neurosurgery by IMRIS Inc (Winnipeg, Canada), has a rail-mounted MRI which can be moved in or out of the radiotherapy treatment room. Both systems are conceptually similar to the in-room CT solution, except that the MRI provides superior soft tissue contrast. However, since the patient has to be moved between the imaging modality and the treatment machine, the risk of geometrical errors is increased and obviously these systems cannot be used to provide direct feedback during treatment delivery.

To overcome these shortcomings, an integrated MRI system has been proposed by Lagendijk *et al.* (2000). The Cross Cancer Institute (Edmonton, Canada) constructed the prototype system which consists of a bi-planar 0.2 T permanent MRI system and a 6 MV linear accelerator. The linac is mounted on the open end of the MRI magnet. The system is capable of capturing MRI images during irradiation as described by Fallone *et al.* (2009). Installation of the second system began in 2013. This has an isocentrically mounted 6 MV linac that rotates in-unison with a biplanar 0.5 T MRI in transverse plane. Viewray Inc (Cleveland, USA) has developed the first commercially available integrated MRI system: it consists of a open 0.35 T MRI scanner combined with three ^{60}Co sources which can rotate axially around the patient (Dempsey *et al.*, 2005).

At our department, in cooperation with Elekta and Philips, a MRI linear accelerator (MRL) is being developed (Lagendijk *et al.*, 2008). It integrates a modified, diagnostic 1.5 T MRI scanner (Philips, Best, The Netherlands) with a 7.2 MV linear accelerator (Elekta AB, Stockholm, Sweden). The linac is mounted on a ring surrounding the MRI and the radiation beam passes through the bore of the MRI before entering the patient. After the construction of the working prototype with a static gantry and fixed collimator blocks (Figure 1.6a), the machine was upgraded with a rotating gantry, which can rotate at a maximum speed of 10 RPM, and a fully functional 80 leaf pair MLC (Figure 1.6b). The gantry is also equipped with an electronic portal imaging device (EPID) (Raaymakers *et al.*, 2011). With these systems we showed that the MRI images of the MRL are comparable to images of standard 1.5 T stand-alone MRI scanners, even when the linear accelerator is turned on (Raaymakers *et al.*, 2009). The MRL can also deliver IMRT plans and supports gating and tracking (Crijns *et al.*, 2011, 2012b). Currently, a second clinical grade prototype MRL is being installed at our department (see Figure 1.6c).

Besides the numerous engineering challenges which have to be overcome in order to integrate the MRI, with its strong magnetic field, with the magnetic field sensitive electronics of the linear accelerator, the influence of the magnetic field on the delivered dose distribution is also of great importance. Due to the presence of a transverse magnetic field, the radiation beam has a decreased build-up distance and a shifted, asymmetrical penumbra (Raaymakers *et al.*, 2004). Even more importantly, electrons leaving the tissue traverse an arc-shaped path back into the tissue, which results in a increased dose at tissue-air interfaces (Raaijmakers *et al.*, 2005a). This electron return effect (ERE)

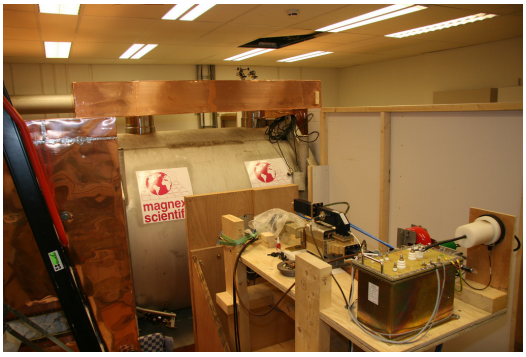

(a) MRL with static gantry and fixed collimator blocks

(b) MRL with rotating gantry and MLC

(c) Clinical grade MRL

Figure 1.6: UMC Utrecht MRL versions overview

and the reduced build-up distance depend profoundly on the entrance or exit surface orientation, as described by Raaijmakers *et al.* (2007b). They also demonstrated that a first order compensation of ERE around a static air cavity can be accomplished by using opposing beams. Additional ERE compensation can be achieved by using IMRT (Raaijmakers *et al.*, 2007a).

1.4 Thesis outline

The first part of this thesis addresses improvements to patient position verification and to the use of MRI in radiotherapy achievable under the classical radiotherapy scheme. The second part of the thesis will focus on developing treatment planning techniques and regimes which will eventually lead to the online use of the MRL, and we will investigate the behavior of ERE in the case of non-stationary air cavities.

Chapter 2 describes how automatic offline patient position verification using MV images can be dosimetrically improved by using the series of IMRT treatment segments instead of using extra position verification fields, even if every individual portal image of each segment does not contain sufficient matching information. Chapter 3 and 4 describe how MRI can be integrated into the treatment preparation and delivery phase. Chapter 3 outlines a framework which allows the physician to use multiple MRI sequences and other modalities such as positron emission tomography (PET) besides the standard planning CT for tumor and OAR delineation. Under this framework, the image datasets are always displayed in their original form and delineation can take place on all orthogonal views of each dataset, while providing direct feedback to the delineator on all other datasets. Chapter 4 introduces a new fiducial gold marker which can be detected on various MRI sequences, while the standard, pure gold markers are poorly visible on MRI. The new marker consists of a steel core (which provides visibility on MRI) within a gold casing (visible on MV images). We show that these markers for prostate cancer patients can be detected with the same accuracy on MRI as on CT, and therefore the planning CT is no longer essential for marker detection.

Chapters 5, 6 and 7 focus on online treatment planning for the MRL and the dosimetric effects of non-stationary air cavities on dose distributions in magnetic fields. In chapter 5 an IMRT optimization system called MRLTP (MRL Treatment Planning system) is introduced which combines a Monte-Carlo dose calculation engine and an inverse dose optimization algorithm. MRLTP can generate tightly conformal IMRT plans in both 0 T and 1.5 T environments and is fast enough for online IMRT planning. In chapter 6 we use MRLTP to study possible ERE effects of non-stationary spherical air cavities on IMRT dose delivery in 0.35 T and 1.5 T transverse magnetic fields. The goal was to verify the robustness of an IMRT treatment in a magnetic field, so random air cavity movements and baseline shifts, both inter- and intrafraction are investigated. Furthermore, the intrafraction effects of appearing or disappearing air cavities are described. In chapter 7, we introduce the online "virtual couch shift" (VCS) concept: we translate and/or rotate the pre-treatment dose distribution to compensate for the changes in patient anatomy and, with MRLTP, generate a new plan which delivers the transformed dose distribution automatically. The VCS is the first step towards compensating for all anatomical changes by online IMRT re-optimization.

Chapter 8 summarizes this thesis and chapter 9 discusses how MRL based radiotherapy could be implemented. This chapter will also discuss specific details within this new regime such as image segmentation, treatment planning and quality assurance (QA).

2

Patient position verification using small IMRT fields

This chapter is based on:
Bol G.H., Van der Heide U.A., Nederveen A.J., Kotte A.N.T.J. and Lagendijk J.J.W. 2006 Patient position verification using small IMRT fields *Medical Physics* **33** 2344–2353

Abstract

A commonly used approach to quantify and minimize patient setup errors is by using electronic portal imaging devices (EPIDs). The position of the tumor can be verified indirectly by matching the bony anatomy to a reference image containing the same structures. In this paper we present two off-line methods for detecting the position of the bony anatomy automatically, even if every single portal image of each segment of an (IMRT) treatment beam contains insufficient matching information. Extra position verification fields will no longer be necessary, which speeds up the treatment and reduces the total dose to the patient. The first method, the stack matching method (SMM), stacks the portal image of each segment of a beam to a 3D volume and this volume is subsequently used during the matching phase. The second method (the averaged projection matching method (APMM)), is a simplification of the first one, since the initially created volume is reduced again to a 2D artificial image, which speeds up the matching procedure considerably, without significant loss of accuracy. Matching is based on normalized mutual information. We demonstrate our methods by comparing them to existing matching routines, such as matching based on the largest segment. Both phantom and patient experiments show that our methods are comparable with the results obtained from standard position verification methods. The matches are verified by means of visual inspection. Furthermore, we show that when an distinct area of 40 to 60 cm^2 of the EPID is exposed during one treatment beam, both SMM and APMM are able to deliver a good matching result.

2.1 Introduction

A commonly used approach to quantify and minimize patient setup errors is by using electronic portal imaging devices (EPIDs) (Antonuk, 2002). The position of the tumor can be verified indirectly by matching the bony anatomy to a reference image containing the same structures. The reference image is usually a digitally reconstructed

radiograph (DRR) or a simulator image (Gilhuijs *et al.*, 1996). When the individual portal images are too small or do not contain enough matching information, additional large rectangular fields are added to the treatment for patient position verification purposes only (De Boer *et al.*, 2001b; Van Lin *et al.*, 2003). These fields add extra dose to the patient and distort the initial treatment dose distribution. For conformal treatment planning, the dose distribution distortions inside the target volume can be compensated by changing the beam weights and wedge angles of the original treatment (Meijer *et al.*, 2000), but still the tissue outside the target volume receives more dose than strictly necessary.

With the introduction of intensity-modulated radiotherapy (IMRT), the delivery of an even more conformal dose to target volumes became possible, while sparing the surrounding organs and tissues at risk (Webb, 2001; Nutting *et al.*, 2000). However, due to geometric uncertainties such as organ motion and setup errors, the potential benefits of IMRT (dose escalation in the target and margin reduction) can get compromised. Therefore, good patient position verification procedures are essential for successfully exploiting the benefits of IMRT (Jaffray *et al.*, 1999; Langen *et al.*, 2001). Also in this case, large rectangular fields are often added to the treatment for positioning purposes only, but usually during treatment planning no attention is given to the dose distribution distortions they cause.

In this paper we present two off-line methods for detecting the position of the bony anatomy automatically, even if every single portal image of each segment of an (IMRT) treatment beam contains insufficient matching information. By using a combination of each image of every beam segment instead of just the first or the largest one, a more robust registration is made. Extra position verification fields will no longer be necessary, which reduces the total dose to the patient. Combining segments has been described earlier (Fielding *et al.*, 2004). All segments were added up to create an artificial 2D image. However, in this case special calibration methods had to be applied to remove the intensity modulations of the beam. We show that our methods avoid the problems regarding artifacts due to fluence variations in the field and at the penumbra. Furthermore, due to their straightforward nature, our methods can be applied to every beam of each treatment. Even if for instance the first segment of a plan sequenced with a "close in" technique contains enough matching information, the usage of all available segments can make the resulting registration more robust.

The basis of the first method, the stack matching method (SMM), is that the portal images after some initial preprocessing steps, are stacked to a 3D volume and this volume is subsequently used during the matching phase. Our second method (the averaged projection matching method (APMM)), is a simplification of the first one, since the created volume is reduced again to a 2D artificial image by a form of projection, which speeds up the matching procedure considerably, without significant loss of accuracy. We use normalized mutual information as our primary similarity measure, which is a well-known intensity-based registration method (Wells *et al.*, 1996; Maes *et al.*, 1997).

2.2 Materials and Methods

2.2.1 Image processing

The portal images were taken with an a-Si flat-panel imager (Elekta *i*View GT, Elekta Oncology Systems Ltd, Crawley, UK) that was mounted on the linac (SLi15, Elekta Oncology Systems Ltd, Crawley, UK). The imaging area at isocenter is 26×26 cm and has 1024×1024 pixels, which corresponds to a spacial resolution of 0.25 mm. An internal copper plate of 1 mm thickness acts as build-up material (Winkler *et al.*, 2005).

Before performing our experiments, the pixel value behavior of the EPID images as produced by the *i*View GT software was investigated. The main purpose of these tests was to assess the possible pixel value effects of the build-in pixel-based normalization routines of the software with respect to reproducibility, frame averaging, and different field sizes. First the reproducibility was tested by delivering multiple 10×10 cm 6 MV fields of 5 monitor units (MU). The second test consisted of delivering 10×10 cm 6 MV fields while varying the MU from 2 to 20 using both maximal frame averaging and no frame averaging. The results of these tests are depicted in Figure 2.1a and 2.1b. Both tests showed that the value of the center pixel was stable since all standard deviations are well below one percent of the mean pixel value (presented in Table 2.1) as long as maximal frame averaging is used. This all means that the portal images are normalized in the *i*View GT software and therefore do not need to be normalized afterwards with respect to the number of monitor units and time between segments. The third test has been performed in order to verify the pixel value stability when having different field sizes. Again, 6 MV, 5 MU beams with field sizes from 1×1 cm to 20×20 cm were captured, leading to the graph depicted in Figure 2.1c. It is clear that as long as the segments are sufficiently large (larger than 2×2 cm) the pixel values returned by the EPID are stable enough and no further normalization is needed. We expected this result, since it is known that the normalization taking place in the *i*View GT software does not work well on small fields. Note that the mean and standard deviation regarding this test in Table 2.1, are calculated without the results of the first two measurements obtained from the two smallest segments.

The DRRs used in this paper have been calculated by our treatment planning system (PLATO RTS 3.6, Nucletron Ltd, Veenendaal, NL) from planning CTs which had an in plane pixel resolution of 0.82×0.82 mm and a slice thickness of 2 or 3 mm.

All image processing routines applied on the EPID images (after they were exported from the vendor software), and the software needed for image registration using normalized mutual information was developed within our department.

2.2.2 Stack matching method (SMM)

The stack matching method starts with the imaging of all segments of a single IMRT beam. All segments with an area smaller than 4 cm^2 are removed, because the portals of these segments are expected to be unstable with respect to pixel values as described in the previous section. After this, every field edge calculated by the planning system is matched on each corresponding imaged segment, using a field edge matching algo-

Test	*Mean pixel value*	*1 SD (percentage)*
Reproducibility	34757	182 (0.52%)
Different MU (no frame averaging)	34267	435 (1.27%)
Different MU (max frame averaging)	34875	184 (0.52%)
Different field sizes	34716	268 (0.77%)

Table 2.1: The results of the different EPID pixel stability tests. Both the mean pixel value and the standard deviation is presented.

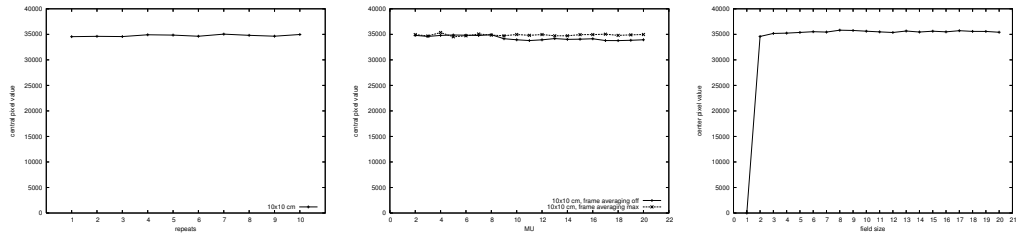

(a) (b) (c)

Figure 2.1: EPID pixel value stability regarding reproducibility (a), frame averaging on/off and number of MU (b), and different field sizes (c).

rithm based on narrow band registration (Ng *et al.*, 2003), to remove any (systematic) misalignment of the EPID and the linac. Such a misalignment is usually caused by the fact that the panel is manually positioned at the beginning of a treatment session. We now have a geometrical relation between the portal image, the field edge and the isocenter, since the position of the isocenter relative to the field edge is known from the planning system data. With this information we can remove the penumbra artifacts by masking out everything that is outside the field edge, along with every pixel that is within 5 mm inside the field edge. Next, each cropped image is display equalized (Moseley *et al.*, 1993) and binned into 64 bins (Hill *et al.*, 2001). The discretization fault introduced by the binning step (each bin contains 1.56 percent of total pixel range) is in the same range as the stability of the EPID as shown in Table 2.1. The 2D preprocessed images are then stacked to a 3D volume as shown in Figure 2.2a. The x- and y-coordinate of the origin of the volume is set to isocenter and the z-coordinate is set to zero in the plane of the first slice. The resulting stack is the target volume used during the actual registration procedure.

The reference volume is created from the a DRR calculated from the planning CT of a sufficiently large field in the direction of the current beam. This DRR is repeatedly copied and stacked until it has the same number of slices as the portal image stack (see Figure 2.2b). The DRR volume is then binned and also display equalized. Furthermore, the origin is defined as described for the target volume. The produced reference and target volume are used in the registration procedure as it will be described in section 2.2.4.

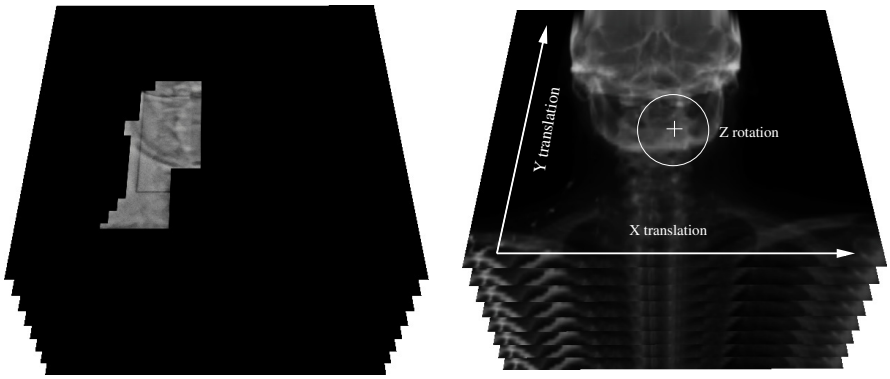

(a) Stacked segments to 3D volume.

(b) Stacked DRR with matching parameters: x- and y-translation and z-rotation around the isocenter.

Figure 2.2: Stack matching method.

2.2.3 Averaged projection matching method (APMM)

The averaged projection matching method is a simplification of the stack matching method. Instead of matching a segment volume with a DRR volume, the APMM reduces the registration to a 2D problem again. The cropped and preprocessed portal images are no longer stacked, but the portals are used to create a single 2D averaged image. In a way, the stacked volume is projected on the base plane, just as it is commonly done when creating a maximum intensity map (MIP) of a MRI or PET dataset, only this time the resulting image is a mean intensity map.

The artificial field is a 2D image and therefore duplicating and stacking the corresponding DRR is also no longer needed. Obviously, the calculation of the similarity maps take far less time (proportional to the number of segments in a beam) since APMM reduces the dimensionality of the problem. All other steps, such as the preprocessing of the portal images, are exactly the same as described in section 2.2.2.

2.2.4 Normalized mutual information similarity maps

The target and reference volumes (or images in case of the APMM) are registered using the normalized mutual information similarity measure (NMI) (Wells *et al.*, 1996; Maes *et al.*, 1997). Reason for using NMI is its theoretical robustness to intensity differences between the target and reference images and its overlap invariant behavior (Studholme *et al.*, 1999). DRRs and portal images are usually not in the same pixel value range and also the values of consecutive portal images can be slightly different, although in our case these differences are very small as described in section 2.2.1). Because of these (small) differences, similarity measures which use a fixed correlation between image values can not be used without prior intensity based calibration. By using NMI we avoid this extra calibration step. Furthermore NMI does not suffer from the edges which can emerge when combining segments that do not have the exact pixel range. Other edge-based registration algorithms, such as chamfer matching (Gilhuijs *et al.*, 1996), are

more likely to detect these boundaries as features rather than as artifacts. As the registration problem of both methods intrinsically is two-dimensional, we allow only three degrees of freedom: in plane x- and y-translation and z-rotation around the isocenter, which is by definition equal to the origin as described in section 2.2.2. Figure 2.2b summarizes the definitions of the match parameters.

In order to verify the usability and to compare our methods with other existing position verification routines, so-called similarity maps were calculated. Such maps present the relationship between the registration parameters, such as translations and rotations, and the used similarity measure, which is in our case the normalized mutual information measure. We varied the matching parameters as follows. The x- and y-translation had a range of -1.5 cm to 1.5 cm both divided into 51 steps. The z-rotation had a range of $-4.5°$ to $4.5°$ and was divided in 7 steps. The total map is a 3D volume (see Figure 2.3) with dimensions $51 \times 51 \times 7$ and the central voxel presents the similarity value when the match parameters are all zero.

The maps are able to depict two properties that are important when developing an automatic matching algorithm. First of all they show whether or not there is a global maximum in the map. If the parameters associated with this peak correspond with the ones found with a gold standard procedure, it is a method which is able to obtain enough matching information to find the correct maximum. Secondly, the similarity maps show the optimization "landscape" around the global peak. When the landscape consists of a lot of local maxima, standard optimization algorithms have a high probability of ending up at a peak that corresponds with a suboptimal set of registration parameters, and thus a misregistration.

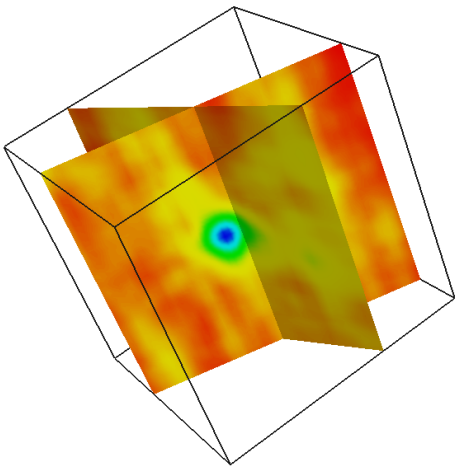

Figure 2.3: Three-dimensional normalized mutual information similarity map with two arbitrary orientated slices. In the middle the global peak is shown.

After the creation of the similarity maps, we refined the global peaks by 'zooming'. We calculated new similarity maps only this time the ranges of the x- and y-translation

and z-rotation were smaller, while the dimensions of the map remained the same. Furthermore, the centers of the new maps correspond to the point containing the global maximum which was found earlier in the initial similarity maps. By using this strategy the position of the optimum solution is more precise and does not suffer as much from discretisation problems. Finding or refining the global maximum could of course also be done by using an optimization algorithm, only choosing and tuning such an algorithm lies beyond the scope of this paper. However, as discussed before, we will investigate the automatic optimization potential of a landscape by generally important properties such the number of local maxima in the landscape.

2.2.5 Experiments

The response of the normalized mutual information measure, when using SMM and the APMM, is demonstrated by four experiments. In the first two, phantom studies are presented that use the head and neck area of an Alderson humanoid phantom. In the first phantom experiment, matching based on a single large field is compared with our methods which have a sequence of artificial segments formed by thin strips covering the same area as the large field as their input. The large field was 20×20 cm with a 6 MV beam of 5 MU in AP direction. The "strip" field consisted of 10 abutting segments with a dimension of 2×20 cm.

The second phantom study uses the AP beam of 17 segments of a clinical head-and-neck IMRT plan. The plan originated from the extended patient experiment described below. In this case the methods are compared with matching based on a large 20×20 cm field and with matching based on the largest segment of the IMRT plan.

In the third experiment, we applied both SMM and APMM on the IMRT segments of a clinical head-and-neck patient as a replacement of the standard 17×12 cm AP verification field. The match results of the registration based on only the largest segment are also presented. Furthermore, the effect of adding more and more small segments on the landscape of the mutual information map will be shown. We now sort the segments by irradiated area and start using them in increasing order. This way, the effect of adding more information to the registration will be demonstrated.

Finally, the SMM and APMM were tested on a group of nine clinical head-and-neck patients. The results were verified by means of visual inspection and again the effect of using more information on the position of the global maximum, is demonstrated.

All of the above experiments were delivered by using the "close-in, step and shoot" MLC technique used in our clinic, except the "strip" plan which was sequenced with a "sliding window, step and shoot" approach. In section 2.4 we will discuss in more detail changes in methodology that have to be applied when using other sequencing techniques, especially when a dynamic MLC is used. Furthermore, it must be stated that the EPID images of the large fields, the largest segments, and standard verification field have been cropped, binned and display equalized before they were used for registration, just as it has been done for all images used by our SMM and APMM.

2.3 Results

Figure 2.4c shows the image as it was used to obtain the results of matching of the large AP field on the corresponding DRR (Figure 2.4a) of the Alderson humanoid phantom. The mutual information map is shown in Figure 2.4d. From now on, we only show one slice of the mutual information map, which contains the maximum similarity measure of the complete volume. The slice presents all combination of the tested x- and y-translations given a fixed rotation angle, which is the angle that corresponds to the highest NMI response in the complete 3D similarity map. In other words, the slice shows the landscape with respect to the "optimal" rotation angle as it is found by the NMI measure. In Figure 2.4c and 2.4e the results of the APMM are presented. The effect of the cropping procedure is clearly visible: although the complete 20×20 cm field is irradiated, half of the total area is lost due to the masking of the penumbra effect, reducing the available matching information considerably. When comparing both mutual information maps, both global peaks are almost on the same location (x-translation difference: 0.01 mm, y-translation difference: 0.11 mm, and z-rotation difference: $0.11°$). As expected, the landscape of the APMM is not as good as the landscape constructed by the large field matching, since it is a bit less smooth, but is still well optimizable. The mutual information map of the SMM is exactly the same as the one of the APMM. This is caused by the fact that all segments of the "strip" plan are not overlapping, so the possible differences of using the complete segments instead of an averaged artificial one is zero in this case.

The results of the phantom study involving the 17 segment AP IMRT beam are presented in Figure 2.5. Figure 2.5a shows the largest segment of the beam, which is used for matching. In Figure 2.5b the artificial field resulting from the APMM is shown. Notice that the APMM field is almost twice as large as the largest segment and that although 5 mm of the field edge was cropped, still some small penumbra effects are visible at the border of the artificial field. This was caused by the field edge matching algorithm which returned a registration which was slightly off in combination with the fact that the particular region was covered by only one segment. Therefore the averaging step did not remove the last penumbra effects. Nevertheless, if one looks at the corresponding mutual information maps, the differences are negligible: all methods result in virtually the same global peaks (see Table 2.2), and the landscapes do not differ considerably in terms of smoothness and presence of local maxima.

Method	*X-translation (mm)*	*Y-translation (mm)*	*Z-rotation (degrees)*
Large 20×20 cm field	0.68	0.13	-0.92
Strip field	0.69	0.02	-1.03
Largest segment	0.50	0.18	-0.63
SMM	0.52	0.09	-0.75
APMM	0.51	0.07	-0.81

Table 2.2: Global peak locations of phantom IMRT experiment.

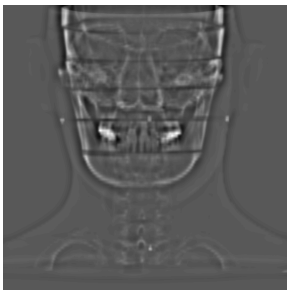

(a) Preprocessed DRR

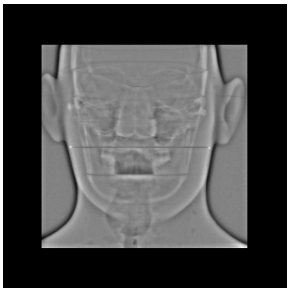

(b) 20 × 20 field

(c) Strip field

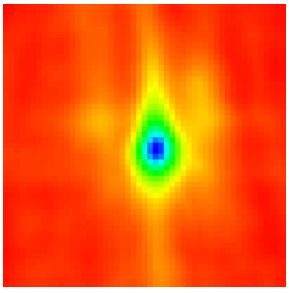

(d) 20 × 20 field: similarity map

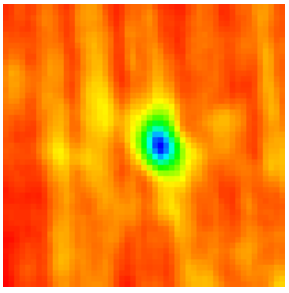

(e) Strip field: similarity map

Figure 2.4: Results of large field versus “strip” field experiment.

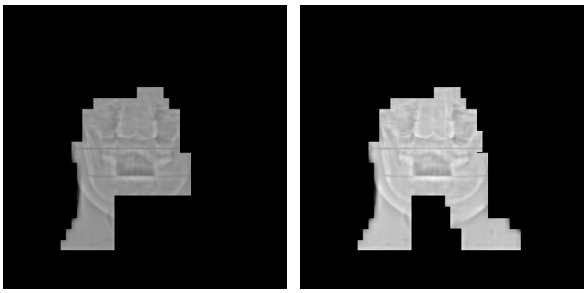

(a) Largest segment (b) Constructed by APMM

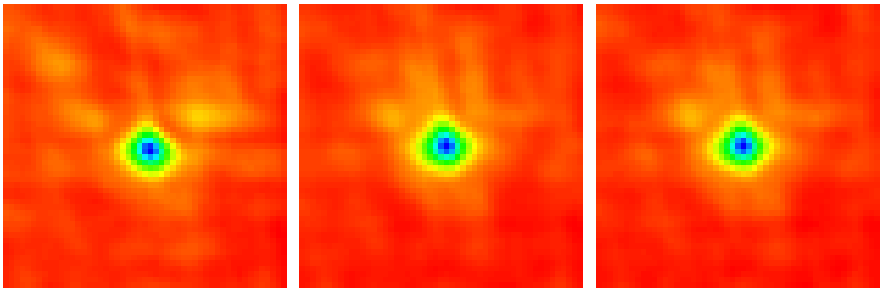

(c) Largest segment: similarity map (d) SMM: similarity map (e) APMM: similarity map

Figure 2.5: Results of phantom 17-segment IMRT beam of a head-and-neck plan.

The differences between the various matching routines became more clear when we conducted our third more extended patient experiment. This time, four different matches were computed, resulting in the similarity maps depicted in Figure 2.6. The first thing that became apparent, is the fact that the landscapes of the SMM and APMM are far better optimizable than the other two. Figure 2.6e shows a landscape with a lot of local maxima, making automatic matching very difficult, even though the used segment is relatively large. Also the landscape of the extra position verification field is not without difficulties: not only the large ridge moving northwards from the global maximum is worrying from an optimization point of view, but also the found optimal rotation is considerably different from the other methods (see Table 2.3). Apparently, the most significant bony structure (the jaws), is not restrictive enough in terms of automatic rotation optimization and more cranial bony structures are needed to find the correct rotation parameter, as they are available in all other methods. This misregistration was confirmed by visual inspection of the data, which means that our clinical position verification field in this case was inadequate for automatic matching purposes.

The differences between SMM and APMM are not very large, but if one looks closely to the results it can be observed that the APMM landscape has a slightly smoother landscape than the SMM. This is the result of averaging the portal images instead of using them directly. Structures which are stable (often bony anatomy) become more important, because they keep their original pixel intensity, where as the unstable structures

(a) Preprocessed DRR

(b) Largest segment (c) Position verification field (d) APMM

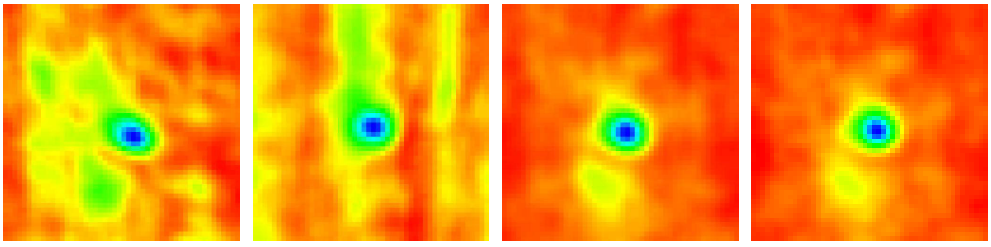

(e) Largest segment (f) Extra position verification field (g) SMM (h) APMM

Figure 2.6: Results of the clinical 17-segment AP IMRT beam of a head-and-neck patient.

become less important in the resulting artificial match image, because they get blurred. In other words, the signal-to-noise ratio (SNR) is higher for the APMM. Even though APMM is in this respect slightly better than SMM, both methods are influenced by intra-fraction movement, where as the other two methods are not since they just use a snap shot of the total fraction, which can lead to a false sense of accuracy.

Method	*X-translation (mm)*	*Y-translation (mm)*	*Z-rotation (degrees)*
Position verification field	0.89	0.63	-0.66
Largest segment	1.13	1.06	-2.73
SMM	1.03	1.18	-2.77
APMM	0.99	1.16	-2.68

Table 2.3: Global peak locations of patient IMRT experiment. The standard position verification field does not result in a correct registration, since it matches mostly on the jaws, which is not restrictive enough regarding the z-rotation.

The effect of adding more information to the matching process is demonstrated in Figure 2.7. It is interesting to see that even with very small number of segments covering only a small area, the global peak becomes visible. It also shows that the landscape improves drastically when larger areas are covered: the number of local maxima goes down and the global maximum becomes more clear. However, the figure depicting the landscape when using only the ten smallest segments also shows that adding more information does not necessarily directly lead to an improved optimization landscape. This means that in order to match automatically it is essential that the matching area should be as large as possible. In other words, SMM and APMM should always be used with as much portal image data as possible.

All eighteen matches obtained by the experiment which applied SMM and APMM on nine head-and-neck patients resulted in a correct registration of the artificially constructed dataset with the corresponding DRR. Visual inspection was done in order to verify the match results. Also, the effect of adding more information to the registration process became more obvious. Figure 2.8 shows the relation between the area of the artificially constructed averaged field and the deviation of the match parameters from the global solution of the APMM for each patient. In other words, all graphs are normalized by setting the match parameters of the APMM to zero, which is by definition the data point which uses all available image information for each patient. As excepted, when the area is very small, the correct match cannot be found, resulting in large, non-converging deviations of the match parameters. However, from 30 cm^2 on, most patients start to converge towards the good registration result. For seven patients the correct optimum can be found with only relatively small areas of up to 60 cm^2, whereas two patients needed more. This is caused by the differences of the type of information that is contained in these areas (stable versus non-stable structures). Nevertheless, when the area is larger than 90 cm^2, the chance of getting a misregistration is very small. Figure 2.9 shows the results of the SMM. Note that the x-axis is normalized to the one of the APMM graph, to make the comparison between the two methods more

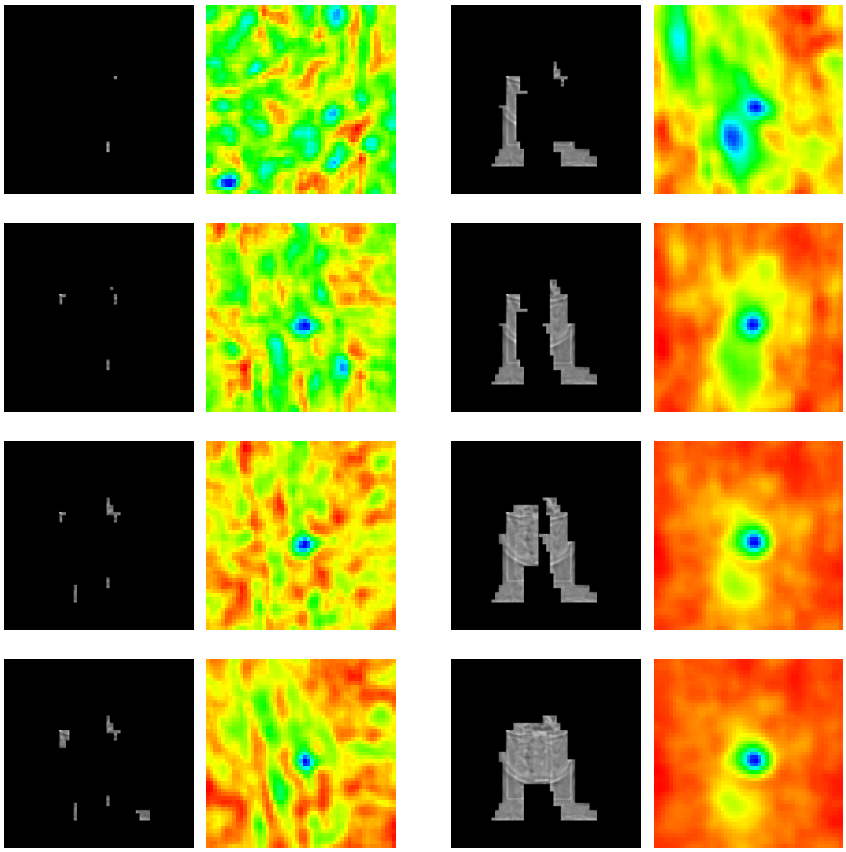

Figure 2.7: Results of adding segments to APMM. In the left column 2, 4, 6, and 8 segments are used to create the averaged artificial match image, and in the right column 10, 12, 14, and 16 respectively.

convenient. It is clear that both graphs are very similar, only in the first part (up to 40 cm^2) there are some differences, which can be explained by just a lack of matching information.

With respect to execution speed, SMM is clearly the slowest of the presented techniques, due to the simple fact that it uses the most data. Most time is spend on the calculation of the normalized mutual information measure. Also, because of the use of volumes instead of 2D images, the SMM uses more memory too. Both speed and memory usage of SMM increase when adding more segments to the procedure, while the other procedure only has increased memory and time consumption during the initialization phase. In Table 2.4 the results of nine head-and-neck registrations are summarized by showing the mean execution time and memory usage for calculating one normalized mutual information similarity measure. Calculations were executed on an Intel Pentium IV, 2.8 GHz machine. Since the similarity maps we used have $51 \times 51 \times 7 = 18207$

entries, it took on average 37 minutes to create APMM-map and just over 3 hours to create a SMM-map. When using a carefully selected and configured optimization algorithm instead of a complete NMI map for finding the global maximum, we estimate that a registration can be done by calculating the NMI roughly 100 times, yielding an registration execution time of approximately one minute and 15 seconds for SMM and APMM respectively.

Method	*Mean execution time (milliseconds)*	*Mean memory usage (MB)*
SMM	630	97.2
APMM	123	32.6

Table 2.4: Mean execution time and memory usage for calculating a single normalized mutual information measure when using the SMM or the APMM, based on data of nine clinical head-and-neck patients

2.4 Discussion

It may look like APMM is the preferred way to use for automatic patient position verification, because it has a small advantage over SMM with respect to the SNR, and the large advantage with respect to execution speed and memory usage. However, this is only the case if averaging of the portal images is allowed. In section 2.2.1 we showed that the pixel values of the raw portal images are stable and can therefore be averaged. If this is not the case and calibration of the images is not possible or insufficient, SMM is the preferred way of matching portals on a corresponding DRR. Instead of combining the absolute image pixel values directly, SMM just uses the pixel values to calculate the normalized mutual information measure. Since NMI is independent in relation to absolute pixel values, the portal images of the segments do not need to have interchangeable intensity values.

Since these methods are based on registering bony structures, the success of the routines still depend on the "availability" of these stable anatomies in the field. If clear bony structures are visible, our methods are capable of determining the correct registration parameters with only a limited amount of field area (between 40 and 60 cm^2). However, when these structures are not widely available within the part of the irradiated area, the methods do not deliver robust registrations any more. This produces the large deviations as depicted on the left side of Figures 2.8 and 2.9, since the chance of having a bony structure is limited when the total field size is small. In this case, more field area is needed to successfully find the optimal maximum.

If we look at other MLC delivery techniques, such as the "sliding window, step and shoot" technique and the dynamic MLC technique, we believe that both SMM and APMM can be even more useful. The field sizes during these delivery strategies are usually smaller, making matching based on the largest segment generally not feasible. No adaptations to the described methods are needed when using the "sliding window" technique to get the same benefits. When adapting the procedures for using them in

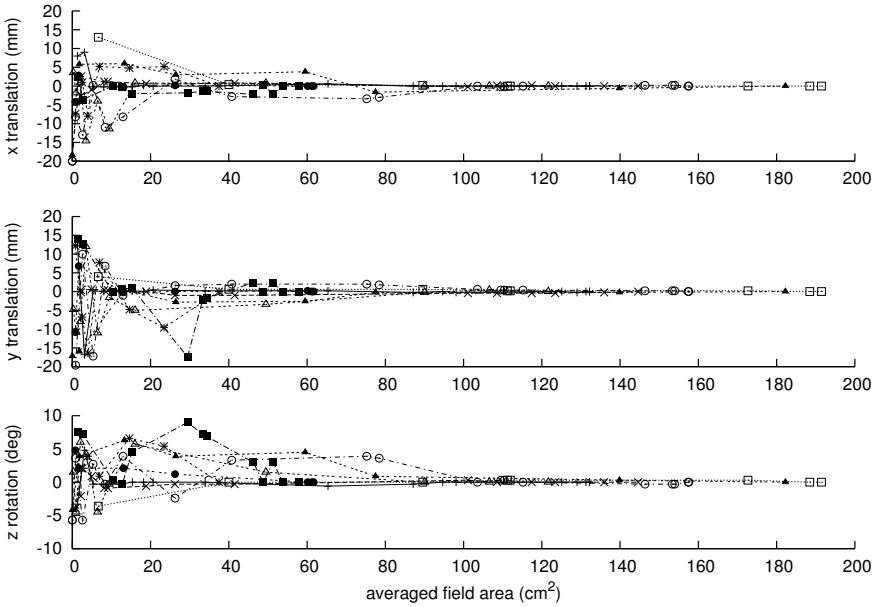

Figure 2.8: The behavior of the normalized match parameters of the APMM in respect to the artificially constructed averaged field area

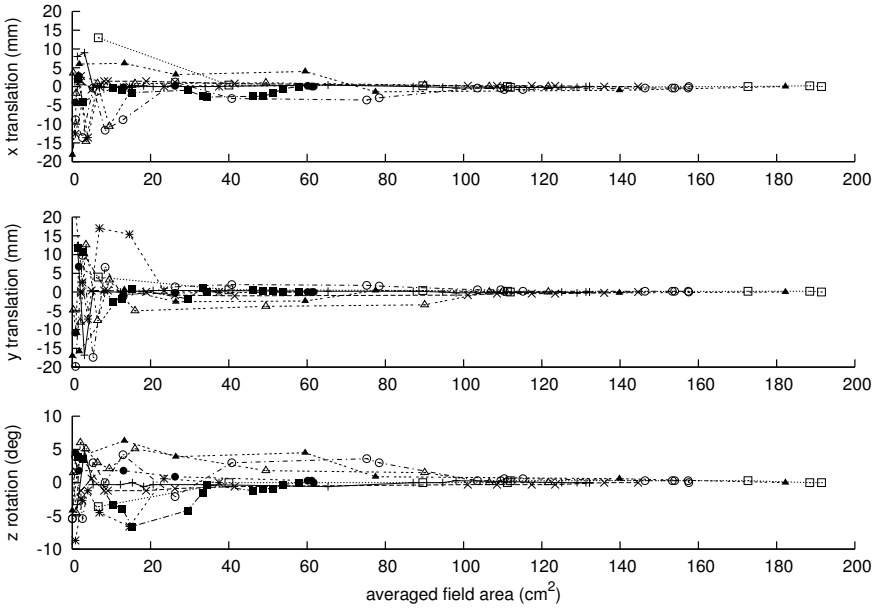

Figure 2.9: The behavior of the normalized match parameters of the SMM, plotted against the corresponding artificially constructed averaged field area of the APMM

combination with a dynamic MLC delivery, one should choose an appropriate time interval in which one portal image is constructed, since the leafs can move at different speeds during "beam on", as opposed to the "step and shoot" methods, where the leafs are at a fixed position when the actual irradiation of the patient takes place. If a large time interval is chosen, large areas of the image can have artifacts caused by travelling leafs, but if a smaller interval is chosen, the portal images themselves can get smaller. The optimal time interval is dependent on the way each plan is sequenced and it will even vary within one beam of the plan. However, even with a simple timing strategy (for instance a constant, short interval) SMM and APMM can be used as a substitute for large position verification fields in combination with dynamically delivered treatments.

2.5 Conclusions

In this paper we introduced two new methods which can be used for off-line patient position verification when only small IMRT fields are available. We showed that the matching results of the methods are comparable with the results obtained from existing methods. When we applied them to nine clinical patients, all matches were considered good by means of visual inspection, and there was no significant difference found between the two methods. This means that our methods can replace the method which uses the extra rectangular large field, reducing the total dose to the patient. Our data shows that when a distinct area of 40 to 60 cm^2 of the EPID is exposed during one treatment beam, the maximum NMI measure found corresponds to matching parameters of a good registration, as long as some bony structures are present in the overall irradiated area. However, adding even more information still improves the optimization landscape, which is important when one adds an optimizer to the matching routine. When the images of the EPID system are adequately normalized, APMM is preferred above SMM, due to a slightly better SNR, a faster execution time and lower computer memory consumption. When this is not the case APMM should not be used. We expect that the benefits of our method become even greater when using "sliding window, step and shoot" or dynamic MLC steering during delivery is used, since these techniques usually result in smaller segments.

3

Simultaneous multi-modality ROI delineation in clinical practice

This chapter is based on:
Bol G.H., Kotte A.N.T.J., Van der Heide U.A. and Lagendijk J.J.W. 2009 Simultaneous multi-modality ROI delineation in clinical practice *Computer methods and programs in Biomedicine* **96** 133–140

Abstract

The delineation of tumors and their surrounding organs at risk is a critical step of the treatment planning for radiation therapy. Besides computer tomography (CT), other imaging modalities are used to improve the quality of the delineations, such as magnetic resonance imaging (MRI) and positron emission tomography (PET). A practical framework is presented for using multiple datasets from different modalities during the delineation phase. The system is based on two basic principles. First, all image datasets of all available modalities are displayed in their original form (in their own coordinate system, with their own spatial resolution and voxel aspect ratio), and second, delineations can take place on all orthogonal views of each dataset and changes made to a delineation are visualized in all image sets, giving direct feedback to the delineator. The major difference between the described approach and other existing delineation tools is that instead of resampling the image sets, the delineations are transformed from one dataset to another. The transformation used for transferring the delineations is obtained by rigid normalized mutual information registration. The crucial components and the benefits of the application are presented and discussed.

3.1 Introduction

Accurate delineation of tumors and surrounding organs at risk is a critical step in treatment planning for modern radiotherapy. Besides the so called planning CT, which forms the basis for radiotherapy dose calculations and treatment optimization, other imaging modalities are added to improve the quality of the delineations. Due to the superior soft tissue contrast over CT, magnetic resonance imaging (MRI) is one of the most prominent modalities used to enhance the visibility of tumor tissue and surrounding organs at risk (Van de Bunt *et al.*, 2006; Daftari *et al.*, 2005; Villeirs *et al.*, 2005). This technique

can be exploited by using multiple scanning sequences in different directions in one imaging session, each depicting specific information on which delineation decisions can be based. Also positron emission tomography (PET) is often used for delineation purposes, especially for identifying positive lymph nodes (Moureau-Zabotto *et al.*, 2005; Grosu *et al.*, 2005; Esthappan *et al.*, 2004).

Since these different imaging datasets are becoming more and more available in the clinic, a new infrastructure is needed that provides an efficient and convenient way to work with these sets. In other words, a transition has to be made from a single dataset, CT-based delineation strategy to a multi-modality, multi-dataset based delineation regime.

We have developed an application which provides a practical framework for using multiple datasets from different modalities during the delineation phase of the treatment planning. We formulated two major objectives:

- Each dataset is displayed in its own coordinate system and with its own spatial resolution. By displaying the sets separately and keeping the image content intact by using its own aspect ratio, delineations are performed on the patient data as it was originally acquired and intended. This property is especially useful when using angulated MRIs or MRIs which are imaged with an high in-plane resolution but a relatively large slice thickness due to scanning time constraints.
- The delineation of structures can be performed in all available datasets and on every orthogonal plane of each dataset. By using different modalities simultaneously and therefore giving direct feedback to the physician, the delineation consistency can improve. We transform the delineations between the different coordinate systems using a transformation which is obtained by image registration.

Furthermore, all contours which are manually delineated by a physician are never changed or adapted by anyone or anything other than the delineator himself. This also means that techniques such as contour smoothing, are only applied on explicit user request. The physician stays in control of the delineation process at all times. This objective increased the acceptance of our tool within our department considerably.

Here, we describe the crucial components of our delineation system, such as the registration phase and the simultaneous construction, transformation and visualization of the delineations on the different modalities. We also show how the framework is used within our department.

3.2 Materials and Methods

3.2.1 Data definitions

Before we describe our tool in detail, we first define the terms we use regarding the data types needed to explain the principles our ROI delineation strategy.

Original image data These are usually three dimensional image datasets as acquired on a imaging modality such as CT, MRI, PET etc. The datasets have the same resolution and slice orientation as it was captured on the imaging device.

Resampled image data Image data derived from original image data, usually placed in a different coordinate system having a different resolution and slice orientation than the original image data.

Delineation data Delineation data is captured in contours (polygons) and triangulated 3D meshes. Note that in this paper delineations are never stored or converted to a voxel models and exist in 3D space without the of use of an underlying (original or resampled) image dataset.

Transformation data Describes how one coordinate system is associated with another coordinate system. Since we only use rigid transformations (translation and rotation), a transformation is described in a 4 by 4 transformation matrix when using homogeneous coordinates.

3.2.2 Clinical setup and work flow

In Figure 3.1 the integration of the delineation tool within our department is visualized. It starts with acquiring various medical images from the patient at hand: besides the standard planning CT, usually several MRI datasets are imaged during an imaging session and stored in a local database (Table 3.1 shows the number of imaging sessions for each modality in 2007 and 2008). After acquisition, the registration step takes place. The MRIs are registered to the planning CT by using an intensity based matching algorithm (see section 3.2.3). To ensure the quality of the registration, all registrations are visually inspected. Next, the delineation of the tumor and other regions of interest can start based on all available image modalities. Because of the lightweight character of the contouring application combined with a client-server setup (all CPU intensive tasks are performed on the server), this is done on a standard desktop PC of the physician.

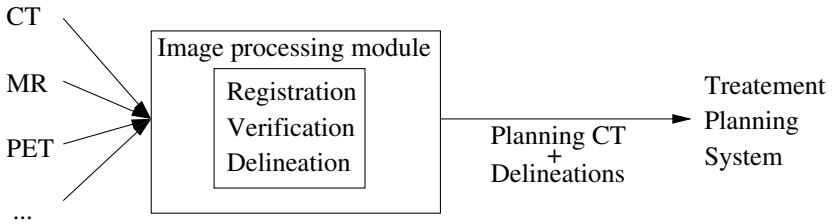

Figure 3.1: The delineation framework as it is currently implemented. The arrows represent a DICOM link. Is starts with acquiring the medical images, then the registration and delineation takes place, followed by the export of the planning CT along with the delineations to the planning system.

After contouring, all delineations are converted to the coordinate system of the planning CT and transferred to the treatment planning system. All in- and outgoing connections of our framework are solely based on DICOM and also all locally stored data

is kept in the DICOM file format. We have implemented the specialized radiotherapy subset of DICOM standard (DICOM RT) for transporting and storing the delineation data based on the official standard as described by the National Electrical Manufactures Association (NEMA). But we also used the DICOM conformance statement of our planning system for resolving some minor vendor specific issues. By using the DICOM standard, we are not dependent on vendor specific communication protocols, since DICOM is supported by all major commercially available imaging- and planning systems. Furthermore, this open framework enables us to access all imaging and delineation data easily for research purposes, especially when performing delineation and advanced imaging studies.

Modality	*2007*	*2008*
CT	2635	3129
MRI	868	1208
PET	56	193
Other	9	4

Table 3.1: Number of imaging sessions for each modality in 2007 and 2008 solely used for delineation purposes.

3.2.3 Registration

Before delineation can take place, the available datasets have to be registered to correctly correlate the different coordinate systems. In order to reduce the number of registrations needed, we define a so-called "master" dataset, which defines the global reference coordinate system of our application. We normally use the standard planning CT as the master, since this one is used during the treatment planning phase. Next, all other datasets are registered to the master set. Since all registrations share a single coordinate system (the master coordinate system), the other datasets are also indirectly registered between each other.

The registration itself is performed by the Vtkview toolkit (VTK CISG Registration Toolkit; King's College London, London, UK). It uses the normalized mutual information (NMI) (Pluim *et al.*, 2003) similarity measure as its optimization parameter and produces rigid transformations. This means that only translations and rotations are allowed. We use only rigid transformations because the quality assurance (QA) of such a registration is more insightful and observer independent than the QA of a non-rigid registration (Hajnal *et al.*, 2001). NMI is a well-established registration similarity measure, which makes it possible to successfully register multi- as well as mono-modality datasets (Studholme *et al.*, 1999; Maes *et al.*, 1997). This means that the technique can be used for CT-MR, CT-PET and MR-MR registration.

Although most steps of the registration procedure runs without human supervision or intervention, all resulting registrations are checked by means of visual inspection. In order to register various tumor sites and types, we implemented three registration strategies:

Full registration Uses the given image datasets as is.

Segmented registration Before the actual registration is performed a coarse segmentation step is added, which makes it for instance possible to register solely based on the bony anatomy.

Partial registration Uses only small parts of the given datasets, this enables registering on specific regions of interest. Usually a box shaped region is defined.

In order to make registration results even more reliable we try to make all image datasets in exactly the same patient (treatment) position using radiotherapy specific positioning procedures, such as head masks, arm rests etc. This reduces the amount of human interaction considerably, since in most cases the registration will find an acceptable transformation without any user-defined registration initialization. When the patient is not imaged in the same position, finding a good registration becomes more complicated to achieve or is sometimes even impossible.

3.2.4 Delineation construction and visualization

The key difference between this system and other delineation tools is that the delineation is transformed between the datasets instead of transforming the image content beforehand by means of resampling. From the registration we have obtained the transformations between the various sets, so we now know how a point in one coordinate system can be transformed to any of the other image datasets. However, direct transformation of the contours is usually not possible, because they are originally constructed within the planes of one of the registered datasets, and these planes do typically not coincide with planes in another dataset.

Therefore, we construct a three-dimensional closed mesh of triangles from the stack of contours using a parallel slice reconstruction algorithm (Boissonnat, 1988). The algorithm matches similar portions of each pair of adjacent slices, and it tiles the matched contour portions by a sequence of adjacent triangles. The matching and tiling are based solely on the similarity between the xy projections of the two contours. No contours in other slices are affected. This resulting 3D mesh can be transferred to other datasets by transforming each vertex according to the transformation matrices obtained from the registration routine, as is schematically shown in Figure 3.2. The use of registration matrices is possible since we only use rigid transformations. By reslicing the mesh with planes of the other dataset at hand, the delineation is visualized.

The delineation itself is contour based. After the physician contoured the structure on one of the orthogonal views of the image volume, a new 3D mesh can be reconstructed and this mesh is displayed in all other datasets. By using a linked cursor, which shows a common point in all datasets, the physician can verify the delineation on all other datasets and adjust it if necessary.

When a contour is added or edited, a new mesh can be generated and is visualized in all the other datasets. This way, the users can see the impact of their actions on more

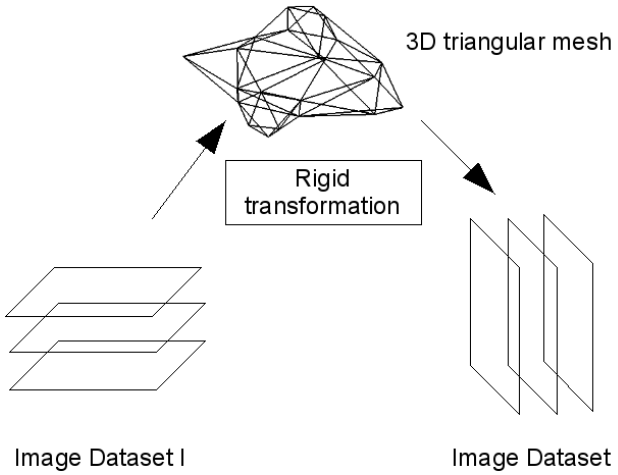

Figure 3.2: The transfer of a delineation from one image dataset to another, using the rigid transformation obtained from the registration procedure. First the mesh is constructed for the contours delineated in dataset I, after transforming the mesh, it is resliced and displayed on the planes of dataset II.

than one dataset simultaneously and use this information during delineation. Updating a typical delineation (in other words, regenerating the 3D mesh from a stack of contours and reslicing it for visualization) takes only a fraction of a second, whereas large structures (such as the body contour and the lungs) takes less than two seconds. It is also possible to really reslice a delineation onto another dataset and continue contouring on this other dataset until a satisfiable result has been reached. As mentioned before, the resulting VOI is then resliced on the planning CT. The polygons produced in this last step are send (accompanied by the CT) to the planning system.

3.2.5 Hardware and software

We developed the tool in a operating system independent way by using the Java 2 programming language and its virtual machine, it runs on both Microsoft Windows based systems as well as on GNU Linux systems within our department. The hardware requirements depend mostly on the size of the original image datasets, but in general we use 2.8 GHz Intel based systems with 500 MB of RAM. The framework supports standard DICOM protocols and has an open architecture, which makes it also a valuable research tool.

3.3 Results

In this section we describe three typical examples which show how the system is used within our department on a daily basis. Before the framework was introduced in the clinic, extensive testing was performed based on the European SocieTy for Radiotherapy and Oncology (ESTRO) guidelines regarding delineation tools for radiotherapy (Mijnheer *et al.*, 2004). The first example depicts the delineation of a prostate cancer pa-

tient which received an intensity modulated radiotherapy treatment (IMRT). The second example shows the delineation of a head-and-neck tumor, whereas in the last example a cervical cancer patient is presented.

In Figure 3.3 two screenshots of the application are shown. The delineation of the clinical target volume (CTV) of a prostate patient was performed on a balanced fast field echo (BFFE) MRI. Both the prostate itself (especially the apex and the lateral sides) and the bladder-prostate boundary can be easily determined on the MRI, rather than on CT. Furthermore, the resolution of the MRI scan is much better ($0.5 \times 0.5 \times 1.0$ mm versus $0.9 \times 0.9 \times 3.0$ mm). In order to register these datasets, the partial registration method is used with only a small box surrounding the prostate. This way, undesired effects on the registration result caused by the movement of the prostate are minimized. The registration accuracy was measured using four anatomic landmarks detected manually from both images. The average distance between the landmarks after registration was 1.4 mm, whereas the average accuracy outside the registered box is determined at 5.4 mm, showing the effect of the partial registration. The 3D mesh is reconstructed from the stack of contours defined in the transversal slices of the CT. This means that the contours of the coronal and sagittal view of the CT and all views of the MRI are calculated by slicing the reconstructed 3D mesh (which is also transformed by the registration transformation in the case of the MRI) by the corresponding viewing planes.

In order to delineate head-and-neck tumors correctly (these include cancers of the sinus, the oral and nasal cavity and the larynx), we use at our department three different modalities: a planning CT, a series of differently acquired MRI sequences, and a FDG PET. Typically, the image resolutions differ a lot: $0.9 \times 0.9 \times 3.0$ mm, $0.4 \times 0.4 \times 4.4$ mm, and $4.0 \times 4.0 \times 4.0$ mm for CT, MRI and PET respectively. Figure 3.4 shows three transversal slices of the datasets. By adding MRI and PET information, outlining of the gross target volume (GTV) and the pathological lymph nodes is more obvious than when using solely CT information. Since everything was imaged with the patient in the treatment mask and all sets cover the same part of the body, the complete datasets are used during the registration phase. This resulted in a CT-MR registration accuracy of on average 1.2 mm by using four different landmarks. The accuracy of the CT-PET is difficult to assess due to PET thresholding artifacts, but was estimated at 3.1 mm.

In Figure 3.5 three orthogonal T2 weighted MRI datasets of cervical cancer patient are shown. All MRIs have an in-plane pixel spacing of 0.6×0.6 mm and a slice thickness of 4.5 mm. Furthermore, the planning CT has a pixel spacing of $0.8 \times 0.8 \times 3.0$ mm. The white contours mark the delineated CTV of the primary tumor in all images. The border between CTV and surrounding tissue can be determined better on the MRI images than solely on the planning CT. In clinical practice the sagittal MRI is mostly used for indicating the caudal and cranial border of the CTV, whereas the coronal view is used for correctly determining the lateral extension of the parametrial tissue. In this case registration of the CT and the MRIs was based on the bony structures of the patient (segmented registration), since the soft tissue itself suffers too much from internal organ motion. The accuracy of the bone match is on average 2.0 mm. Large deviations can be observed when choosing landmarks within the target area (up to 17 mm, due to rectal filling).

(a) Screenshot of the window with the planning CT

(b) Screenshot of the window with corresponding BFFE MRI

Figure 3.3: Two screenshots depicting the datasets which are currently used while delineating the prostate and the surrounding tissues: one with the planning CT and the other with the corresponding BFFE MRI. The cross is the linked cursor, depicting the same location in all datasets.

(a) Planning CT, transversal (b) MRI T1 weighted, transversal (c) FDG PET, transversal

Figure 3.4: Three different modalities (CT, MRI, and PET), used during the delineation phase of the IMRT treatment planning of head-and-neck tumors. The white cross is the linked cursor, depicting the same location in all datasets.

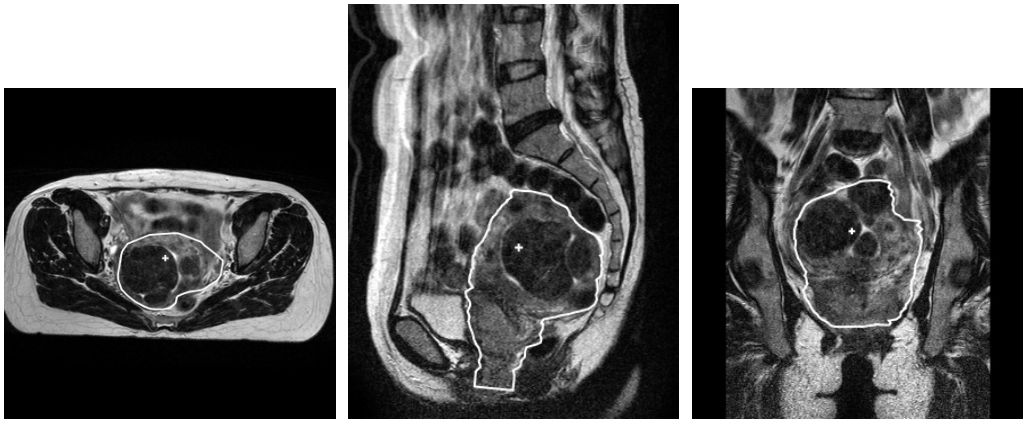

(a) MRI T2 weighted, transversal (b) MRI T2 weighted, sagittal (c) MRI T2 weighted, coronal

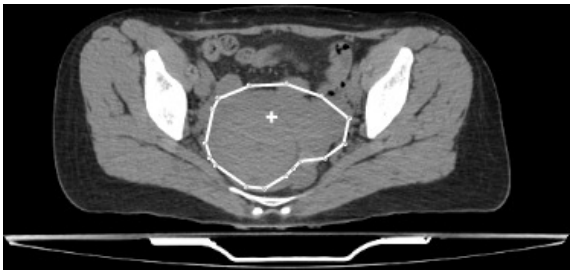

(d) Planning CT, transversal

Figure 3.5: Three orthogonal MRI datasets along with the corresponding planning CT of a cervical cancer patient. The white cross is the linked cursor, depicting the same location in all datasets.

Figure 3.6 shows the resampled version of the original MRI datasets of the cervical cancer patient. The sets were resampled with trilinear interpolation to the same resolution as the planning CT. This technique is commonly used in other multi-modality delineation tools. Since the caudal-cranial pixel spacing of the CT is relatively big, the resulting sagittal and coronal MRI images loose a lot of their image quality which makes it harder for the delineator to make a clear distinction between targets and surrounding healthy tissue.

On the other hand, the MRIs are upsampled in the slice direction, leading to extensive memory usage. Instead of having just the four original datasets loaded into computer memory, with the resample technique the memory usage is usually four times the memory consumption of the CT. In this case the total memory usage when using our approach is $63 + 16 + 15 + 16 = 110$ MB, whereas the resampling method needs $4 \times 63 = 252$ MB, making our method more appropriate for usage on a standard desktop PC. Obviously, this advantage increases when the dataset that is used as 'master' gets even larger, for instance when a multislice CT is used.

Also in the case of the prostate patient example the effect of direct resampling is large: if the MRI is downsampled to CT resolution, each voxel of the resampled MRI averages the information of 9.72 original MRI voxels, reducing the visualization of structures considerably. When applying the same routine on the PET image of Example 2, the information of each original PET voxel is spread on 26.34 voxels in the interpolated PET image, creating a false perception of high resolution.

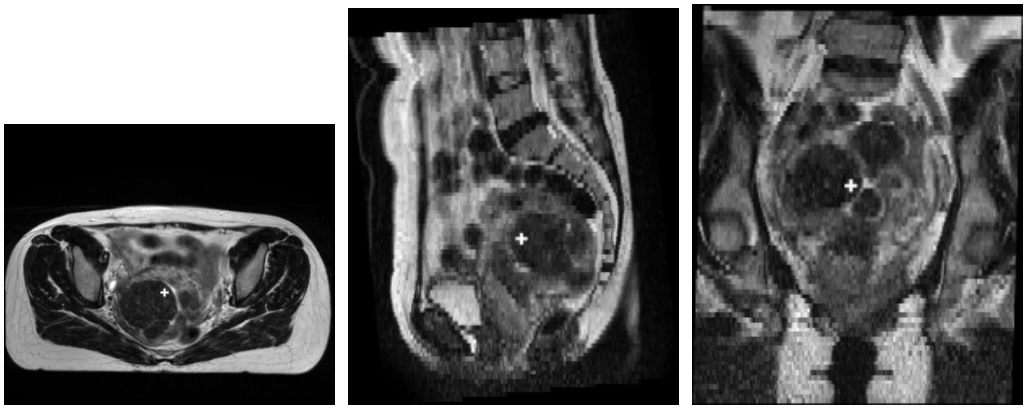

(a) Resampled MRI T2 weighted, transversal (b) Resampled MRI T2 weighted, sagittal (c) Resampled MRI T2 weighted, coronal

Figure 3.6: The same MRI datasets as shown in Figure 3.5, only this time resampled to the planning CT by using trilinear interpolation. Note the degeneration of the sagittal and coronal MRI images.

3.4 Discussion and conclusions

In the previous section we showed some examples of cases where the physician is given the opportunity of delineating targets and organs at risk in such a way that only the

originally acquired image datasets of the patient are used. We imposed this requirement on the system, so that the delineator has a better indication of the spatial resolution of the different scans. By using more modalities, the contours of the tumor can be determined more accurately (Examples 1 and 3) and the chance of missing parts of the targeted tissue becomes smaller (Example 2).

Other delineation systems used within a radiotherapy setting (such as Pinnacle TPS (Philips, Eindhoven, the Netherlands) and Oncentra Masterplan (Nucletron, Veenendaal, the Netherlands)) choose to resample the datasets after registration. This can make it hard for the physician to recognize partial volume effects since most of the displayed pixel values are interpolated and can therefore give a false sense of accuracy, especially when the originating datasets have very different resolutions (see Example 2). By using a different strategy to link the various image datasets (thus by transforming the delineations), we avoid these resample problems.

Although we do not resample the imaging datasets, the delineation method is still a contour based one. This means that when a delineation originally is contoured on one set by using the guidance of the linked cursor and is completely converted to the planning CT, partial volume effects still take place: the 3D mesh is 'sliced' on the CT, which usually has a poor caudal-cranial resolution. Therefore we advise our physicians not to convert the delineations from one dataset to another dataset profusely. Also when neighboring contours are very different, the 3D reconstruction can cause artifacts, because the problem of automatically connecting two very different contours is not well defined and has many possible solutions. However, in clinical practice the contours of a tumor changes gradually, since the resolution of the underlying MRI is determined by the expected irregularity of the tumor type.

Another possibility is to use semi-automatic segmentation. The basic idea is to fit automatically a 3D triangulated deformable model to the image datasets of the patient, followed by a correction phase in which the physician can adapt the delineation manually (Lötjönen *et al.*, 2008; Lötjönen, 2003). This type of delineation is especially useful when the desired structure is well known in advance. However, due to the unpredictable shape of tumors, this approach is less suitable within the radiotherapy field.

The real solution to the delineation discretization problem is to use a truly 3D based delineation method instead of a contour-based one: it should allow manipulation of the 3D mesh directly on all datasets at the same time rather than using the 3D mesh as a convenient datastructure for transporting delineations from one dataset to another. This solves the discretization problems during delineation, however the mesh still has to be sliced to the planning CT before it can be handled by the planning system. Such a strategy could be developed using the reconstruction algorithm of Amenta *et al.* (2001), which produces a 3D mesh from a cloud of user-defined points instead of contours, by-passing the contour difficulties as described in section 3.2.4.

Another difference with traditional resampling methods is that for instance the transversal displayed slice of one dataset does not necessarily correspond with a displayed transversal slice of another dataset. This is caused by the fact that the patient can be

shifted or rotated between image sessions or by acquiring an angulated dataset. Only the position depicted by the linked cursor in both datasets has a one on one correspondence. However, the individual image set does not suffer from resampling artifacts (as shown in Figure 3.5 and 3.6) and by moving the linked cursor each delineation can be verified adequately.

Although the primary topic of this study is not image registration, it is important to state that registration is a crucial step within our framework, just as it is for the resampling delineation method. The quality of the registration has a direct influence on the quality of the delineation which is eventually used for treatment planning. This is why we introduced specific registration methods for certain patient groups, resulting in an acceptable registration performance. Currently we are looking into the possibility to do first a rigid transformation based on bones, followed by a non-rigid registration in the area where the tumor is situated. Still the quality assurance of such a procedure remains difficult and adds extra complexity to the tool.

The delineation quality obtained from our system, should be similar or better than the delineations created with other tools. We try to avoid partial volume artifacts as much as possible, which benefits the overall delineation procedure. However, to really assess the benefits a large comparative delineation study should be performed, but that is beyond the scope of this paper.

Since the introduction of our system at our department the awareness regarding differences between spatial resolution of especially CT and MRI scans, has let to more consistent imaging protocols and delineation strategies. In the future, we will add truly 3D delineation methods to our system and more advanced options (such as automated registration assessment (Ceylan *et al.*, 2005)) to the registration phase which will reduce the number of necessary human interactions even more.

Here, we showed a framework in which the physician is able to simultaneously delineate targets and organs at risk on multi-modality image sets, without the need of preproccessing the images, using the full potential of each available dataset, while it does not need excessive hardware requirements. The software is standardly used throughout our department and is able to export clinically approved delineations to the beam optimization module of the planning system.

4

MRI-compatible fiducial gold markers for prostate cancer patients

This chapter is based on:
Bol G.H., Van der Heide U.A., Kotte A.N.T.J., van Vulpen M. and Lagendijk J.J.W. 2008 MRI-compatible fiducial gold markers for prostate cancer patients in *Radiotherapy and Oncology proc. ESTRO 27, Göteborg, Sweden* vol. 88, suppl 2, nr 1171 p. S374

Abstract

MRI based target delineation is rapidly gaining ground. Fiducial gold markers are poorly detectable on most MRI sequences. Therefore, markers always have to be detected on a separated CT, adding extra CT ↔ MRI registration errors to the treatment preparation phase. We developed a marker which is visible on MRI and on EPID. A separate CT is no longer needed. The marker consists of a steel core with a diameter of 0.3 mm within a gold casing. The marker is 5.0 mm long and has a diameter of 1.0 mm. The steel core provides visibility on MRI and the gold casing on EPID. To investigate the interobserver variability, five experienced observers marked the positions of the markers on three MRI sequences: a bSSFP, T1- and T2-weighted sequence. These positions were also compared to the CT based marker positions. The bSSFP is best suited for delineating the prostate and detecting the developed markers. The interobserver variability is small (the mean absolute distances ranges from 0.16 mm to 0.30 mm). The differences between the MRI based detection and the CT base detection are also small, considering it contains registration errors: the mean absolute differences ranges from 0.43 mm to 1.44 mm. The gold marker with steel core can be detected on various MRI sequences, reducing the overall systematic treatment error.

4.1 Introduction

Fiducial marker based position verification has significantly improved the accuracy of the external beam radiation therapy for prostate cancer (Van der Heide *et al.*, 2007; Nederveen *et al.*, 2002; McNair *et al.*, 2008). Because the prostate cannot be visualized directly during treatment with megavoltage imaging, typically solid gold markers are implanted (Dehnad *et al.*, 2003; Van der Wielen *et al.*, 2008; Schiffner *et al.*, 2007). The markers indirectly visualize the prostate position, since they have a sufficiently high

density in order to detect them on an electronic portal imaging device (EPID). Prostate deformation cannot be detected, but the impact of this on the total dose given to critial organs such as the rectum is negligible (Kerkhof *et al.*, 2008). The markers are implanted before the acquisition of the planning CT scan. From this scan the marker positions are automatically extracted and when target contouring takes place on the same CT, a direct correlation between markers positions and the planning target volume (and thus the treatment fields) is established. This correlation is used when the daily position of the prostate is verified by detecting the gold markers with the EPID.

Although CT is still used for delineating the targeted prostate volume, MRI based contouring is rapidly gaining ground due to superiour soft tissue contrast and therefore smaller intraobserver variability (De Meerleer *et al.*, 2005; Khoo *et al.*, 2006; Smith *et al.*, 2007; Parker *et al.*, 2003). However, the gold markers are poorly detectable on most MRI sequences (see Figure 4.2b, 4.2d and 4.2f). In order to obtain the required correlation between the markers and the delineated structures, the MRI is registered to the planning CT using for instance mutual information matching (Maes *et al.*, 1997) or by detecting the implanted fiducial markers on a separated dedicated MRI sequence within the same imaging session (Huisman *et al.*, 2005). However, due to registration errors and intra imaging session motion respectively, the correlation between the markers and the contours can be disturbed, introducing a systematic error into the radiation therapy treatment.

In this study we introduce a new kind of fiducial marker which is visible on most MRI sequences and on EPID. The goal is to delineate the prostate and accurately detect the positions of the gold markers in the same MRI sequence. This procedure does no longer need a MRI-planning CT registration in order to correlate the marker positions and the delineated structures. This is important because these types of registration faults can not be compensated during treatment, and therefore introduce a systematic error: during treatment planning only the on MRI delineated structures are taken into account, but when the treatment is delivered, only the positions of the markers are checked. If the delineated structures and the markers are misaligned relative to each other due to registration errors, no correction protocol will correct for these mistakes.

An additional advantage is that the influence of intra imaging session motion is minimized when using just one MRI sequence for delineation and marker detection. In this study, we describe the design of the marker, we test the reproducibility of the manual detection of the markers, and we compare the positions of markers found solely based on the MRI with the positions found with the current combined CT-MRI based marker extraction procedure.

4.2 Methods and Materials

4.2.1 Fiducial markers

The new fiducial markers consist of a pure gold cylinder with a central core of surgical steel (Ethicon Stahldraht®). While the gold cylinder provides visibility on the EPID, the steel core provides the artifact on MRI. The core causes signal loss due to dephas-

ing of the spins. The shape of the resulting artifact can be predicted as described by Lagerburg *et al.* (2008). The marker has a diameter of $1.0\ \mathrm{mm}$ and is $5.0\ \mathrm{mm}$ long and has rounded tips to avoid unnecessary tissue damage. The steel core has a diameter of $0.3\ \mathrm{mm}$.

The manufacturing process starts by inserting a surgical steel thread into a hollow cylinder of gold. In this phase, the outer and inner circumference of the cylinder is slightly larger than its final dimensions. After this, the cylinder is stretched until the steel thread is tightly confined within its gold casing. Finally, the markers are cut at the appropriate length and then lathed to obtain the rounded tips.

Figure 4.1a shows a photograph of the marker and Figure 4.1b shows a electron microscopic (EM) image of a marker tip. In the center of the marker tip, the steel core is clearly visible. The lighter material is the gold casing surrounding the steel core. The markers are biocompatible due to the choice of materials and are easily manufactured in large quantities. Since the edge at the rounded tip between the steel core and the gold casing is very smooth, the marker can be properly sterilized.

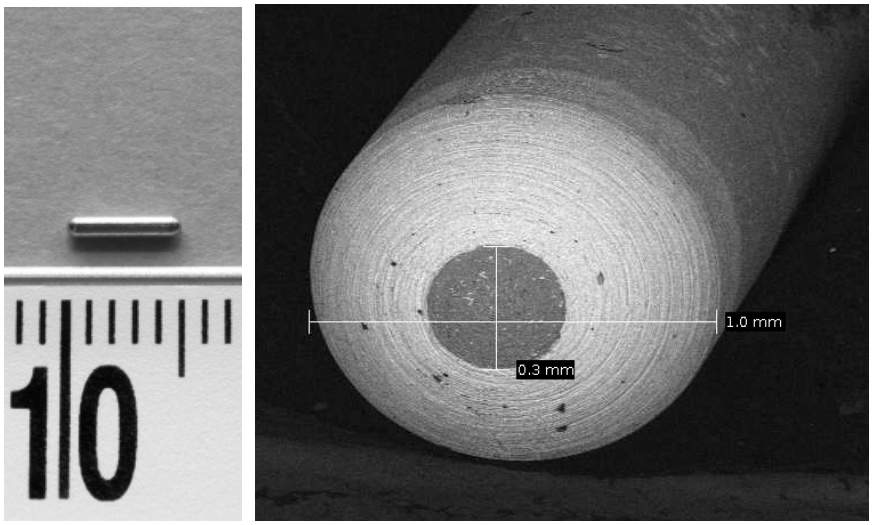

(a) Gold marker with steel core

(b) Electron microscopic image of the marker tip

Figure 4.1: Gold markers with steel core for patients treated for prostate cancer.

4.2.2 MRI sequences

All MRI exams were carried out at a 3T MRI scanner (Achieva, Philips Medical Systems, Best, NL). The planning CTs were acquired on a single slice CT scanner (Aura, Philips Medical Systems, Best, NL) and have an in-plane slice resolution of $0.49\mathrm{x}0.49\ \mathrm{mm}^2$ and the slice thickness is $3\ \mathrm{mm}$. For prostate imaging and treatment planning, three MRI sequences were used:

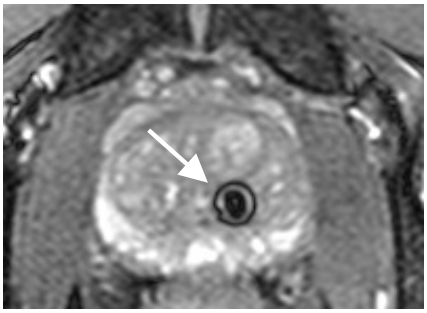

(a) bSSFP, transversal, with steel core

(b) bSSFP, transversal, pure gold

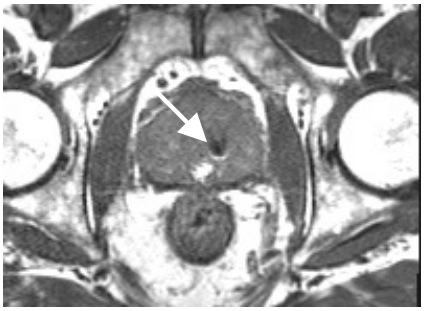

(c) T1, transversal, with steel core

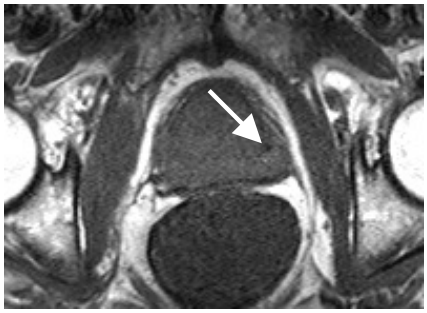

(d) T1, transversal, pure gold

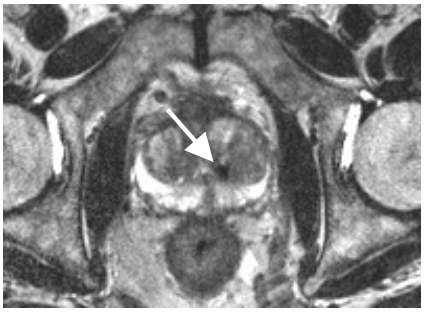

(e) T2, transversal, with steel core

(f) T2, transversal, pure gold

Figure 4.2: Visibility of the new gold markers with a steel core (Figure (a), (c) and (e)) compared to the pure gold markers (Figure (b), (d) and (f)).

1. A 3D balanced Steady State Free Precession sequence (bSSFP) (TR/TE = 5.3/2.4 ms) using 90 slices with a $0.5\text{x}0.5\text{x}1\ \text{mm}^3$ reconstructed resolution and a flip angle of 21 degrees.

2. A multi-slice T1 weighted spin echo (SE) sequence (TR/TE = 570/30 ms) using 25 slices of $4\ \text{mm}$ and a reconstructed resolution of $0.8\ \text{mm}$.

3. A multi-slice T2 weighted Turbo Spin Echo (TSE) (TR/TE = 8400/120 ms, turbo factor=13) with identical resolution and spatial coverage as the T1 weighted sequence.

The MRI sequences were carried out in a single imaging session and between the scans the patient was not moved. The bSSFP had an acquisition time of $2\ \text{min}\ 9\ \text{s}$, the T1 took $6\ \text{min}\ 12\ \text{s}$ and the T2 $8\ \text{min}\ 23\ \text{s}$. Time constraints were the cause of the rather large T1 and T2 slice thickness.

The bSSFP is specifically designed for delineating the prostate and the seminal vesicles. The expected geometric errors in the prostate region are small, since this sequence uses balanced and symmetrical imaging gradients during acquisition. Furthermore, due to the fat suppression, the boundaries of the prostate are clearly visible and also the high resolution combined with a relatively short acquisition time make it very suitable for use in a clinical setting. The T1 and the T2 are mainly used as diagnostic scans for detecting hemorrhage and tumor localization within the prostate respectively.

4.2.3 Experiments

Phantom tests

We performed phantom tests to see whether the new markers have indeed an increased visibility compared to the conventional markers. We also investigated the shape of the artifact caused by the steel core of the marker. We used the bSSFP MRI scan, since this sequence is the most important when delineating the prostate. During the experiments, the markers were aligned with the main magnetic field in a gelatin phantom. This setup corresponds with the most common orientation of the markers in patients treated for prostate cancer, since the implantation of the markers occurs in the longitudinal direction of the patient. After the phantom study we started implanting the markers into all new prostate cancer patients and studied the artifacts *in vivo*.

Manual marker detection

In order to determine how precise the new markers can be detected, five experienced physicians and physicists marked the location of each of the three implanted markers in 20 patients on all MRI sequences. For all patients the planning CT, the bSSFP, the T1- and the T2-weighted MRI were used. First, the markers are automatically detected on the CT and each marker had its unique identifier assigned per patient. The automatic detection of the markers is based on thresholding the high CT values followed by the calculation of the center of gravity. The accuracy is $0.1\ \text{mm}$ in transversal direction

and $0.3\ \mathrm{mm}$ in axial direction. This difference is caused by the relatively large slice thickness compared to the in-plane resolution (Dehnad *et al.*, 2003).

Subsequently, each observer indicated the corresponding markers in all MRI datasets. The observers were instructed to locate the 3D position of the center of gravity of the marker. An in house developed software package, called Volumetool (Bol *et al.*, 2009), was used. Three orthogonal views of the dataset at hand are presented to the observer, along with a linked cursor. The observers were free to choose the window/level settings. It was also possible to put a marker "between slices". In other words, the observer was not forced to pick the center of a voxel as a marker position. In this way, the position of a marker can be manually interpolated between slices, which makes the whole procedure less sensitive for large voxel sizes.

The final result of the procedure is that we have for each individual marker five 3D positions (from every observer one position) in each MRI sequence. From these five locations, we calculated the mean marker position, and computed for each orthogonal direction the absolute distance between this mean marker and each contributing marker. The mean of these absolute distances is a measure for the interobserver variability for each MRI sequence.

Differences between CT and MRI based marker detection

In current clinical practice, the prostate is delineated on MRI and the markers are extracted from the CT. Registration is used to correlate both datasets. In order to investigate the differences between this procedure and the solely MRI based procedure, we compared the marker positions of the CT based marker detection with the ones based on MRI marker detection.

In order to do this comparison, the markers were all transformed to the same coordinate system and we choose the bSSFP coordinate system as our standard. The T1 and T2 marker positions were directly mapped to the bSSFP coordinate system. Registration was not applied, because the expected registration error (mainly caused by the large slice thicknesses) would be larger than the intra imaging motion. However, the "bSSFP positions" of markers which were extracted from the CT, were obtained by applying the rigid transformation we obtained from the CT-bSSFP registration. This registration was clinically used and was based on mutual information registration, using only small boxes around the prostate in both datasets as its registration volumes.

The measure we used to quantify the differences is comparable to the one described in Section 4.2.3: for each orthogonal direction we first calculated the absolute distance between the CT position and the MRI position of the marker. We did this for all CT-MRI sequence combinations and summarized these results by taking the mean of the absolute distances of each scan combination.

4.3 Results

4.3.1 Marker induced artifacts

In Figure 4.3, the phantom experiment setup (the main magnetic field (B0) with respect to the marker orientation), the signal artifacts of a new marker and a conventional marker are shown. Due to the steel core, ring artifacts are visible around the new marker, whereas the pure gold marker gives only a very weak signal disturbance in the gelatin phantom. Since the ring artifacts are evenly distributed around the marker, the center of the marker can be spotted easily. Although the precise artifacts depend on the orientation of the marker in the magnetic field, the lobed, symmetrical shape remains virtually the same when the marker has an angle of up to 40 degrees with respect to the main magnetic field. Due to the nature of the implantation procedure, such large angles are very rarely observed. The artifact shape is also depicted in Figure 4.4a. Here, three markers are visible in this coronal slice, having the same artifact shape as seen in the phantom experiments.

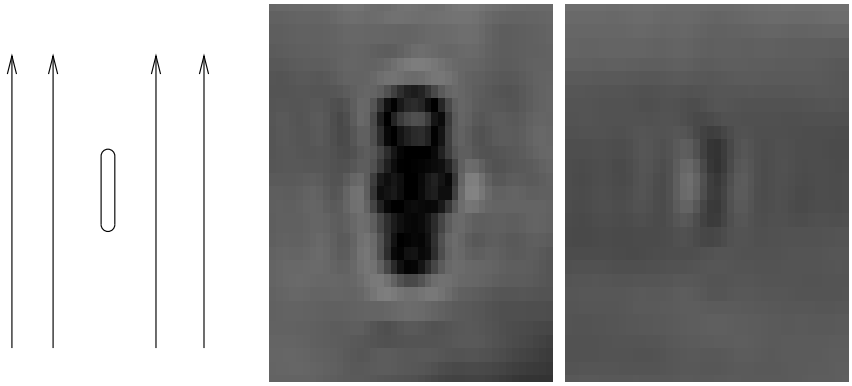

(a) B0 and marker orientation (b) bSSFP, with steel core (c) bSSFP, pure gold

Figure 4.3: Results of visibility experiment in a gelatin phantom.

The new markers contain slightly less gold than the solid gold markers ($3.6\ \mathrm{mm}^3$ versus $3.9\ \mathrm{mm}^3$) and atomic mass of iron is less than the atomic mass of gold (55.84 u versus 196.97 u), but the visibility on EPID remains good (see Figure 4.4b) and they give sufficient contrast for automatic EPID marker extraction algorithms (Harris *et al.*, 2006). Therefore, the markers are standardly used at our department in the same fashion as described by Van der Heide *et al.* (2007).

4.3.2 Interobserver variability

The results of the interobserver variability experiment for the three main axis directions are presented in Table 4.1. The LR-axis corresponds with the lateral direction, the AP-axis corresponds with the anterior-posterior direction and the cranial-caudal direction is presented by the CC-axis. The LR-positions of the markers are detected consistently on all individual MR sequences: the mean absolute distances are small. However, larger

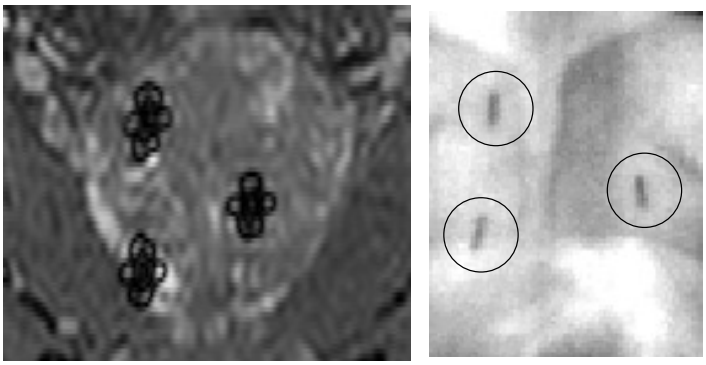

(a) Coronal view bSSFP (b) AP megavolt image

Figure 4.4: Gold markers with steel core *in vivo*.

distances in AP-direction of the T1 and the T2 compared to the bSSFP can be observed. This difference is caused by the elongated (in AP-direction) and therefore circlely asymmetric artifact that is produced by the marker in the transversal plane (see Figure 4.5). This makes it more difficult for an observer to determine the position of the markers the AP-direction. The bSSFP, however, is almost perfectly round, making the decision where to pinpoint the marker easier. As expected, it was more difficult to consistently detect the CC-position of the marker on the T1 and T2 scans. This is caused by the relative thick slices of $4\ \mathrm{mm}$ of these scans.

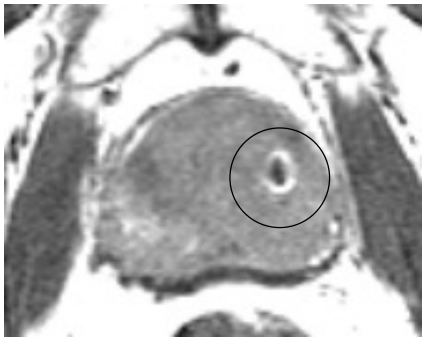

Figure 4.5: Close-up of the T1 artifact. The elongated shape causes a larger interobserver variation in AP-direction.

We also tried to manually detect the pure gold markers, but this failed due to the very poor visibility of these markers. The only way to find the markers in most cases was by projecting the CT marker position into the MRI image and assume that the artifact closest to that projected position was caused by the marker.

Sequence	LR (mm) *mean abs. dist.*	AP (mm) *mean abs. dist.*	CC (mm) *mean abs. dist.*
bSSFP	0.16	0.20	0.30
T1	0.28	0.52	0.95
T2	0.28	0.47	0.88

Table 4.1: The mean absolute distance between the mean marker position and every observed marker position by the five observers on 20 patients, each implanted with three fiducial markers.

Scan combination		LR (mm) *mean abs. dist.*	AP (mm) *mean abs. dist.*	CC (mm) *mean abs. dist.*
bSSFP	CT	0.43	1.44	1.42
T1	CT	0.56	1.84	1.83
T2	CT	0.46	1.63	1.64

Table 4.2: The mean absolute distance of all markers, calculated from the distances between the MRI position and the CT position of each marker.

4.3.3 Variability between MRI and CT

Table 4.2 shows the means of the absolute distances between the marker positions found in various MRI sequences and the planning CT, for each orthogonal direction. It shows the effects resulting from the registration which is needed when using a MRI based delineation and a CT based marker detection. In the LR-direction the observer differences of all modality combinations are relatively small: the mean absolute distances are all below $0.6\,\mathrm{mm}$. The rather large mean absolute distance in AP-direction in the T1 sequence can be explained by the interobserver variation as described in Section 4.3.2 and specific registration errors in that direction. In CC-direction the effect of the large slice thickness is also reflected in all combinations involving a T1 or a T2 scan.

Furthermore, it is important to state that, when comparing Table 4.1 with Table 4.2, the variability between the CT and MRI, in which the registration error plays a (major) role, is in all directions and modalities larger than the interobserver variability within the MRI scans.

4.4 Discussion

As shown in section 4.3.2, the interobserver variation of the new markers with the steel core, in combination with the bSSFP, is small. Since the bSSFP is very sensitive to even small amounts of iron, the artifact is clearly visible and has a predictable and distinct symmetrically lobed shape, from which the center of gravity is easily spotted. Furthermore, the 3D spatial resolution of the bSSFP is very high, which makes it even more easy to point out the precise position of a marker. As explained in section 4.2.2, the bSSFP is also very suitable for determining the outline of the prostate and the seminal vesicles. Therefore, it justifies the proposition that the bSSFP sequence is exceedingly suitable

for determining the most important structures needed for tumor position verification during treatment.

Although the new markers are also visible on the T1- and T2-weighted images, detecting the exact marker positions is not that straightforward and consistent compared to the bSSFP. One problem is the poor slice thickness of the scans. Observers have to interpolate the CC-position of the marker and this is the main cause of the large variations we see in that direction. This problem can be solved by longer scanning times (and consequently thinner slices).

The other problem is more fundamental. When different MRI sequences are used, the corresponding artifact of the marker also differs. The artifact changes due to the used readout direction, susceptibility artifacts and the orientation of the marker in the main magnetic field. This can lead to differences in (automatic) detectability of the markers. Although the marker is visible on most MRI sequences, it does not necessarily mean that it is suitable for accurately determining the position of the implanted markers (see section 4.3.2).

When large air pockets are in the rectum near the prostate during MRI acquisition, geometrical errors can be present in the resulting T1- or T2-weighted datasets. These distortions are usually visible close to the rectum-prostate boundary and may obscure the delineation of the prostate. However, with respect to determining the marker positions, the problem is not very important because the markers are placed in the central zone of prostate rather than near the boundary. Note that the bSSFP is not influenced by these geometrical errors.

Although the above problems exists, the distances between the absolute positions found in CT and all MRI sequences are small (see Table 4.2). Especially when keeping in mind that in order to compare two positions of a marker, first a registration matrix is applied. The estimated accuracy for this registration is approximately 1 voxel and this means that the registration error can be as large as $3\ \mathrm{mm}$ due to the CT slice thickness. Since the mean absolute distances are on average well below this maximum (they are all lower than $2\ \mathrm{mm}$), we conclude that the registration step is the most dominant source of errors. The potential marker position shifts play only a minor role in the observed differences: when for instance a large systematic shift would be introduced, the resulting mean displacement errors would be larger than the expected registration error, but this is not the case.

The most important modality combination to look at is the one combining the bSSFP and the planning CT, because in current clinical practice we register the bSSFP to the CT in order to correlate the MRI prostate delineation with the CT based marker positions. As expected, the CC-coordinates are determined more consistently compared to all other combinations, because the slice thickness of the bSSFP is relatively small. The LR-direction is detected more consistently than the AP-direction. This is caused by the larger registration error in anterior-posterior direction: due to different bladder and rectal filling during the separate CT and MRI imaging sessions, it is slightly more difficult to consistently register the prostate in that direction. However, the differences

between the bSSFP and the golden standard using the CT are on average in all directions well below $1.5\ \mathrm{mm}$. Therefore the bSSFP sequence can be used for both delineation of prostate and reliable detection of the fiducial gold markers with steel core.

When comparing Table 4.1 and Table 4.2, it is clear that MRI based delineation and marker detection can reduce the systematic treatment error. As reported before, the differences between the two tables are mainly caused by CT-MRI registration errors. By using only MRI, these errors are no longer in play: the correspondence between the delineation and the marker positions is directly established. Furthermore, we plan to automatically extract the markers from the MRI. In the end we try to obtain the same accuracy as the one achieved by the automatic CT based marker extraction method. This will reduce the systematic error even more. We expect that by using our method we may reach a reduction of the systematic error up-to $1.0\ \mathrm{mm}$ in CC-direction.

When target delineation and marker detection is solely based on MRI, the treatment planning scheme becomes different. For proper dose calculation, a planning CT is still needed. This means that the markers and delineation should be transfered to the planning CT by means of registration, but this registration is not as critical as the one needed when the correlation between the CT markers and an MRI based delineation is established: dose errors resulting from displaced air (outside the body contour or in the rectum) are small and any positional errors with respect to for instance skin markers are corrected by the position verification procedure during the irradiation phase. Consequently, the registration error is no longer systematic (the error remains during the whole treatment), but random.

4.5 Conclusions

In this study we introduced a new fiducial gold marker with a steel core for prostate cancer patients which is visible on most MRI sequences. We demonstrated its use with bSSFP, T1 and T2 scans. We conclude that the bSSFP is most suitable for both delineation of the prostate as well as for accurately detecting the markers. The lobed and symmetric artifact of the marker is clearly visible and makes it easy to point out the center of the marker consistently. Since the detection error is comparable to or lower than the errors made registering the bSSFP to the planning CT, this approach can be used to delineate the prostate and reliably detect the new markers within the same MRI sequence. This can result in a lower overall systematic treatment error.

5

Fast online Monte-Carlo based IMRT planning for the MRL

This chapter is based on:
Bol G.H., Hissoiny S., Lagendijk J.J.W. and Raaymakers B.W. 2012 Fast online Monte Carlo-based IMRT planning for the MRI linear accelerator *Physics in Medicine and Biology* **57** 1375–1385

Abstract

The MRI accelerator, a combination of a 6 MV linear accelerator with a 1.5 T MRI, facilitates continuous patient anatomy updates regarding translations, rotations and deformations of targets and OARs. Accounting for these demands high speed, online IMRT re-optimization. In this paper, a fast IMRT optimization system is described which combines a GPU based Monte-Carlo dose calculation engine for online beamlet generation (GPUMCD) and a fast inverse dose optimization algorithm (FIDO). Tightly conformal IMRT plans are generated for four phantom cases and two clinical cases (cervix and kidney) in the presence of a 0 T and 1.5 T magnetic field. We show that for the presented cases the beamlets generation and optimization routines are fast enough for online IMRT planning. Furthermore, there is no influence of the magnetic field on plan quality and complexity and equal optimization constraints at 0 T and 1.5 T lead to almost identical dose distributions.

5.1 Introduction

The UMC Utrecht (Utrecht, The Netherlands), in cooperation with Elekta (Crawley, UK) and Philips (Best, The Netherlands), is building a MRI linear accelerator for real-time, soft-tissue based position verification and treatment monitoring for image guided radiotherapy. It combines an Elekta 6 MV linear accelerator system with a Philips 1.5 T MRI scanner (Lagendijk *et al.*, 2002; Raaymakers *et al.*, 2009). During treatment delivery the dose distribution of such a system is influenced by the presence of the magnetic field of the MRI. The magnetic field causes a decreased build-up distance, a shifted asymmetric penumbra and the electron return effect (ERE) (Raaymakers *et al.*, 2004; Raaijmakers *et al.*, 2005a; Kirkby *et al.*, 2008, 2009; Oborn *et al.*, 2009, 2010). The first order compensation of these effects can be done by using opposing beams as described by

(Raaijmakers *et al.*, 2005a). Further compensation requires addition of intensity modulated radiotherapy (IMRT).

In order to deliver accurate IMRT, the effects of the magnetic field have to be incorporated during (online) treatment optimization. Most modern treatment planning systems use pencil beam or superposition/convolution (Mackie *et al.*, 1987; Liu *et al.*, 1997) such as collapsed cone techniques (Ahnesjö, 1989) for dose calculation. However, due to the surface orientation dependency of the ERE effect at large mass density changes, specifically at tissue-air boundaries (Raaijmakers *et al.*, 2007b), these techniques are not suitable for accurate dose calculation for the MRI accelerator.

Monte-Carlo based dose calculation in the presence of a magnetic field in combination with IMRT optimization is feasible as shown by Raaijmakers *et al.* (2007a). They used an inverse IMRT treatment optimization approach based on pre-calculated Monte-Carlo based beamlet dose distribution kernels to obtain adequate homogeneous target coverage and sparing of organs at risk (OAR). However, the amount of calculation time (several days with a cluster of 100 CPUs for a 7 beam prostate IMRT plan) makes this approach clinically impractical, both for conventional pre-treatment treatment planning as well as for online pre-delivery treatment planning. As for now, other commercially available Monte-Carlo based treatment planning systems do not implement magnetic fields.

With the MRI accelerator it will be possible to get continuous patient anatomy updates (translations, rotations and deformations of targets and OARs) and accounting for this demands high speed, online IMRT re-optimization. Conventional linacs can only compensate for target translations and small rotations by changing the table, gantry and/or collimator settings pre-treatment. A daily re-optimization of the treatment plan based on the online MRI images can fully account for these patient position uncertainties. Consequently, there is a need for an IMRT optimization system which is fast and robust enough to generate daily a clinically approved plan.

In this work we present an online IMRT optimization system for the MRI accelerator. It uses a GPU based Monte-Carlo dose calculation engine (Hissoiny *et al.*, 2011a,b) for online beamlet generation and a fast inverse dose optimization algorithm (Goldman *et al.*, 2009). We describe a system which is able to generate tightly conformal IMRT plans for four phantom cases and two clinical cases (cervix and kidney) in the presence of a 0 T and 1.5 T magnetic field. Furthermore, we show that there is no influence of the magnetic field on plan quality and complexity.

The differences between the 0 T plans and 1.5 T plans are evaluated by the γ criterion (Low *et al.*, 1998) and the D_{99} target coverage. Furthermore, we show that the beamlets generation and optimization routines are very fast and therefore usable for online IMRT planning.

5.2 Materials and Methods

5.2.1 Beamlet generation

The IMRT optimization exists of two steps: first the anatomy specific beamlets for each gantry angle have to be calculated and the second step is the inverse optimization of the beamlets weights. The beamlets were calculated by GPUMCD (Hissoiny *et al.*, 2011a). GPUMCD is a fast and accurate GPU-oriented Monte-Carlo dose calculation platform which also implements magnetic fields (Hissoiny *et al.*, 2011b).

Before the beamlets are generated, the CT is resampled to the dose scoring grid with voxels of $2.0 \times 2.0 \times 2.0\ \mathrm{mm}^3$. The beamlets themselves are $5.0 \times 5.0\ \mathrm{mm}^2$ at isocenter. Since Monte-Carlo calculation requires that the various tissue types have to be properly characterized, the Houndsfield units of the CT are used to generate a composition phantom using four tissue types with specific elemental composition (air, lung, soft tissue and bone) and the Houndsfield units are also converted to mass density (Jiang *et al.*, 2007).

Instead of calculating all beamlets for the maximum field size of the MRI linac (which is $56 \times 24\ \mathrm{cm}^2$ at isocenter) for each gantry angle, we only calculate the beamlets which deliver dose to at least one of the target volumes in order to reduce calculation time. A spherical margin of $0.4\ \mathrm{cm}$ is added to the targets with the constraint that the margin stays within the body contour and when the mid-line of a beamlet hits the artificial target, the beamlet is included into the Monte-Carlo simulation. This beamlet selection step is performed by a standard ray casting algorithm (Foley *et al.*, 1994).

Each beamlet was generated with 1.58×10^6 histories, with and without the presence of a $1.5\ \mathrm{T}$ magnetic field, resulting in a statistical accuracy of approximately 1.8% (for all voxels with dose more than 20% of dose maximum). Calculation was performed on two Nvidia® GeForce GTX 480 graphics cards. The current GPUMCD implementation can calculate at most *n* beams in parallel where *n* is the number of GPU cores available.

The analytical source definition had the same spectrum as a $6\ \mathrm{MV}$ beam of a Elekta SLi linear accelerator, which is close to the source spectrum of the linear accelerator which will be used in the MRI linac system. Output factors were not included into the simulation, since there is no sequencing included in our current setup.

5.2.2 IMRT optimization

The basis of the IMRT optimization algorithm was the fast inverse dose optimization (FIDO) as described by Goldman *et al.* (2009). This method generates comparable, and often better IMRT plans, than those obtained by using standard optimization techniques that are considerably slower (Goldman *et al.*, 2009). It reformulates the objective function for the optimization of large number of beamlets such that the optimization problem is reduced to a linear set of equations. The optimal beamlet weights are found through matrix inversion. Due to the reformulation of the objective function these weights are guaranteed to be non-negative.

We implemented the algorithm in such a way that, for every target voxel, the prescribed dose and the associated importance weight can be set individually. Also, the importance weight of each OAR voxel can be set case-by-case. This refinement is used by the "dynamic importance weight assignment (DIWA)" routine as described below.

When assigning the same importance weights for complete structures, we use volume weighting in order to stay independent of the structure volumes. This allows the use of the same importance weights for comparable target cases or for automatic re-optimization purposes and is implemented in order to reduce the amount of user interaction.

DIWA was added to the algorithm: after a first run of FIDO with purely user defined constraints for complete structures, the calculated dose of the targets and OARs is evaluated and when certain parts of the structures do not meet a clinical dose criterion (such as maximum dose or minimum dose), the importance weights are adjusted in an unsupervised manner, according to predefined rules. The optimization loop is then executed for the second time. This fine-tuning step gives more control over the optimization result without the cost of added user interaction.

A commonly used DIWA rule removes hotspots and beamlet streaking artifacts within the body: OAR voxels with a relatively high dose are given an higher weight in order to reduce the dose on these locations. Figure 5.1 gives a phantom example of the effect of this rule on the dose distribution. The setup of the phantom is discussed in section 5.2.3.

Fast matrix inversion was implemented by using the open source C++ linear algebra library Armadillo (Sanderson, 2010) combined with the Intel® Math Kernel Library. Calculation was performed on a quad core 64-bit Intel® i5-2400 CPU, all cores running at $3.10\ \mathrm{GHz}$. The operating system was Debian Linux 6.0.3.

5.2.3 Anatomy definitions

The basis of all phantom anatomies was formed by a $40 \times 20 \times 30\ \mathrm{cm}^3$ water phantom. The first phantom consist of only a spherical target with a diameter of $5\ \mathrm{cm}$, which is placed in the center of the water phantom. The prescribed dose to the target was $75\ \mathrm{Gy}$. The second phantom has an additional spherical boost volume with a diameter of $3\ \mathrm{cm}$ in the center of the first target sphere and had a prescribed dose of $85\ \mathrm{Gy}$. The third phantom adds a OAR as a cylinder with a diameter of $4\ \mathrm{cm}$ and a length of $6\ \mathrm{cm}$, which slightly overlaps with the target area.

The final phantom used is a horseshoe like target area with an OAR and an air cavity inside. The target is created by removing a block of $4.4 \times 4.2 \times 6.0\ \mathrm{cm}^3$ from a larger block of $8.4 \times 6.2 \times 6.0\ \mathrm{cm}^3$. At the center of the cavity of the horseshoe, a cylinder of air with a diameter of $3.2\ \mathrm{cm}$ and a length of $10.0\ \mathrm{cm}$ was placed which was surrounded by a cylindrical OAR with a diameter of 4 cm and a length of $6\ \mathrm{cm}$. The target prescribed dose was $75\ \mathrm{Gy}$.

The patient anatomies used were a cervical cancer patient and a kidney cancer patient.

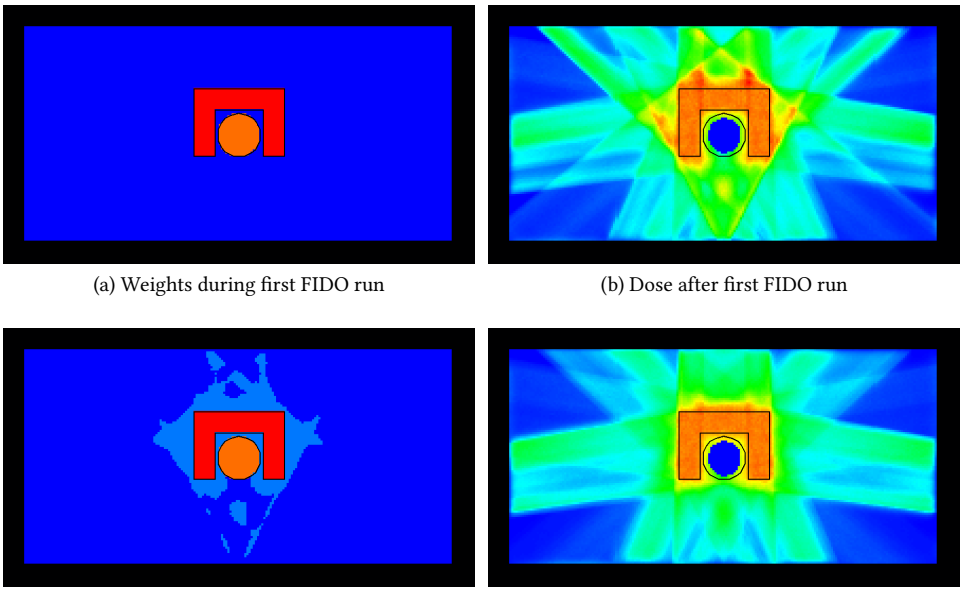

(a) Weights during first FIDO run

(b) Dose after first FIDO run

(c) Weights during second FIDO run

(d) Dose after second FIDO run

Figure 5.1: Example of dynamic importance weight assignment (DIWA): after the first run of FIDO, high dose areas are detected outside the target. The importance weights in these areas are automatically elevated. After the second run of FIDO the hotspots are significantly reduced.

The cervical tumor was choosen because it represents a case with a large target. The kidney case represents a small boost target. For both cases the clinical CT and delineations were used and the prescribed dose were $45\ \mathrm{Gy}$ and $25\ \mathrm{Gy}$ to the planning target volume (PTV), respectively. The OARs of the cervical cancer case were the rectum, bladder, and the bowel. The OARs of the kidney case were the kidneys, the spinal cord, the bowel and the spleen. A graphical representation of all anatomies used are shown in Figure 5.2 and Figure 5.3.

5.2.4 Plan setup and verification

All cases were manually planned with beamlets calculated in the presence of a magnetic field of $1.5\ \mathrm{T}$. After this, all cases were automatically planned without the magnetic field, with exactly the same constraints as they were found manually for the $1.5\ \mathrm{T}$ cases. The phantom cases and the cervix case were planned with seven fixed gantry angles of 0, 50, 100, 155, 205, 260 and 310 degrees. The kidney case was planned with 12 equidistant gantry angles starting at 0 degrees.

Since the isocenter of the MRI linac is in the middle of the bore of the MRI and the table height is also fixed, all initial isocenters were placed according to these specifications: they were placed in the transversal plane through the center of gravity of the target structure, at the central body axis, $14\ \mathrm{cm}$ above the treatment table.

The main manual planning criterion was that 99% of the target volume received at least 95% of the prescribed dose (D_{99}), while creating as steep as possible dose gradients outside the targets to ensure maximum OAR sparing. In order to get steep dose gradients around the targets, the importance weights of the OARs were elevated until the D_{99} criterion was just satisfied. Figure 5.2 and Figure 5.3 show the resulting dose distributions.

The resulting dose distributions calculated with and without the presence of the magnetic field were compared using the $2\%/2\ \mathrm{mm}$ γ criterion. Furthermore, the D_{99} was determined, and the calculation time for the beamlets generation per gantry angle as well as the IMRT optimization routine was recorded.

In order to investigate possible complexity differences between the optimized beamlet weights maps found with and without a magnetic field, the modulation index (Webb, 2003) for each gantry angle was calculated. The modulation index quantifies the variations between adjacent beamlet weights map values, and this determines the degree of difficulty MLC-based systems have to deliver such a map. Afterwards, the modulation index was normalized to 1 for the $0\ \mathrm{T}$ case. This normalization was also applied to the $1.5\ \mathrm{T}$ case, giving the relative modulation index (RMI). If the RMI is significantly larger than 1 for the $1.5\ \mathrm{T}$ cases, sequencing such plans will be harder and treatment delivery will also be more difficult.

5.3 Results

In Figure 5.2 and 5.3, the dose distributions are presented for both the $0\ \mathrm{T}$ and $1.5\ \mathrm{T}$ cases. All cases show a conformal dose distribution with steep dose gradients tightly around the target structures. Also the corresponding γ distributions are presented for all voxels having a dose of more than 10% of the dose maximum.

The relative difference between the D_{99} values at $0\ \mathrm{T}$ and the D_{99} values at $1.5\ \mathrm{T}$ was calculated and the results are presented in Table 5.1. The differences are minimal in all cases: the absolute relative difference is always smaller than 0.3%. This means that the target coverage with and without the presence of a magnet field and using the same optimization constraints are virtually equal.

Case	*% difference* D_{99}
Simple phantom, (target only)	0.00
Simple phantom, *target* (target, boost)	0.15
Simple phantom, *boost* (target, boost)	0.26
Simple phantom, *target* (target, boost, oar)	0.21
Simple phantom, *boost* (target, boost, oar)	0.09
Horseshoe phantom	0.00
Cervix	0.04
Kidney	0.09

Table 5.1: The relative D_{99} difference between the $0\ \mathrm{T}$ and the $1.5\ \mathrm{T}$ case. Note that the D_{99} for the simple phantom cases with two targets are given separately for the target and boost structure.

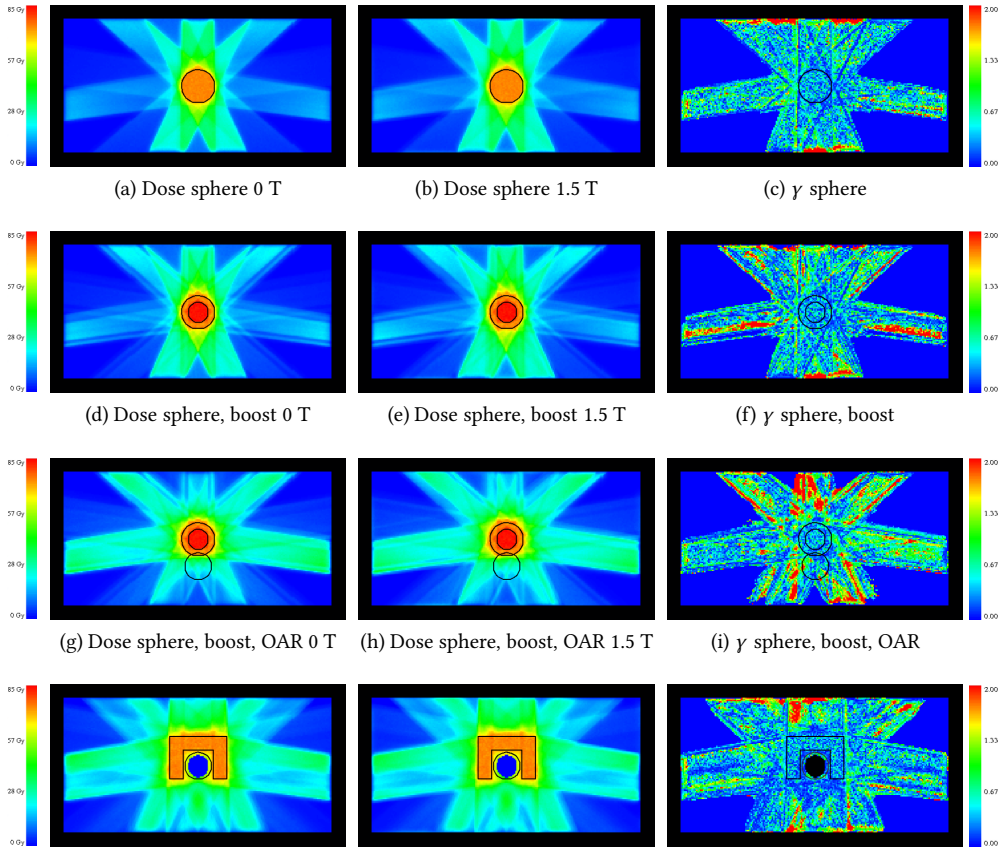

(a) Dose sphere 0 T (b) Dose sphere 1.5 T (c) γ sphere

(d) Dose sphere, boost 0 T (e) Dose sphere, boost 1.5 T (f) γ sphere, boost

(g) Dose sphere, boost, OAR 0 T (h) Dose sphere, boost, OAR 1.5 T (i) γ sphere, boost, OAR

(j) Dose horseshoe 0 T (k) Dose horseshoe 1.5 T (l) γ horseshoe

Figure 5.2: Dose and γ distributions of the phantom cases.

The results of the γ analysis are presented in Figure 5.4 and Table 5.2. Figure 5.4 shows histograms of the γ values of all target voxels and OAR voxels from all cases for 0 T and 1.5 T. Almost all voxels with a dose of more than 50% of the maximum dose satisfy the $2\%/2$ mm γ criterion, since they have a $\gamma \leq 1$. The average γ value for all target voxels and all OAR voxels was 0.33 and 0.30 respectively. Table 5.2 presents the percentage of target and OAR voxels which have a $\gamma \leq 1$ for each case separately and for all cases together. The horseshoe phantom has its OAR adjacent to the air cavity of the phantom and near the high dose area. Because of the ERE effect, the dose in this area will be larger at 1.5 T than at 0 T which results in slightly larger γ values.

Since we want to use our approach in a online setting, calculation time of both the beamlet generation and the optimization routines are very important. Table 5.3 presents the average execution times per gantry angle of each case for 0 T and 1.5 T, together with the average number of beamlets per gantry angle. The beamlet selection step reduces the number of calculated beamlets per gantry angle significantly: without this step 5376

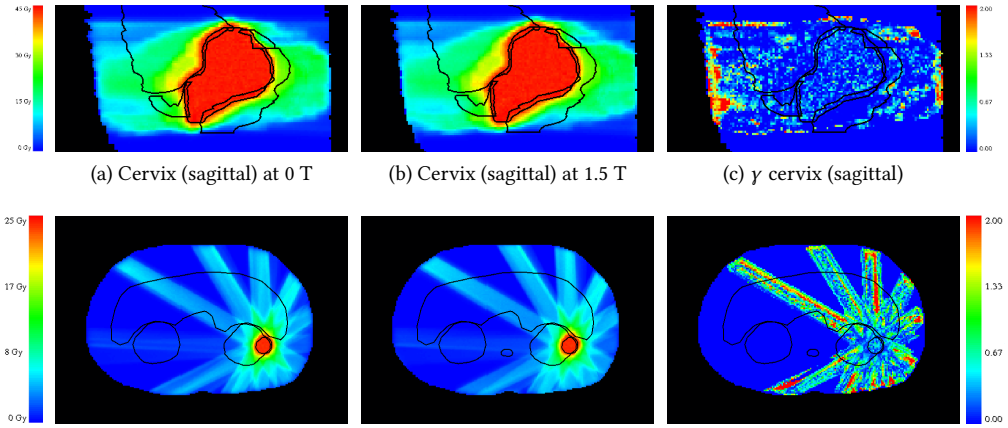

(a) Cervix (sagittal) at 0 T (b) Cervix (sagittal) at 1.5 T (c) γ cervix (sagittal)

(d) Kidney (transversal) at 0 T (e) Kidney (transversal) at 1.5 T (f) γ kidney (transversal)

Figure 5.3: Dose and γ distributions of the clinical cases.

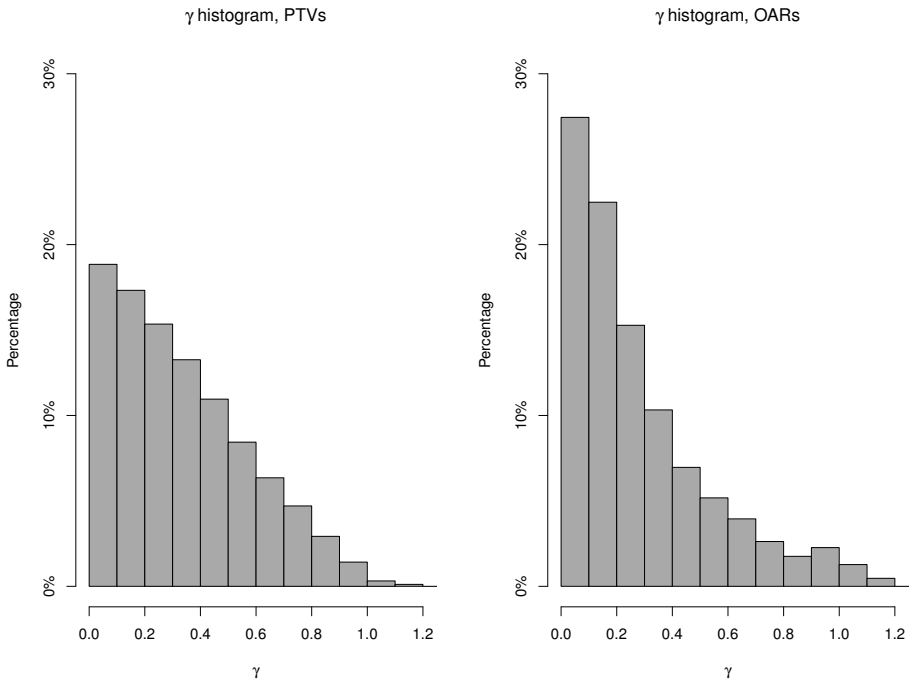

Figure 5.4: Histograms of γ values for all PTV and OARs voxels with dose greater than 50% of D_{max}.

Case	$\gamma \leq 1$ *PTV*	$\gamma \leq 1$ *OAR*
Simple phantom (target)	99.6%	—
Simple phantom (target, boost)	99.4%	—
Simple phantom (target, boost, oar)	99.4%	97.5%
Horseshoe phantom	99.5%	90.3%
Cervix	99.5%	97.6%
Kidney	100.0%	99.7%
All cases	99.5%	96.9%

Table 5.2: Percentage of voxels with dose greater than 50% of D_{max} having $\gamma \leq 1$ for all cases.

beamlets should be generated for each gantry angle, but now for a relatively large target as the cervix, on average 368 beamlets per gantry angle were needed. As expected, the beamlet generation step is dependent on the magnetic field strength (Hissoiny *et al.*, 2011b): at 1.5 T it takes roughly twice as much time as needed when no magnetic field is present, but still for a rather large clinical case as the cervix the total calculation time already stays below 2.5 minutes when using the same number of GPUs as there are gantry angles, given the described GPU hardware.

Case	*Avg beamlets per gantry angle*	*Calc time at 0 T (s)*	*Calc time at 1.5 T (s)*
Simple phantom	284	30.27	58.72
Horseshoe phantom	283	30.25	59.22
Cervix	368	57.85	133.99
Kidney	38	4.13	12.64

Table 5.3: Average number of beamlets and GPUMCD calculation time per gantry angle in seconds. Note that for the three simple phantom cases the beamlets are reused, since the total target area is the same for all cases.

The average timing results of the optimization step are shown in Table 5.4. There is no influence of the magnetic field present in these results, only the number of beamlets and whether DIWA was used is important. All cases could be optimized well within 7 seconds.

The complexity differences of the optimized beamlet weight maps are expressed in Table 5.5. For all cases the average RMI is close to 1 with only a small standard deviation. This means that the complexity of the weight maps at 1.5 T is comparable with the ones optimized at 0 T.

5.4 Discussion

With the current GPU and CPU hardware we are able to optimize a new set of Monte-Carlo based beamlets within minutes: when having one GPU per gantry angle available, a complete 7 beam cervix beamlet generation and IMRT optimization at 1.5 T takes

Case	*Calc time at 0 T (s)*	*Calc time at 1.5 T (s)*
Simple phantom (target)	1.46	1.36
Simple phantom (target, boost)	1.38	1.42
Simple phantom (target, boost, oar)[1]	2.96	2.77
Horseshoe phantom[1]	4.25	3.91
Cervix	6.72	6.56
Kidney	1.06	1.02

[1] Optimized with DIWA

Table 5.4: Average optimization calculation time per case in seconds.

Case	*RMI average (SD)*
Simple phantom (target)	1.00(0.04)
Simple phantom (target, boost)	0.98(0.02)
Simple phantom (target, boost, oar)	0.98(0.05)
Horseshoe phantom	0.99(0.02)
Cervix	1.00(0.01)
Kidney	1.00(0.01)
All cases	0.99(0.03)

Table 5.5: Relative modulation index (RMI), averaged over all fluencemaps, by case and for all cases.

about 2 minutes and 21 seconds. A kidney tumor takes a total of 14 seconds. Both are already fast enough for a daily pre-delivery re-optimization regime and for the kidney case, even an intrafraction re-optimization is possible. Faster hardware, improved beamlet calculation parallelization and moving the FIDO algorithm from the CPU to the GPU will directly reduce the execution time and data streaming efficiency of the system even more. For instance, when using the successor of the GPU used in this paper (Nvidia® GeForce GTX 580), the GPUMCD engine is expected to run 2.5 times faster.

Also the differences between optimizing in the presence of a 0 T and 1.5 T magnetic field are minimal: the target and the high dose OAR areas receive comparable amount of dose in terms of D_{99} and γ values, although at 1.5 T the electron return effect (ERE) is present at the skin-air interface (see Figure 5.2 and 5.3). Since air cavities did not play a very large role in this research, it may become more of an issue when going to targets in the lung and the head-and-neck region, although the use of IMRT optimization with multiple gantry angles will limit this effect as long as the target is located within the crossfire of the beams, as shown by Raaijmakers *et al.* (2007a).

We showed that when the optimization constraints of the 1.5 T cases were reused for the 0 T cases, the resulting dose distributions were almost identical, even when using DIWA. This suggests that the optimization routine is very robust regarding the type and/or setup of beamlets used. Therefore, we expect that the method can also

accurately compensate for online target and OAR translation, rotation and deformation (determined from the daily MRI-based patient anatomy) by re-optimization of the treatment plan, without the need of manually changing the constraints, which were determined pre-treatment. Whether this is the case, will be investigated in the future.

The system currently relies on pre-treatment CT data for the tissue properties needed for the Monte-Carlo calculation. When generating online beamlets, the pre-delivery MRI scan has to be registered to this CT. At first, we will use rigid registration, since it can be performed within seconds. However, a completely MRI based procedure is preferred and this will be investigated in the future, along with other registration methods, such as deformable, non-rigid registration for compensating for daily anatomical and setup variations. Our method can also be used in combination with a conebeam CT instead of a MRI. The advantage is that the tissue properties for beamlet generation can be derived directly from the conebeam CT, although the HU to density conversion is still difficult (Rong *et al.*, 2010; Niu *et al.*, 2010). Also the beamlet calculation time is shorter, since no magnetic field is present.

Since the focus of this paper is on the beamlet generation and IMRT optimization, issues regarding sequencing were not investigated. One can expect that by adding sequencing to the system, it adds extra calculation time and the resulting dose distribution will degrade from the results shown here, since it adds another discretization step to the process. However, the RMI results show that the optimized beamlet weight maps for 0 T and 1.5 T are equally complex, so we expect that the performance of a sequencer for the MRI accelerator in terms of deliverability will be same as the ones used for conventional linacs.

5.5 Conclusions

In this paper we described an IMRT planning system which correctly incorporates the magnetic field of a MRI accelerator, and is fast enough to perform online re-optimization. We showed that for the cases presented the presence of the magnetic field does not have an adverse effect on plan quality and complexity and that equal optimization constraints at 0 T and 1.5 T lead to almost identical dose distributions. The system also will be an invaluable research tool to further investigate IMRT planning for the MRI linear accelerator, especially for targets near air cavities which are probably more affected by the ERE effect. In the future, the system could be used to compensate for target and OAR translation, rotation and deformation and could handle continuous online patient anatomy changes.

6

Compensating for the impact of non-stationary spherical air cavities on IMRT dose delivery in transverse magnetic fields

This chapter is based on:
Bol G.H., Lagendijk J.J.W. and Raaymakers B.W. 2015 Compensating for the impact of non-stationary spherical air cavities on IMRT dose delivery in transverse magnetic fields *Physics in Medicine and Biology* **60** 755–768

Abstract

With the development of the 1.5 T MRI linear accelerator and the clinical introduction of the 0.35 T ViewRay^{TM} system, delivering intensity-modulated radiotherapy (IMRT) in a transverse magnetic field becomes increasingly important. When delivering dose in the presence of a transverse magnetic field, one of the most prominent phenomena occurs around air cavities: the electron return effect (ERE). For stationary, spherical air cavities which are centrally located in the phantom, the ERE can be compensated by using opposing beams configurations in combination with intensity-modulated radiotherapy (IMRT). In this paper we investigate the effects of non-stationary spherical air cavities, centrally located within the target in a phantom containing no organs at risk, on IMRT dose delivery in 0.35 T and 1.5 T transverse magnetic fields by using Monte Carlo simulations. We show that IMRT can be used for compensating ERE around those air cavities, except for intrafraction appearing or disappearing air cavities. For these cases, gating or plan re-optimization should be used. We also analyzed the option of using IMRT plans optimized at 0 T to be delivered in the presence of 0.35 T and 1.5 T magnetic field. When delivering dose at 0.35 T, IMRT plans optimized at 0 T and 0.35 T perform equally well regarding ERE compensation. Within a 1.5 T environment, the 1.5 T optimized plans perform slightly better for the static and random intra- and interfraction air cavity movement cases than the 0 T optimized plans. For non-stationary spherical air cavities with a baseline shift (intra- and interfraction) the 0 T optimized plans perform better. These observations show the intrinsic ERE compensation by equidistant and opposing beam configurations for spherical air cavities within the target area. IMRT gives some additional compensation, but only in case of correct positioning of the air cavity according to the IMRT compensation. For intrafraction appearing or disappearing air cavities this correct positioning is absent and gating or plan re-optimization should be used.

6.1 Introduction

At the UMC Utrecht (The Netherlands), a new radiotherapy treatment system is being developed, which combines a 8 MV linear accelerator (Elekta AB, Sweden) and a 1.5 T MRI scanner (Philips, The Netherlands). This MRI linear accelerator (MRL) will enable online visualization and thus position verification of the tumor, even during beam-on (Raaymakers *et al.*, 2009). The current technical prototype which employs a 6 MV accelerator can deliver IMRT plans and supports gating and tracking (Crijns *et al.*, 2011, 2012b).

Due to the presence of a transverse magnetic field, the radiation beam has a decreased build-up distance and a shifted, asymmetrical penumbra (Raaymakers *et al.*, 2004). Even more importantly, electrons leaving the tissue traverse an arc-shaped path back into the tissue, which results in a increased dose at tissue-air interfaces (Raaijmakers *et al.*, 2005a; Kirkby *et al.*, 2008; Oborn *et al.*, 2009, 2010; Yang *et al.*, 2013). This electron return effect (ERE) and the reduced build-up distance depend profoundly on the entrance or exit surface orientation, as described by Raaijmakers *et al.* (2007b). This paper also demonstrated that a first order compensation of ERE around a static air cavity can be accomplished by using opposing beams. Additional ERE compensation can be achieved by using intensity-modulated radiation therapy (IMRT) (Raaijmakers *et al.*, 2007a).

In this paper we investigate the effects of non-stationary spherical air cavities, centrally located within the target in a phantom containing no organs at risk, on IMRT dose delivery in magnetic fields by using Monte Carlo simulations. More specifically, we will look at random air cavity movements and baseline shifts, both inter- and intrafraction. These shift types represent air cavity movement due to respiration in the head-and-neck region and air cavity movement due to patient relaxation in the pelvic region respectively. Furthermore, the intrafraction effects of an appearing or disappearing air cavities are investigated, which represents for instance appearing or disappearing gas pockets in the rectum. By using spherical air cavities we can investigate all air-surface orientations at once, therefore maximizing the influence of the ERE on the dose distribution.

We explore strategies which are less sensitive to or could minimize the air cavity effects on the dose distribution in the presence of a magnetic field. The opposing beams strategy is investigated. Also the beam setup of the ViewRay^{TM} system is included in this paper. The ViewRay^{TM} system combines three equidistant ^{60}Co beams setup with an open 0.35 T MRI system. The setup of Fallone *et al.* (2009), which combines a biplanar 0.2 T MRI with a 6 MV linac is not included in the paper, although the results of the ViewRay^{TM} setup can be easily extrapolated to this system.

Due to ERE compensation, IMRT plans optimized for a static air cavity in the presence of a magnetic field have a higher degree of fluence modulation compared to IMRT plans optimized at 0 T. The extra modulation will most likely result in extra dose differences when delivering these plans with non-stationary air cavities. Therefore we compared IMRT plans optimized with and without the magnetic field present, while delivering them in the presence of a magnetic field. This way, the robustness against

non-stationary air cavities for the two optimized plan types can be investigated.

To make fair comparisons possible, all Monte Carlo simulations were performed for 0 T, 0.35 T, and 1.5 T. The 0 T dose distributions are used as reference. The aim of the paper is to understand the impact of non-stationary air cavities on the dose distributions in a transverse magnetic field, and to investigate potential strategies to minimize this influence.

6.2 Materials and Methods

6.2.1 Phantom definitions and IMRT optimization

The base phantom consists of a cube of air with dimensions of $40 \times 40 \times 40$ cm^3. In the center of this cube a $30 \times 30 \times 30$ cm^3 cube of water is placed. In the center of the water cube the target structure is defined as a cylinder with a radius of 6 cm and a length of 12 cm. The air cavity used in all experiments is a sphere with a radius of 2 cm. By using such a sphere, all air-tissue orientations can be investigated at once and the air cavity is large enough for electrons to curve back into the tissue when a transverse magnetic field is present. The reference position of the air cavity is in the center of the phantom. All dose calculations were performed on a $2.0 \times 2.0 \times 2.0$ mm^3 grid. For clarity, the air around the water phantom is not shown in the figures. Furthermore, all (difference) images shown in this paper are through the central transversal slice of the phantom and the magnetic field always points into the page. Figure 6.1 shows a dose distribution, with the spherical air cavity at reference position.

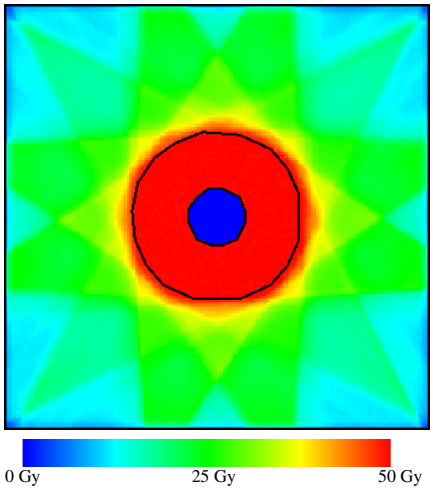

Figure 6.1: Dose distribution with a spherical air cavity, optimized and delivered at 1.5 T.

The prescribed dose was 50 Gy inside and 0 Gy outside the target. Twelve equidistant beams were used during optimization, starting at beam angle $0°$. From these, three delivery modes can be derived: sequential beam delivery, simultaneous opposing beams delivery, and simultaneous delivery using three equidistant beams. We used the treat-

ment planning system as described by Bol *et al.* (2012). It has a GPU based Monte Carlo dose dose engine (GPUMCD) (Hissoiny *et al.*, 2011a,b) which can incorporate the effects of different magnetic field strengths and it has a fast inverse dose optimizer (FIDO) (Goldman *et al.*, 2005, 2009), which can generate tightly conformal fluence-based IMRT plans. The $6\ \mathrm{MV}$ energy spectrum of the MRL prototype was used for all simulations, which was derived from initial beam measurements and Monte Carlo simulations. The direction of the magnetic field was along the positive z-axis (perpendicular to the transverse plane) and was fixed for all simulations.

6.2.2 No air cavity and static air cavity experiments

We first optimized six dose distributions: without an air cavity and with the static air sphere at reference position, both setups at $0\ \mathrm{T}$, $0.35\ \mathrm{T}$ and $1.5\ \mathrm{T}$. In order to interpret the non-stationary cases more easily, the results of the base experiments are also presented by showing the relative dose differences between the $0.35\ \mathrm{T}$ and the $1.5\ \mathrm{T}$ results and the $0\ \mathrm{T}$ reference results.

6.2.3 Random moving air cavity experiments

In these experiments the static optimized $0\ \mathrm{T}$, $0.35\ \mathrm{T}$, and the $1.5\ \mathrm{T}$ plans were delivered at the corresponding magnetic field strength on phantoms with 12 randomly placed air cavity positions. For each position, every x-, y- and z-coordinate of the center of the air cavity was drawn of a Gaussian distribution with a mean of 0 and a σ of $4\ \mathrm{mm}$, and discretized to the nearest dose grid position. This ensures that the air cavity stays within the high dose region at all times.

Interfraction random air cavity movement was simulated by delivering each plan 12 times on the phantoms with the 12 different air cavity positions. For intrafraction random air cavity movements the delivered dose was calculated by changing the anatomy after each delivered (sequential) beam. The latter was repeated for the opposing beams and the three equidistant beams strategy. Note that the results of the interfraction movements are not affected by the choice of delivery strategy, therefore these experiments were not performed.

Since in these experiments the exact positions of the air cavities were known, the delivered dose distributions are rigidly transformed back to the reference position. By doing this is, it becomes possible to compare the relative dose differences between the $0.35\ \mathrm{T}$ and the $1.5\ \mathrm{T}$ results and the $0\ \mathrm{T}$ reference results. Note that due to the discretization step after selecting the new random air cavity position, no re-sampling of the dose distributions was needed. This avoids smoothing of any strong dose effects.

6.2.4 Shifting air cavity experiments

The shifting air cavity experiments are similar to the ones described in section 6.2.3, except the air cavity does not move in a random fashion around the reference position but it starts at the reference position and descends in twelve steps of $2\ \mathrm{mm}$ in y-direction. This mimics air cavity behavior observed for instance in patients who relax during a fraction or during the course of treatment.

6.2.5 Appearing/disappearing air cavity experiments

The effect of a suddenly appearing or disappearing air cavity during a fraction is also simulated. To maximize the effects, the air cavity was present at the reference position half of the fraction for each experiment. During the other half no air cavity was present.

For the appearing experiments the optimized plans without an air cavity were used, for the disappearing ones the optimized plans with an air cavity were used. Also the same compensating strategies were investigated by delivering the fraction using opposing or three equidistant beams.

6.2.6 0 T optimized plans, delivered at 0.35 T and 1.5 T

All experiments of section 6.2.2 to section 6.2.5 were repeated by using the 0 T optimized plans, and delivering them in the presence of a 0.35 T and 1.5 T magnetic field. This way, the results of 0 T optimized plans can be compared to the ones optimized in the presence of a magnetic field.

6.3 Results

6.3.1 No air cavity and static air cavity experiments

Figures 6.2a and 6.3a show the relative differences between the 0 T optimized plan, delivered at 1.5 T and the corresponding 0 T optimized and delivered plan, without and with the spherical air cavity respectively. The ERE is visible at the border of the water phantom: scattered electrons curve back into the tissue resulting in 20 to 30 % higher local dose, regardless of the magnetic field strength.

The star shaped pattern is a result of the shifted, asymmetric penumbra. The difference in target coverage without the air cavity is within 1 % for all examined cases. Figure 6.3a shows shows a slight ERE effect of about 1 %, just around the air cavity. The other static air cavity cases do not show such an ERE effect.

Although the local relative differences can be quite large (especially a the border of the phantom), the resulting dose volume histograms (DVH) are almost identical for all cases (see Figure 6.2a and 6.2b).

6.3.2 Random moving air cavity experiments

When the plan is optimized and delivered at the same magnetic field strength, the target coverage is comparable with the target coverage at 0 T.

When delivering the 0 T plan at 0.35 T and 1.5 T, the results are similar to the ones described in section 6.3.1: for the 0.35 T case (see Figure 6.4a) the target coverage does not differ from the 0 T case, but the 1.5 T case shows a slight underdosage around the air cavity, on average -0.95 %±0.68 at the air-tissue interface (see Figure 6.4b).

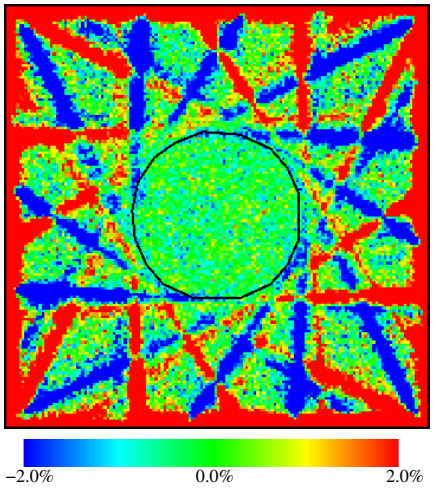

(a) Optimized: 0 T, delivered: 1.5 T

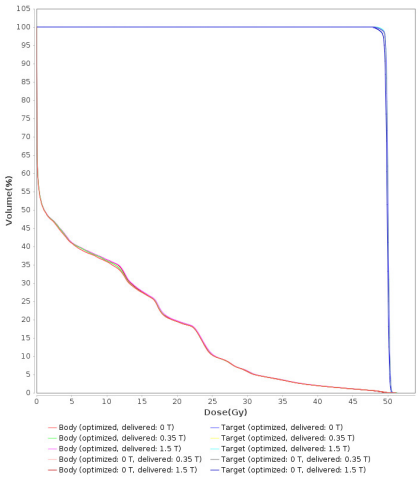

(b) DVH

Figure 6.2: Static results, without an air cavity. The left figure shows the relative differences between the 0 T optimized plan, delivered at 1.5 T and the corresponding 0 T optimized and delivered plan. The right figure shows all DVH of the investigated cases.

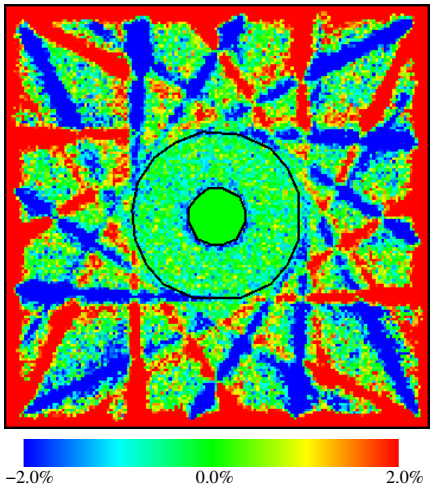

(a) Optimized: 0 T, delivered: 1.5 T

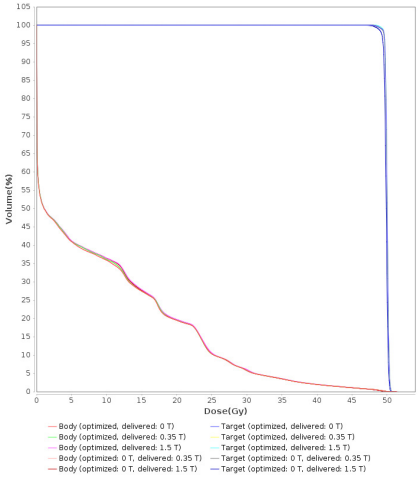

(b) DVH

Figure 6.3: Static results, with an air cavity. The left figure shows the relative differences between the 0 T optimized plan, delivered at 1.5 T and the corresponding 0 T optimized and delivered plan. The right figure shows all DVH of the investigated cases.

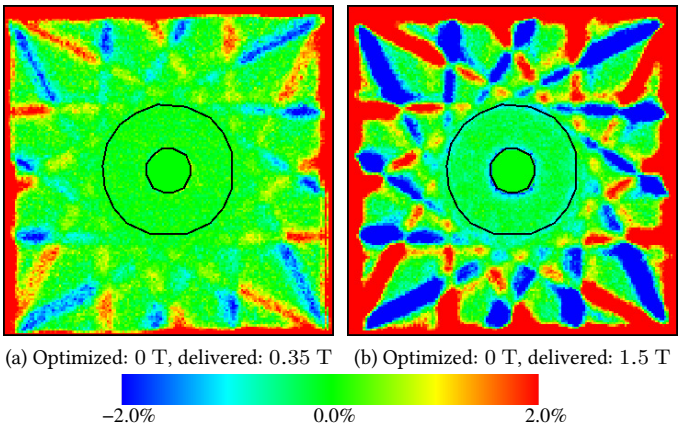

(a) Optimized: 0 T, delivered: 0.35 T (b) Optimized: 0 T, delivered: 1.5 T

Figure 6.4: Interfraction random moving air cavity results.

The results of the intrafraction random moving air cavity, optimized at the 1.5 T or at 0 T and both delivered at 1.5 T, are depicted in Figure 6.5. At the top row the beams of the plan were delivered in a sequential manner, the middle row using opposing beams and the bottom row using three equidistant beams simultaneously.

For the plans optimized at 1.5 T, the influence of the magnetic field on the target dose becomes slightly less when using opposing or three equidistant beams delivery and/or by having a 0.35 T magnetic field instead of 1.5 T. Compared to the no air cavity and static air cavity experiment results, the magnetic field influence is slightly larger or comparable (see Table 6.1).

For the plans optimized at 0 T, the results are similar to the results of 0 T optimized plans shown in Figure 6.3: a star shaped pattern with a slight dose decrease around the air cavity. When delivering at 0.35 T we did not observe this decrease around the air cavity. The target dose differences in terms of standard deviation is better for both field strengths compared to the cases where the optimization and the delivery magnetic field strength was in sync, as shown in the bottom part of Table 6.1. However, the mean of the 1.5 T cases drops due to the lower dose around the air cavity. Note that also the ERE at the boundary of the phantom remains, since this air-tissue interface is not in the crossfire of the beams.

6.3.3 Shifting air cavity experiments

The main interfraction shifting air cavities results are depicted in Figure 6.6. For the 0.35 T cases differences regarding target coverage are minimal, regardless if the 0 T or the 0.35 T optimized plan was used. For the 1.5 T case there was a significant difference: when using the 1.5 T optimized plan, extra dose was delivered just above the air cavity, with a peak value of 3.3 %. When the 0 T plan was used, the overdosage disappears and the low dose rim around the air cavity appears again.

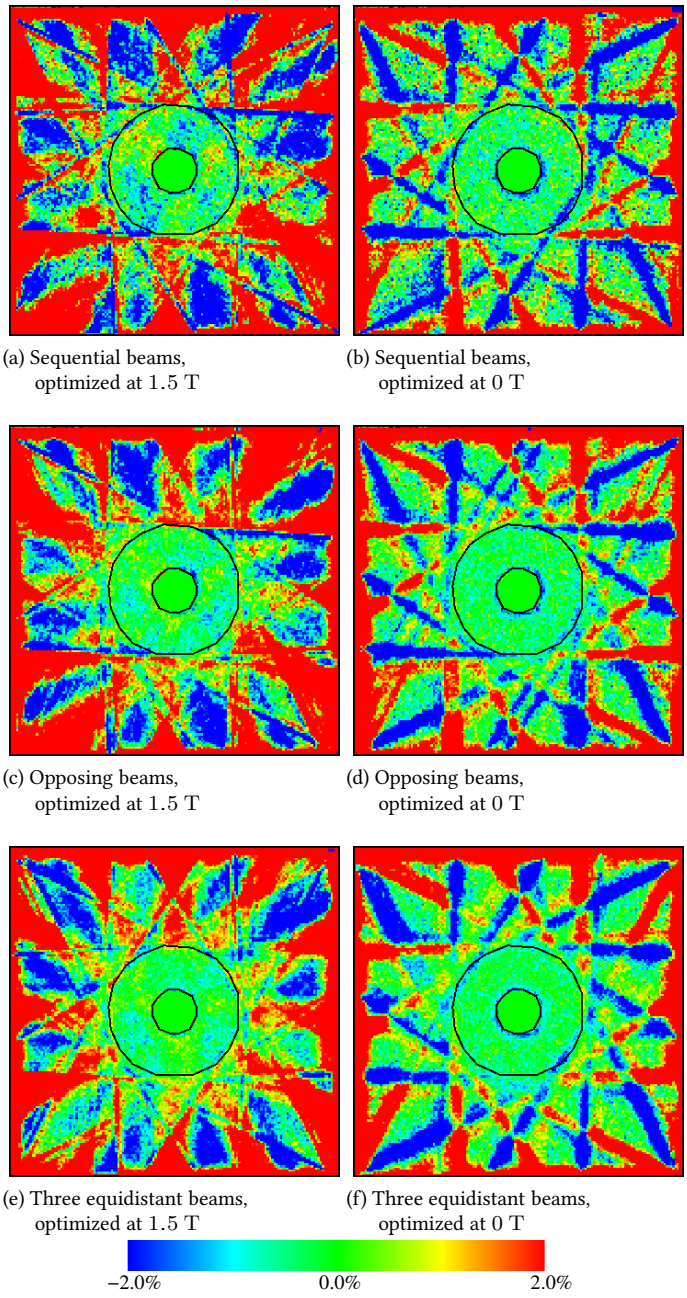

(a) Sequential beams, optimized at 1.5 T

(b) Sequential beams, optimized at 0 T

(c) Opposing beams, optimized at 1.5 T

(d) Opposing beams, optimized at 0 T

(e) Three equidistant beams, optimized at 1.5 T

(f) Three equidistant beams, optimized at 0 T

Figure 6.5: Intrafraction random moving air cavity results, all delivered at 1.5 T, using 1.5 T and 0 T optimized plans.

Case	Mean (%)	SD
No air cavity, 0.35 T	0.00	0.53
No air cavity, 1.5 T	0.01	0.53
Static air cavity, 0.35 T	0.00	0.52
Static air cavity, 1.5 T	0.01	0.53
Interfr, random pos, 0.35 T	0.02	0.30
Interfr, random pos, 1.5 T	0.01	0.29
Intrafr, random pos, sequential beams, 0.35 T	0.02	0.74
Intrafr, random pos, sequential beams, 1.5 T	0.00	0.86
Intrafr, random pos, opposing beams, 0.35 T	0.01	0.53
Intrafr, random pos, opposing beams, 1.5 T	0.01	0.60
Intrafr, random pos, 3 equidistant beams, 0.35 T	0.01	0.45
Intrafr, random pos, 3 equidistant beams, 1.5 T	0.01	0.50
Intrafr, optim 0T, random pos, sequential beams, 0.35 T	0.01	0.56
Intrafr, optim 0T, random pos, sequential beams, 1.5 T	0.27	0.67
Intrafr, optim 0T, random pos, opposing beams, 0.35 T	0.02	0.39
Intrafr, optim 0T, random pos, opposing beams, 1.5 T	0.31	0.47
Intrafr, optim 0T, random pos, 3 equidistant beams, 0.35 T	0.02	0.32
Intrafr, optim 0T, random pos, 3 equidistant beams, 1.5 T	0.31	0.42

Table 6.1: Mean and standard deviations of dose differences of all target voxels.

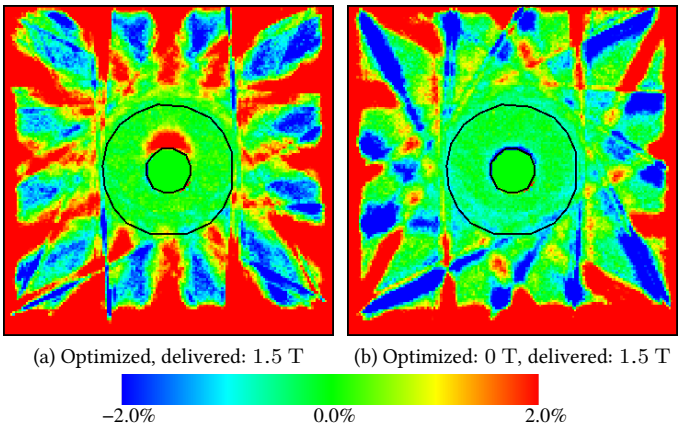

(a) Optimized, delivered: 1.5 T (b) Optimized: 0 T, delivered: 1.5 T

Figure 6.6: Interfraction shifting air cavity results.

The same behavior is seen when shifting the air cavity in a intrafraction way (see Figure 6.7): for the 1.5 T optimized plans, delivered at 1.5 T the overdosage appears regardless of the delivery strategy used. All peak values are below 3.4 %. For the 0.35 T cases this hotspot is not observed. When using the 0 T plans, the low dose around the air cavity replaced the overdosed area. Note that the high and low dose striping on the edges of the target are due to the rigid dose remapping to the reference position: initial small dose differences due to optimization and dose distribution shifts caused by the magnetic field are exaggerated because of repeated shifted addition of these differences.

6.3.4 Appearing and disappearing air cavity experiments

Figure 6.8 shows the results for plans optimized without an air cavity present, delivered at the same magnetic field strength, using the MRL and ViewRay^{TM} beam arrangements, i.e. representing the physical machines. During fraction delivery, the air cavity was present half of the time. The ERE is clearly visible around the air cavity, but it is reduced when using the opposing or the three equidistant beam strategy. Changing to the 0 T plan does not decrease the impact of ERE on the dose distribution.

When comparing the 0.35 T and the 1.5 T results of the opposing beams strategy, we observed that the ERE appears more pronounced in the 0.35 T case than in the 1.5 T case.

The experiments, as described in the previous paragraph, were repeated but this time the optimized plans contained the air cavity. This setup mimics the disappearing air cavity scenario. The results regarding the ERE are virtually the same for these cases, but are not presented here.

The graphs of Figure 6.9 show the maximum difference values for all beam delivery strategies, 0.35 T and 1.5 T magnetic field influences and the effect of 0 T plan optimization for both the appearing and disappearing air cavity in the target volume (excluding the air cavity). In general, appearing or disappearing air cavities result in the same dose distributions and the more simultaneous beams used during delivery, the more ERE compensation around the air cavity is noticeable. Except for the sequential beam delivery, the 0.35 T and the 1.5 T results are comparable. Furthermore, optimizing at 0 T while delivering the plan with a magnetic field does not lower the influence of the ERE on the dose distribution. Note that there is more underdosage than overdosage for all graph points.

6.4 Discussion

As described by (Raaijmakers *et al.*, 2007a) and also shown in section 6.3.1 of this paper, the influence of the magnetic field and particularly the ERE can be compensated by using an opposing beam geometry when having a static anatomy. IMRT only adds little extra modulation. Plans optimized at 0 T and delivered at for instance at 1.5 T come close to the plans optimized at 1.5 T, although a small underdosage around the air cavity becomes visible. When an air cavity is moving randomly around the reference position this behavior does not change, both for inter- and intrafraction movements.

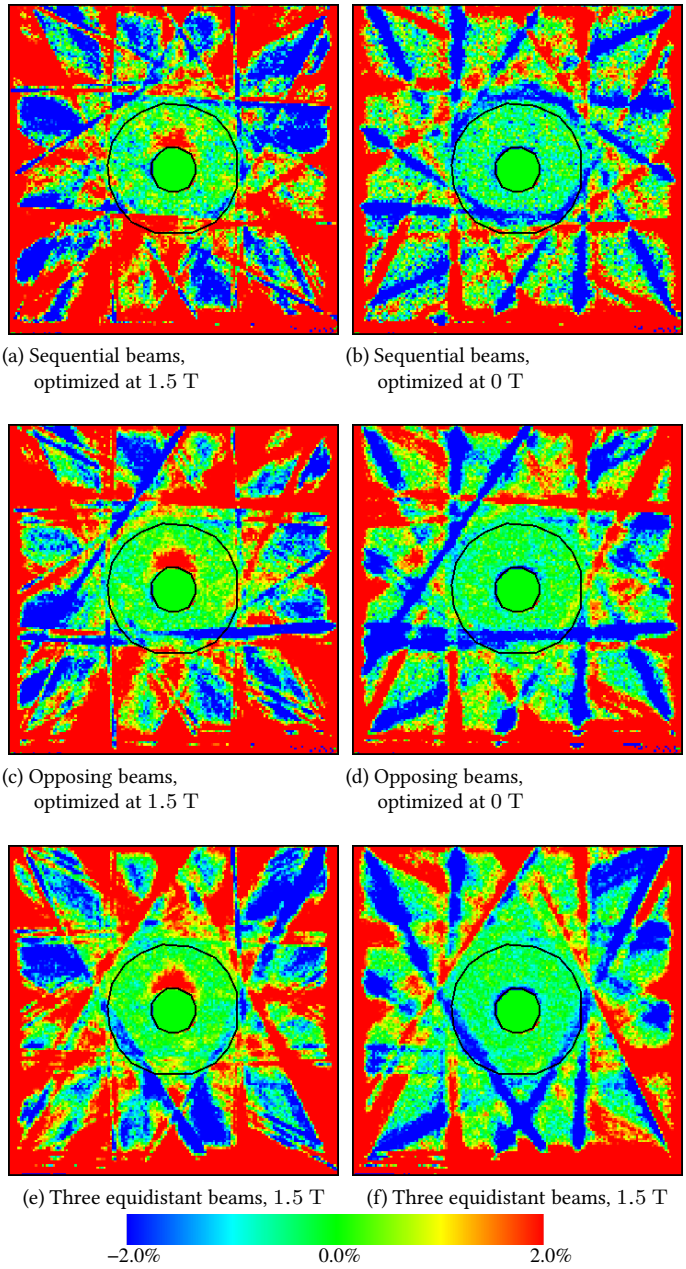

(a) Sequential beams, optimized at 1.5 T

(b) Sequential beams, optimized at 0 T

(c) Opposing beams, optimized at 1.5 T

(d) Opposing beams, optimized at 0 T

(e) Three equidistant beams, 1.5 T

(f) Three equidistant beams, 1.5 T

Figure 6.7: Intrafraction shifting air cavity results, all delivered at 1.5 T, using 1.5 T and 0 T optimized plans.

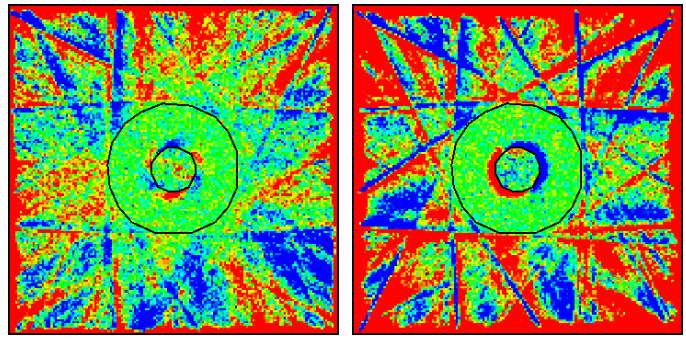

(a) Three equidistant beams, optimized and delivered at 0.35 T

(b) Sequential beams, optimized and delivered at 1.5 T

Figure 6.8: Appearing air cavity, results for the ViewRay^{TM} and MRL machine configurations.

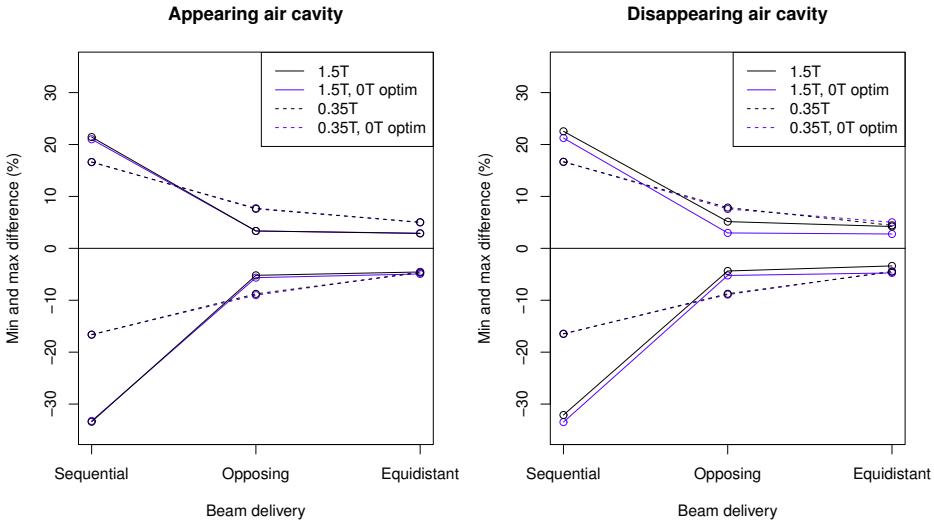

Figure 6.9: Minimum and maximum deviations for the sequential, opposing and three equidistant beams delivery when an air cavity is appearing or disappearing at 0.35 T and 1.5 T. Results are given for the 0 T optimized plans and the same field strength optimized plans. Note the graphs of the 0.35 T cases coincide.

When optimizing at 1.5 T, some dose is given to compensate for this effect. However, when a baseline shift occurs this extra dose ends up in the tissue resulting in a hotspot as seen in Figures 6.6 and 6.7. This effect does not occur when the plan was optimized at 0 T, since this plan did not incorporated ERE compensation.

Given these results, the 0 T optimized plans can be used to minimize the magnetic field effects (especially the ERE) around non-stationary spherical air cavities. The results can even be improved by using only the shifted, asymmetric penumbra effect caused by the magnetic field during dose calculation, while disregarding the ERE. This opens up the possibility to use a kernel-based dose calculation algorithms (Pfaffenberger, 2013) instead of a full Monte Carlo calculation, for those situations with air cavities inside the radiation field crossfire. This can be beneficial for online plan re-optimization due to shorter computational times.

Another possible strategy which does not include disregarding the ERE is 4D planning: if the movement of an air cavity can be modeled, then it can be included in the treatment optimization in order to minimize the ERE. In other words, this will involve an ERE initiated robust planning regime.

Although the ERE is compensated for when the air cavity is in or near the target (and therefore typically in the crossfire of all beams), the ERE is still an important factor when the air cavity is outside the crossfire of the treatment beams, as seen at the boundary of the phantom in all figures. Air cavities which are only irradiated from one angle are subjected to maximum ERE, and this is particularly true for the skin-air interfaces. On the other hand, those area's are usually in the low dose regions, are typically not used during dose optimization and the effect on the DVH is limited as shown in section 6.2.2. A single post-optimization or even post-fraction Monte Carlo dose calculation should suffice in order to review the ERE in most clinical cases.

When during irradiation an air cavity appears or disappears, changing to a 0 T plan does not decrease the effect of the ERE. Using two or three simultaneous beams can have a positive effect on the ERE influence, but due to the unpredictable behavior of such air cavities, the residual ERE may still add up to less or more dose than expected. We observed this positive and negative interference of residual ERE is especially when comparing the 0.35 T and the 1.5 T results of the opposing beams strategy: in these cases the 0.35 T ones has more pronounced over- and underdosage at the air cavity border than the 1.5 T case, which contradicts at first sight with the other results of this paper. Furthermore, these simultaneous beam delivery strategies do not have a significant effect on the other intrafraction cases investigated. Appearing or disappearing air is dosimetric troublesome, but since image guidance is the key element of the MRL, events such as passing gas should be detected and handled correctly by means of a gated delivery or plan re-optimization based on the current patient anatomy.

Instead of having to irradiate from multiple angles simultaneously, the effect of a non-stationary spherical air cavity can be decreased by using a fast form of arc therapy. With the MRL it will be possible to continuously irradiate the patient while the gantry is rotating at approximately 6 RPM. This means that the opposing beam configuration

will occur every 5 seconds for each beam angle, limiting the effects of ERE, even if an air cavity shifts or appears/disappears. The full extent of using fast arc therapy for compensating ERE will be investigated in future using more clinically relavent targets that contain air-cavities, and are in close proximity to organs at risk.

As expected the influence of a 0.35 T magnetic field on a moving air cavity is less pronounced than the influence of the 1.5 T. Especially for the shifting air cavity experiments, the 0.35 T optimized dose distributions are closer to the 0 T optimized ones. Since the optimized 0 T and the 0.35 T plans do not differ as much, the gain when using the 0 T plans instead of the 0.35 T plans is less compared to the 1.5 T cases.

6.5 Conclusions

While this study only investigated ERE compensation for the moving spherical cavities that are centrally located in the target without considering the organs at risk, the results form strong bases for future, clinically relevant investigations. Opposing beam configurations can be used for compensating the dose influence (especially ERE) of a transverse magnetic field around non-stationary spherical air cavities within the target area. IMRT further aids in getting the required dose uniformity. When delivering dose at 0.35 T, IMRT plans optimized at 0 T and 0.35 T perform equally well regarding ERE compensation. Within a 1.5 T environment, the 1.5 T optimized plans perform only slightly better for the static and random intra- and interfraction air cavity movement cases than the 0 T optimized plans and are comparable to plans optimized and delivered at 0 T. For non-stationary spherical air cavities with a baseline shift (intra- and interfraction) the 0 T optimized plans perform better. While these observations open up the possibility to use a kernel-based dose calculation algorithms (Pfaffenberger, 2013) instead of a full Monte Carlo calculation (thus disregarding the ERE), great care must be taken in case the air cavities are not fully covered by the beam cross fire. For intrafraction appearing or disappearing air cavities, gating or plan re-optimization should be used.

7

Virtual couch shift (VCS): accounting for patient translation and rotation by online IMRT re-optimization

This chapter is based on:
Bol G.H., Lagendijk J.J.W. and Raaymakers B.W. 2013 Virtual couch shift (VCS): accounting for patient translation and rotation by online IMRT re-optimization *Physics in Medicine and Biology* **58** 2989–3000

Abstract

When delivering conventional intensity modulated radiotherapy (IMRT), discrepancies between the pre-treatment CT/MRI/PET based patient geometry and the daily patient geometry are minimized by performing couch translations and/or small rotations. However, full compensation of especially rotations is usually not possible. In this paper, we introduce an online "virtual couch shift (VCS)": we translate and/or rotate the pre-treatment dose distribution to compensate for the changes in patient anatomy and generate a new plan which delivers the transformed dose distribution automatically. We show for a phantom and a cervical cancer patient case that VCS accounts for both translations and large rotations equally well in terms of DVH results and $2\%/2\ \mathrm{mm}$ γ analyses and when the various aspects of the clinical workflow can be implemented successfully, VCS can potentially outperform physical couch translations and/or rotations. This work is performed in the context of our hybrid $1.5\ \mathrm{T}$ MRI linear accelerator, which can provide translations and rotations but also deformations of the anatomy. The VCS is the first step towards compensating all of these anatomical changes by online re-optimization of the IMRT dose distribution.

7.1 Introduction

Intensity modulated radiotherapy (IMRT) can give a highly conformal dose distribution to the tumor tissue, while sparing the surrounding organs at risk (OAR) as much as possible. In conventional radiotherapy, the IMRT plan is optimized using inverse optimization before the treatment of the patient is started. The target volumes and OAR are defined based on a pre-treatment CT, possibly combined with other imaging modalities such as MRI or PET.

After treatment planning, the patient is treated according to calculated beam setup for up to 35 fractions. To minimize discrepancies between the pre-treatment CT/MRI/PET based patient geometry and the daily patient geometry, strict target alignment and patient positioning techniques have been developed to ensure adequate target coverage and avoidance of OAR. This is for instance accomplished by monitoring the daily motion of the patient geometry using on MV/kV imaging, cone-beam CT and in the future by MRI. If a correction is needed, the patient is brought back to the pre-treatment state as close as possible by using a couch translation and/or small rotation.

Conventionally, three-degree-of-freedom couches can only compensate translations of the patient anatomy during treatment. If the patient displacement has rotational components, compensation is not possible, due to couch limitations. The six-degree-of-freedom couches (such as the HexaPOD robotic couch (Elekta AB, Stockholm, Sweden)) can compensate for small, isocentric rotations up to ± 3 degrees in all principle directions (Meyer *et al.*, 2007). Large or off-isocenter rotations can not be corrected, although they do occur in clinical practice (Ahmad *et al.*, 2012; Lips *et al.*, 2009; Van der Heide *et al.*, 2007). Deformation of targets and OAR can not be compensated by any couch type.

Here, we introduce a method which accounts for patient translations and rotations without changing the position of the couch. Instead, a 'virtual couch shift (VCS)' is performed: we translate and rotate the pre-treatment dose distribution to compensate for the changes in patient anatomy and generate a new plan which delivers the translated and/or rotated dose distribution automatically. Essentially, VCS produces a clinically similar dose distribution at a new position, so maintaining all patient specific pre-treatment dose considerations.

Instead of performing a full plan re-optimization, one could also translate and/or rotate the pre-treatment apertures to (partially) compensate for a changed patient anatomy (Rijkhorst *et al.*, 2009; Mohan *et al.*, 2005). This strategy is hampered by the same type of constraints as seen by physical couch based strategies. The effectiveness will decrease even more if instead of using a flat beam profile, a flattening filter free (FFF) beam profile is used. For instance, an aperture shift will result in very different dose deposition than was originally intended.

The main advantage of VCS is that the correction of rotations is not hampered by couch limitations. Furthermore, VCS is important for the development of the MRI linear accelerator (MRL). The MRL combines an Elekta 6 MV linear accelerator system with a Philips 1.5 T MRI scanner (Lagendijk *et al.*, 2002; Raaymakers *et al.*, 2009) and is built for online, soft-tissue based position verification and treatment monitoring for image guided radiotherapy. Since the MRL does not allow table shifts due to the limited space in the bore of the MRI, VCS can be used to compensate for the daily patient position uncertainty. But more importantly, VCS is the first step towards a full online plan re-optimization paradigm (which is the ultimate goal of the MRL), resulting in an optimal dose delivery, which takes into account the interfraction patient anatomy translation, rotation and deformation as detected on the MRI images.

In this paper we will show that, within the MRL framework (with its particulars due to the presence of the 1.5 T magnetic field (Raaijmakers *et al.*, 2005b, 2007b)), patient translations can be compensated by VCS and we can also correct for large, off-center rotations with the same accuracy. We use a challenging phantom, with straight edges, a concave target shape and an air cavity inside and for which the plan has sharp dose gradients to validate our method. The method is also applied to a cervical cancer patient case. The differences between the pre-treatment plan and the generated plans are evaluated by DVH comparison and, since the aim of VCS is to generate the same dose distribution at a different location, we also present the results of γ analyses (Low *et al.*, 1998).

7.2 Materials and Methods

7.2.1 Anatomy definitions

The phantom used is a horseshoe like target area with an OAR and an air cavity inside (see Figure 7.1a). The basis of the phantom was formed by a $40 \times 20 \times 30$ cm^3 water phantom. The target is created by removing a block of $4.4 \times 4.2 \times 6.0$ cm^3 from a larger block of $8.4 \times 6.2 \times 6.0$ cm^3. At the center of the cavity of the horseshoe, a cylinder of air with a diameter of 3.2 cm and a length of 10.0 cm was placed which was surrounded by a cylindrical OAR with a diameter of 4 cm and a length of 6 cm.

Due to the sharp edges and concave shape of the target area, combined with the inner OAR, this case is challenging to perform a VCS on. Steep dose gradients have to be regenerated automatically with different translations and rotations, without changing the number of beams and/or gantry angles. Moreover, the air-tissue interface yield steep dose gradients due to the electron return effect (Raaijmakers *et al.*, 2005b, 2007b) induced by the magnetic field.

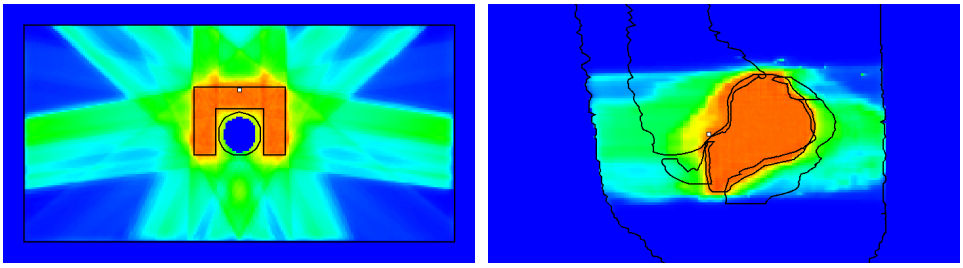

(a) Phantom case (b) Cervix case

Figure 7.1: Pre-treatment fluence-based dose distributions of the phantom and the cervix case. The white squares indicate the positions of the isocenters.

The patient anatomy used was a cervical cancer patient (see Figure 7.1b). The clinical CT and delineations were used to define the planning target volume (PTV) and OARs. The OARs were the rectum, sigmoid, bladder and the bowel. Note that for both the

phantom and the cervical cancer patient case the isocenter was placed off-center the target volume.

7.2.2 IMRT optimization and sequencing

The inverse treatment planning system (TPS) we used is described in Bol *et al.* (2012). It combines a GPU based Monte-Carlo dose calculation engine (Hissoiny *et al.*, 2011a,b) for online beamlet generation (GPUMCD) and a fast inverse dose optimization algorithm (FIDO) (Goldman *et al.*, 2005, 2009). It is capable of generating tightly conformal fluence-based IMRT plans, while incorporating the electron return effect caused by the presence of the 1.5 T magnetic field. Furthermore, the system is fast enough for online IMRT planning: for the phantom and the cervix case presented here, the beamlet generation and IMRT optimization takes roughly 1 minute and 2.5 minutes respectively, when using Nvidia® GeForce GTX 480 graphics cards for beamlet generation and a quad core 64-bit Intel® i5-2400 CPU for the IMRT optimization step. For details regarding the beamlet generation, changes made to the FIDO algorithm and the exact timings of TPS we refer to Bol *et al.* (2012).

For this paper we complemented the TPS by adding step-and-shoot MLC sequencing. Sequencing decomposes the optimal fluence map, calculated by the inverse fluence optimization, for each beam into deliverable MLC field shapes, called apertures. In this case, the apertures are generated using the Continuous Intensity Map Optimization (CIMO) algorithm as described by Cao *et al.* (2006). The number of apertures was fixed to 15 per beam. The used MLC definition is similar to the one currently installed in the MRL: it has 80 leaf pairs, having a 7 mm leaf width at the isocenter. No minimal leaf gap is defined and interdigitation of neighboring leafs is allowed. Sequencing takes on average an extra 30 seconds of CPU time, keeping total computation time for a single plan fast enough for online usage.

7.2.3 Pre-treatment planning

To establish the pre-treatment dose distribution, the phantom and the cervix case were first manually planned with beamlets calculated in the presence of a magnetic field of 1.5 T. Seven fixed gantry angles of 0, 50, 100, 155, 205, 260 and 310 degrees were used. The phantom case had a target prescribed dose of 75 Gy, whereas the target prescribed dose of the cervix case was 45 Gy.

The main manual planning criterion was that 99% of the target volume received at least 95% of the prescribed dose (D_{99}), while creating as steep as possible dose gradients outside the targets to ensure maximum OAR sparing. In order to get steep dose gradients around the targets, the importance weights of the OARs were elevated until the D_{99} criterion was just satisfied.

After the optimal beamlets weights were determined for each case, sequencing was performed as described in Section 7.2.2. The pre-treatment DVHs after fluence optimization and after sequencing are presented as part of Figure 7.2.

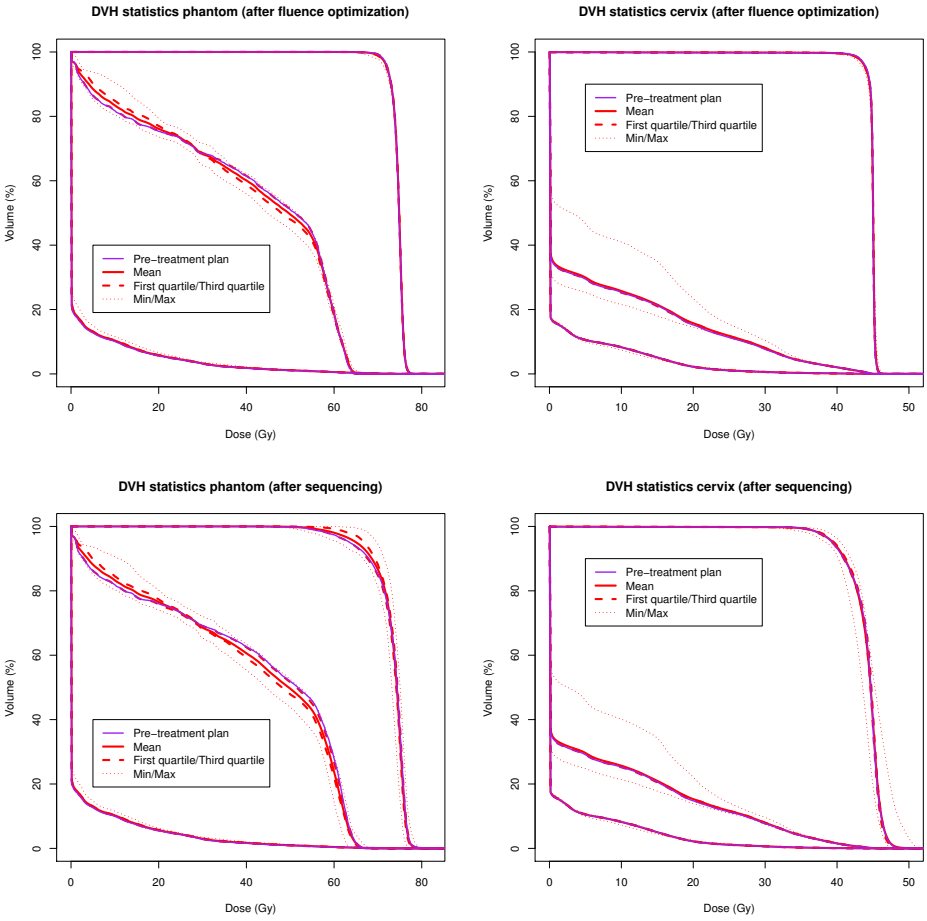

Figure 7.2: Summary of the DVH statistics from the phantom and the cervix case, after fluence optimization and sequencing. The graphs show the pre-treatment planned DVH and the mean, first and third quartile, the minimal and the maximum DVHs, after applying the 48 translations and 42 rotations, for the target, the total OAR volume and the body.

7.2.4 VCS experiments and comparison

All VCS experiments started by translating the complete or rotating the internal phantom and patient anatomy. For each of these translations and rotations, the pre-treatment optimized fluence distribution was also translated or rotated with the same amount in order to get the goal towards VCS is optimizing. The translations were defined along the x-, y-, and z-axis: (+x, 0, 0), (-x, 0, 0),(0, +y, 0), (0, -y, 0),(0, 0, +z) and (0, 0, -z), with different translation offsets: $1, 2, 3, 5, 8, 13, 21$ and $34\,\mathrm{mm}$. The rotations were defined along the same axes and had values of $1, 2, 3, 5, 8, 13$ and $21\,\mathrm{degrees}$ around the isocenter. This means that for each case, a total of 48 translations and 42 rotations were applied.

After a transformation was applied, beamlets were calculated for the new geometry. These beamlets were automatically optimized by setting the prescribed dose (which will be fed into FIDO) for each target voxel or high-dose OAR voxel to the same value as the corresponding transformed pre-treatment fluence value. All remaining (body) voxels were set to zero dose with a low importance weight of 1, whereas the voxels with a prescribed dose had a importance weight of 300. This value was determined empirically, but the exact value proves to be not critical for the optimization result. All OAR voxels of the phantom case were considered high-dose voxels, but with the cervix case only the voxels receiving $\geq 30\,\mathrm{Gy}$ were marked as high-dose OAR voxels, since these are considered clinically relevant.

The resulting prescribed dose and importance weights matrix are directly used as input for the FIDO optimization routine (Figure 7.3 shows an example of the FIDO input for the cervix case, which was rotated 13 degrees around the x-axis). It calculates the new optimal beamlets weights, resulting in a new optimal fluence distribution, followed by the sequencing step as described in Section 7.2.2, which gives a deliverable dose distribution. Note that the desired fluence distribution is typically "non-physical", due to the applied transformations, but FIDO will calculate the nearest physical solution possible. This will be discussed further in Section 7.4.

Both the resulting fluence and dose distributions are compared with the transformed pre-treatment results by using DVHs and by using the $2\%/2\,\mathrm{mm}$ γ criterion. The pre-treatment optimized fluence distributions were used as the reference dataset for all γ analyses. Prior to the γ analyses, the VCS results were first translated or rotated back to the original pre-treatment position in order to make a valid comparison possible.

7.3 Results

Figure 7.2 summarizes the DVH results after all translations and rotations were compensated by an automatically generated VCS. The graphs show the pre-treatment DVH and the mean, first quartile and third quartile, and the minimum and maximum DVH values extracted from all individual DVHs, calculated after each anatomy transformation. This results in a "boxplotted" DVH overview. The top row show the results after fluence optimization, the bottom row shows the results after sequencing. Note that the mean DVH of the sequenced phantom plans performed better in terms of target coverage and

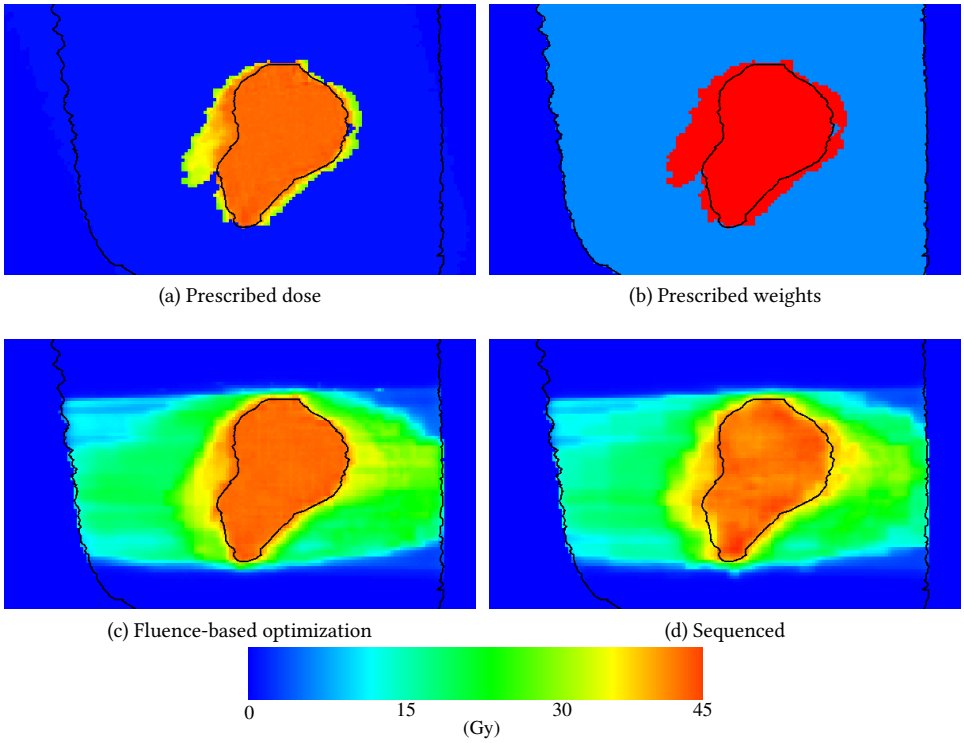

Figure 7.3: The images on the top row show the prescribed dose and weights used for FIDO optimization for the cervix case where a x-rotation has been applied of 13 degrees. All target voxels are included into the prescription, plus the OAR voxels receiving ≥ 30 Gy. The remaining body voxels are marked as OAR. The target voxels have an importance weight of 300, all other voxels an importance weight of 1. The images on the bottom row show the results after fluence optimization and sequencing.

OAR sparing than the pre-treatment plan. Furthermore, the effect of the used 30 Gy threshold on the cervical high-risk OAR voxels is clearly visible: from this point on, the difference between the minimum and the maximum DVH decreases significantly.

All fluence based plans generated by VCS obtain virtually identical target coverage and OAR sparing when comparing them to the pre-treatment plan. The DVHs of the sequenced plans are less steep due to the discretization errors introduced due to generating a distinct number of apertures with a finite leaf width. Other than that, the sequenced plans produced by VCS result in similar DVHs when comparing them to the pre-treatment sequenced plan.

Figure 7.4 shows the effect of applying only translations, only rotations and applying both on the mean DVH. Since all DVHs virtually coincide, VCS is as effective for compensating for (large) rotations as for translations.

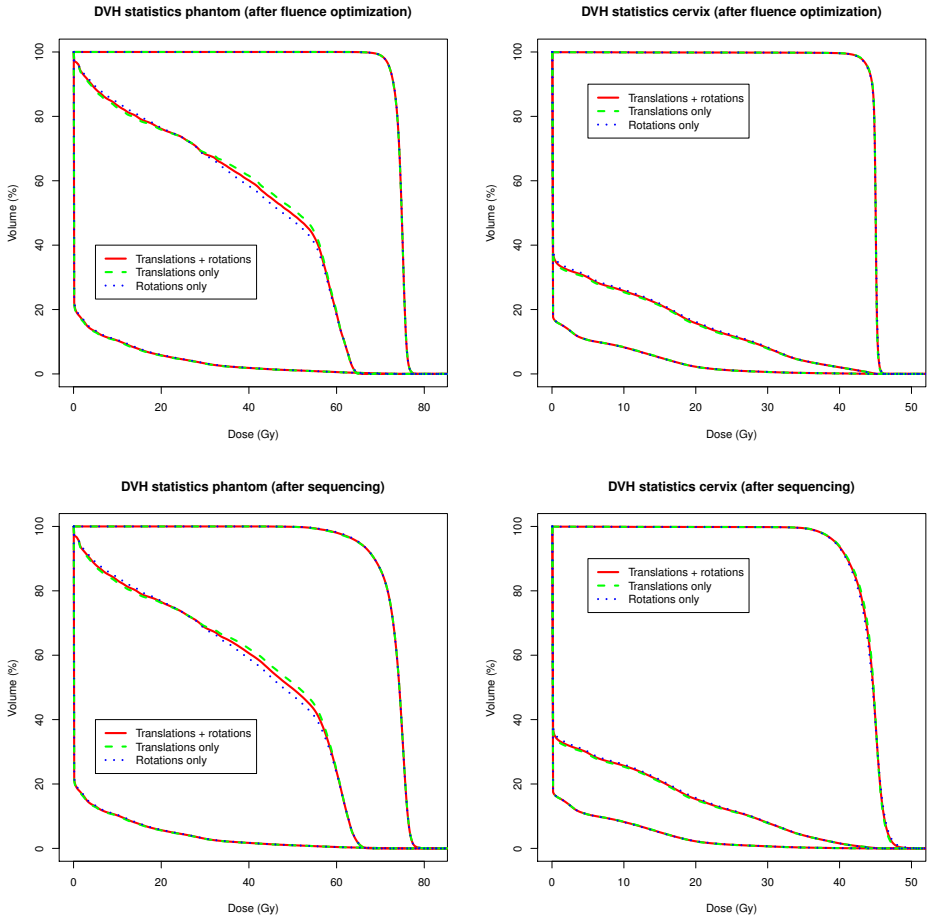

Figure 7.4: Summary of the DVH statistics from the phantom and the cervix case, after fluence optimization and sequencing. The graphs show the mean DVHs after the translations and rotations and the graphs depicting the mean DVHs after only the translations and rotations, for the target, the total OAR volume and the body.

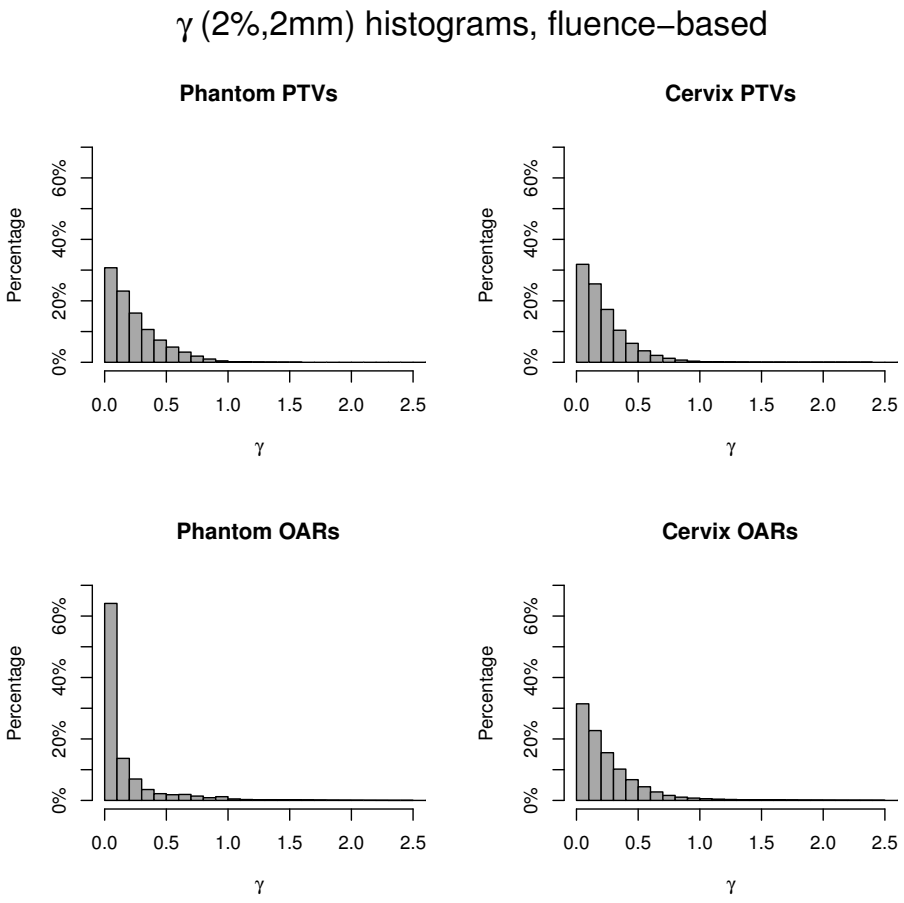

Figure 7.5: Histograms of γ values for PTV and high-dose OARs voxels of the phantom and the cervix case after fluence optimization. The histograms accumulate the results of all generated plans after applying the translations and rotations.

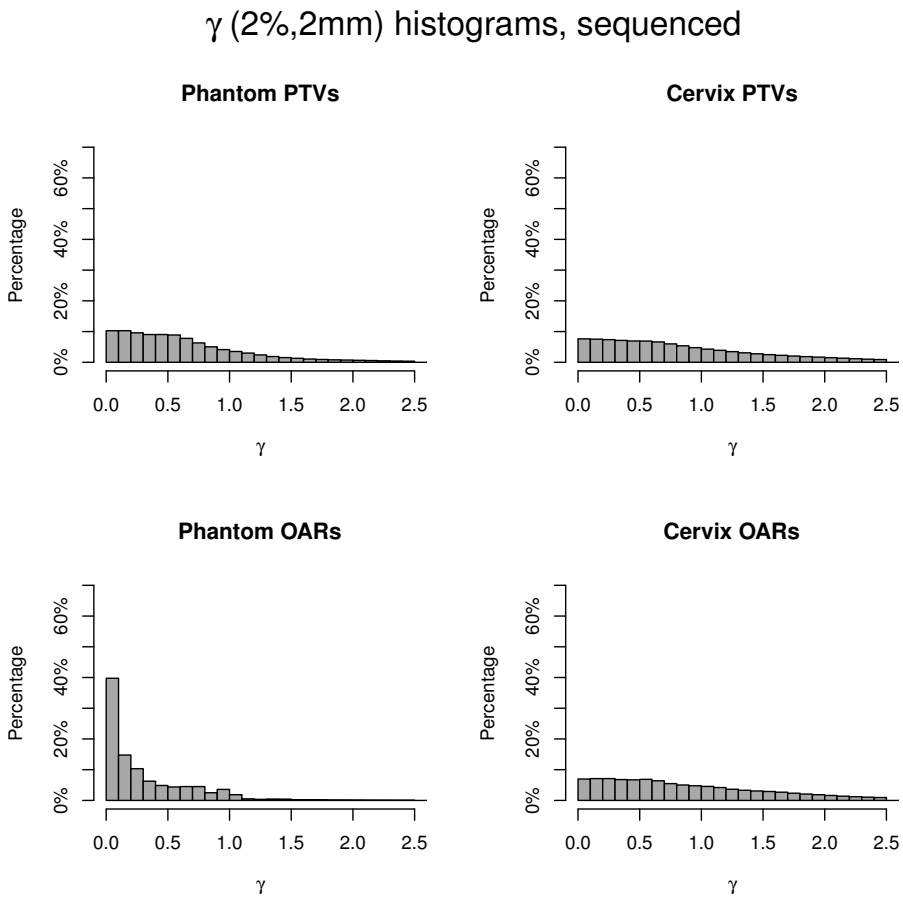

Figure 7.6: Histograms of γ values for PTV and high-dose OARs voxels of the phantom and the cervix case after sequencing. The histograms accumulate the results of all generated plans after applying the translations and rotations.

Table 7.1 shows the percentages of voxels of all re-generated plans, having a γ value ≤ 1. For all fluenced-based cases, well over 96% of the target and high-dose OAR voxels satisfy the $2\%/2\ \mathrm{mm}$ γ criterion. Figure 7.5 and 7.6 show the general histograms of the γ values for all generated fluence-based and sequenced plans. The shapes of the γ histograms with respect to rotations and translations (not presented here) are very similar to the general histograms. Figure 7.7 shows the relation between the magnitude of the applied translations and rotations and the percentage of PTV and high-dose OAR voxels fulfulling the γ criterion. All results show that the fluence-based plans can reproduce the original plan very accurately and the influence of the magnitude of the translations and rotations is very limited. As expected, the sequenced plans show deteriorated results compared to the fluence based plans, but were also not influenced by the applied translations and rotations. This confirms that VCS can compensate for both transformations, in terms of the γ criterion, equally well, as also seen in Figure 7.4.

Case	*PTV fluence-based*	*PTV sequenced*	*High dose OAR fluence-based*	*High dose OAR sequenced*
Phantom	99.7%	78.4%	97.7%	94.5%
Cervix	99.6%	62.4%	96.9%	59.1%

Table 7.1: Table containing the percentage of all PTV and OAR voxels after applying 48 translations and 42 rotations, which have a γ (2%,$2\ \mathrm{mm}$) ≤ 1.0. Percentages are given after optimization and after sequencing.

7.4 Discussion

Accounting for patient translation and rotation is possible using VCS. The DVHs differences between the automatically generated plans and the pre-treatment plans are very small. The γ analyses confirm this statement. There is no accuracy difference anymore between compensating for rotations and translations, as there is when performing physical couch shifts. Since new beamlets are generated for each VCS, our method also incorporates dose effects caused by for instance a changed body contour.

The FIDO algorithm proves to be very efficient in re-generating a pre-treatment dose distribution at a different location and/or with a different orientation within a new patient anatomy. The main reason for this is that FIDO by definition delivers the optimal solution when given a dose description and importance weight for each voxel and does that very quickly. The dose prescription is given by just applying the observed patient transformation to the pre-treatment dose distribution and setting some default important weights. In other words, FIDO performs very well in an online dose-painting-by-numbers strategy. This also means that we can use any TPS with their specific fluence-based optimization strategies to generate the pre-treatment plan, and use FIDO for the online translation and rotation correction re-optimization.

As described in Section 7.2.4, by translating or rotating the pre-treatment dose distributions, a “non-physical” dose prescription will occur, e.g. the gantry position does not fit the pre-treatment beam path anymore. In order to avoid large errors between the prescription and the feasible physical dose, special attention is needed for these ’beam

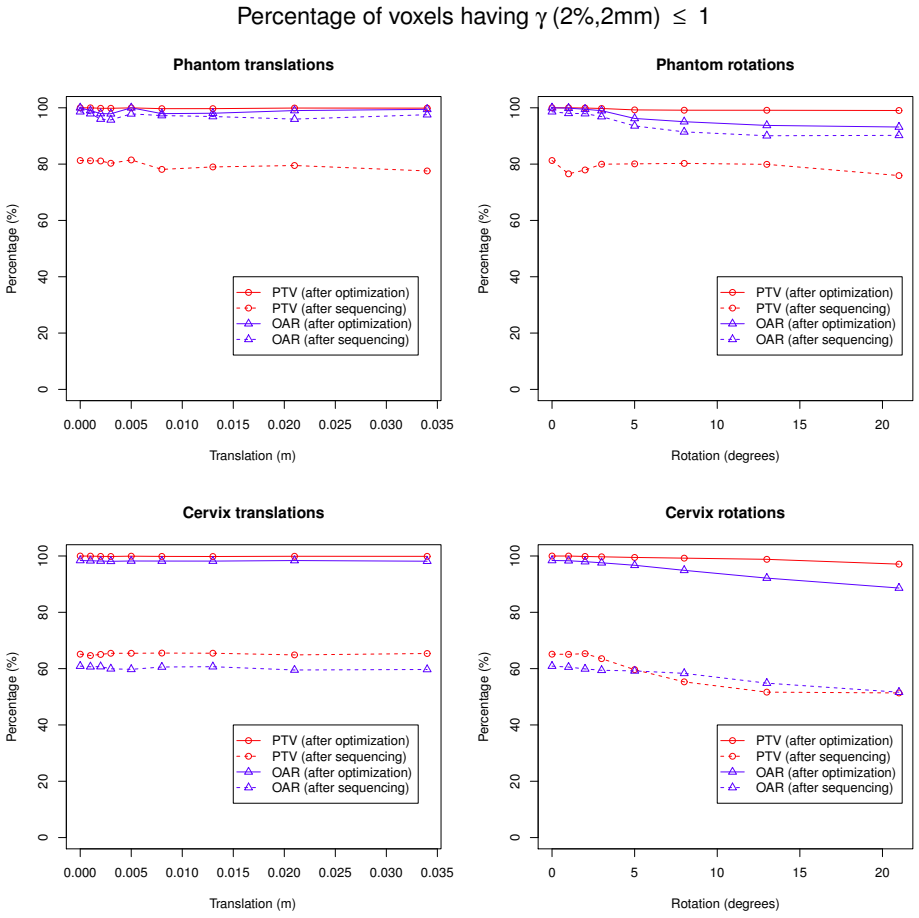

Figure 7.7: Graphs show the relation between the magnitude of the translation and rotation and the precentage of voxels fulfilling the 2%,2 mm γ criterion after beamlet optimization and after sequencing. The graph points with no translation or rotation present the pre-treatment optimization results.

entry' areas. These low dose areas typically occur far away from the target area. Compensating for these artifacts will deteriorate the target coverage, since the optimization will try to fulfill all voxel constraints. Therefore, only the high-dose (and clinically relevant) part of the pre-treatment dose distribution should be used in order to perform a proper VCS.

In this paper we start with optimizing the beamlets to get an ideal, fluence-based dose distribution, followed by a sequencing step. By doing this, VCS dose effects caused by fluence optimization errors and sequencing errors can be separated. The reproducibility of the fluence optimization is very good, large translations and rotations can be corrected without compromising plan quality. The vast majority of the sequenced plans of VCS are also very close to the pre-treatment sequenced plans, but it is a fact that converting an ideal plan into a deliverable plan is more susceptible for unfavorable anatomies. As mentioned in Section 7.3, Figure 7.2 shows that for the phantom case, the pre-treatment sequenced plan has such a disadvantageous geometry, leading to a lower target coverage and a high OAR exposure than the mean of the generated plans has in terms of DVHs. However, in a clinical setting is it unlikely that these unfavorable anatomy occur systematically.

A disadvantage of the two step optimization approach is that the sequencing step always deteriorates the initial plan, since it does not take into account the contraints on which the fluence optimization was based on. This means that with our current setup it will be difficult to match treatment plans optimized with for instance Direct Aperture Optimization (DAO) or Direct Machine Parameter Optimizion (DMPO). It is expected that when we integrate the FIDO algorithm with the sequencing routine, it will be feasible to regenerate these plans.

Clearly, VCS can also be used in a 0 T environment. Cone-beam CT (or even MV/kV imaging, combined with fiducial markers) can be used to obtain the daily target translations and rotations. Also a regular TPS can be used for the re-optimization of the treatment plan, as long as a prescribed dose per voxel can be entered and it is fast enough for online usage.

In order to use VCS clinically, a new workflow has to be put into place. It starts with capturing the patient displacement by for instance MRI images. Missing density information has to be handled, for example by registering a pre-treatment CT to the newly acquired MRI, using a pseudo CT derived from a specific MR scans (Johansson *et al.*, 2011; Berker *et al.*, 2012) or replace the MRI image data by a bulk electron density. As VCS considers only translations and rotations, fast rigid image registration of the current patient anatomy to the pre-treatment patient anatomy can be used for contour propagation. Than the treatment planning part starts as we described in this paper. Plan quality can be assessed manually, but preferable automatically based on DVH and γ parameters. When passing all plan constraints, the new plan can be delivered. We expect that the whole procedure can be executed within minutes.

For QA purposes, phantom measurements can be performed after treatment. However, we expect that after gaining experience with the online re-optimization in terms of

phantom studies and post-fraction QA measurements, the conclusion will be that VCS plans are safe to deliver. This expectation is based on the fact that we clinically do not measure IMRT plans for head-and-neck or prostate cases on a phantoms anymore.

We showed VCS in context of the ongoing MRI linear accelerator project. With this machine, not only translations or rotations, but also deformations can be detected. To account for deformations, one may deform the pre-treatment dose distribution and use this as input for the full re-optimization. This strategy has to be investigated further. The VCS framework can also be a foundation on which deformations can be compensated by re-optimizing a plan, not based on a fixed pre-treatment dose distribution, but based on clinical optimization constraints. This will result in a system which automatically generates inter- or even intrafraction optimal plans which take into account the current patient anatomy.

7.5 Conclusions

VCS can account for patient translations and rotations by online IMRT optimization, without the need of modifying the position or orientation of the treatment couch. Both the generated fluence-based as sequenced plans perform well compared to the pre-treatment plans. Within our MRI linear accelerator framework, VCS runs automatically and the DVHs and γ analyses show that both translations and large rotations can be compensated equally well. When the various aspects of the clinical workflow are implemented successfully, VCS can potentially outperform physical couch translations and/or rotations.

8

Summary

This thesis describes various radiotherapy treatment improvements which begins with optimizing the classical approach for patient position verification based on portal imaging, continues with adding MRI to the current radiotherapy scheme and ends with the first steps towards online MRI-guided radiotherapy.

In chapter 2 we present two offline methods for detecting the position of the bony anatomy automatically with portal imaging, even if every single portal image of each segment of an (IMRT) treatment beam contains insufficient matching information. Additional position verification fields will no longer be necessary, which speeds up the treatment and reduces the total dose to the patient. The first method, the stack matching method (SMM), stacks the portal image of each segment of a beam into a 3D volume and this volume is subsequently used during the matching phase. The second method, the averaged projection matching method (APMM), is a simplification of the first one, since the initially created volume is reduced again to a 2D artificial image, which speeds up the matching procedure considerably without significant loss of accuracy. Matching is based on normalized mutual information. We demonstrate our methods by comparing them to existing matching routines, such as matching based on the largest segment. Both phantom and patient experiments show that our methods produce results that are comparable with the results obtained from standard position verification methods. The matches are verified by means of visual inspection. Furthermore, we show that when an distinct area of 40 to 60 cm^2 of the EPID is exposed during one treatment beam, both SMM and APMM are able to deliver a good matching result.

Chapter 3 describes a tool which enhances the way tumors can be delineated by using multiple imaging modalities. This tool is especially useful when multiple MRI sequences are available as well as the standard planning CT. The system is based on two basic principles. Firstly, all individual image datasets are displayed in their original form (in their own coordinate system, with their own spatial resolution, voxel aspect ratio and slice orientation), and secondly, delineations can take place on all orthogonal views of each dataset and changes made to a delineation are visualized in all image sets, giving direct feedback to the delineator. The major difference between the described approach and other existing delineation tools is that instead of resampling the image sets, the delineations are transformed from one dataset to another. The transformation used for transferring the delineations is obtained by rigid normalized mutual information

registration. The crucial components and the benefits of the application are presented and discussed.

In chapter 4 we discuss the use of MRI-compatible fiducial gold markers. Conventional fiducial gold markers are poorly detectable on most MRI sequences. Therefore, markers always have to be detected on a separated CT, adding extra CT-MRI registration errors to the treatment preparation phase. We developed a marker which is visible on MRI and on EPID. A separate CT is no longer needed. The marker consists of a steel core with a diameter of 0.3 mm within a gold casing. The marker is 5.0 mm long and has a diameter of 1.0 mm. The steel core provides visibility on MRI and the gold casing on EPID. To investigate the interobserver variability, five experienced observers marked the positions of the markers on three MRI sequences: a bSSFP, T1- and T2-weighted sequence. These positions were also compared to the CT based marker positions. The bSSFP is best suited for delineating the prostate and detecting the developed markers. The interobserver variability is small (the mean absolute distances ranges from 0.16 mm to 0.30 mm). The differences between the positions detected via CT and via MRI were small, with the mean absolute differences ranging from 0.43 mm to 1.44 mm. Note that these differences also include registration errors. The gold marker with steel core can be detected on various MRI sequences, reducing the overall systematic treatment error.

The studies presented in chapter 5 and subsequent chapters are conceptually different to the previous studies, as the focus shifts from offline MRI-aided radiotherapy towards online MRI-guided radiotherapy, by introducing a planning system for the MRL. The MRL facilitates continuous patient anatomy updates regarding translations, rotations and deformations of targets and OAR. Accounting for this information demands high speed, online IMRT re-optimization. In this chapter, a fast IMRT optimization system is described which combines a GPU based Monte-Carlo dose calculation engine for online beamlet generation (GPUMCD) and a fast inverse dose optimization algorithm (FIDO). Tightly conformal IMRT plans are generated for four phantom cases and two clinical cases (cervix and kidney) in the presence of a 0 T and 1.5 T magnetic field. We show that for the presented cases the beamlets generation and optimization routines are fast enough for online IMRT planning. Furthermore, there is no influence of the magnetic field on plan quality and complexity, and equal optimization constraints at 0 T and 1.5 T lead to almost identical dose distributions.

As mentioned in the introduction of this thesis, one of the most significant effects of the transverse magnetic field on the dose distribution occur around air cavities: the electron return effect (ERE). For stationary, spherical air cavities which are centrally located in the phantom, the ERE can be compensated by using opposing beams configurations in combination with intensity-modulated radiotherapy (IMRT). In chapter 6 we investigate the effects of non-stationary spherical air cavities, centrally located within the target, on IMRT dose delivery in 0.35 T and 1.5 T transverse magnetic fields by using Monte Carlo simulations. We show that IMRT can be used for compensating ERE around those air cavities, except for air cavities that appear or disappear during delivery of a fraction. For these cases, gating or plan re-optimization should be used. We also considered the use of IMRT plans optimized at 0 T to be delivered in the presence

of 0.35 T and 1.5 T magnetic field. When delivering dose at 0.35 T, IMRT plans optimized at 0 T and 0.35 T perform equally well regarding ERE compensation. Within a 1.5 T environment, the 1.5 T optimized plans perform slightly better for the static and random intra- and interfraction cases of air cavity movement than the 0 T optimized plans. For non-stationary spherical air cavities with a baseline shift (intra- and interfraction) the 0 T optimized plans perform better. These observations show the intrinsic ERE compensation by equidistant and opposing beam configurations for spherical air cavities within the target area. IMRT gives some additional compensation, but only in the case of correct positioning of the air cavity according to the IMRT compensation. For air cavities appearing or disappearing during a fraction this correct positioning is absent and gating or plan re-optimization should be used.

Chapter 7 introduces a first step towards a real online MRI-guided treatment regime. When delivering conventional IMRT, discrepancies between the pre-treatment patient geometry as determined from CT, MRI and/or PET scans and the daily patient geometry are minimized by performing couch translations and/or small rotations. However, full compensation of rotations in particular is usually not possible. In this chapter, we introduce an online "virtual couch shift" (VCS): we translate and/or rotate the pre-treatment dose distribution to compensate for the changes in patient anatomy and generate a new plan which delivers the transformed dose distribution automatically. We show for a phantom and a cervical cancer patient case that VCS accounts for both translations and large rotations equally well according to DVH results and $2\%/2$ mm γ analyses and when the various aspects of the clinical workflow can be implemented successfully, VCS can potentially outperform physical couch translations and/or rotations. This work is performed in the context of our MRL, which can provide translations and rotations but also deformations of the anatomy. The VCS is the first step towards compensating all of these anatomical changes by online re-optimization of the IMRT dose distribution.

9

General discussion

9.1 Introduction

In this chapter we will discuss various topics which are subject to major changes when migrating from an offline MRI-aided treatment paradigm to an online MRI-guided treatment paradigm using the MRL. First we will describe how the general layout of a radiotherapy treatment will change and afterwards we will discuss specific details within the new regime such as image segmentation, treatment planning, and quality assurance (QA).

9.2 Changing the radiotherapy paradigm

In the introduction of this thesis we described the classical radiotherapy regime as a sequential, deterministic process which consists of three separate phases: the treatment preparation phase, the treatment planning phase and treatment delivery phase. With the development of the MRL, this regime has to be adapted in order to gain maximal improvement in terms of OAR sparing and/or escalating the dose to the target structures.

Figure 9.1 schematically shows how the new regime will look like. The most prominent difference is the fact that the classical sequential process is replaced by a continually repeating treatment cycle. The cycle consists of an image acquisition and VOI segmentation part, a treatment planning part and a treatment delivery part. With this setup ultimate adaptive radiotherapy that adapts to the continual changes of patient geometry can be achieved; the MRI, with its superior soft tissue contrast and fast imaging techniques, provides real time information about the position of the tumor and OAR, the online TPS adapts the current treatment plan to account for the observed translations, rotations and deformations and the adapted plan is directly delivered to the patient.

The timescale in which this cycle runs can differ. The most straightforward way of implementing this cycle is in an interfraction manner. At the beginning of a fraction, one or more volumetric MRI scans are acquired and segmented, and with this information a new treatment plan is calculated and then delivered. The VCS method described in this thesis fits nicely within this strategy.

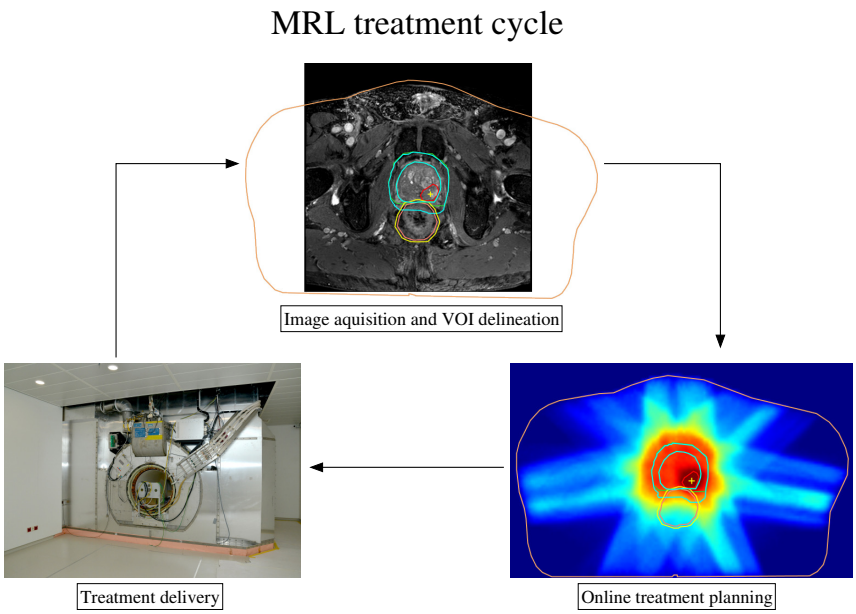

Figure 9.1: MRL treatment cycle

Intra-fractional changes are also addressed as the MRL treatment cycle is repeated multiple times within a fraction, for example before each delivered segment (in case the IMRT is delivered in a step-and-shoot fashion) or before each gantry rotation (in case of delivering IMRT using volumetric modulated arc therapy (VMAT)). Obviously this loop is the most demanding for all components of the cycle in terms of speed and QA; due to the time constraints the modules must be fast and reliable and should only require minimal human interaction.

Another challenge is how to correctly update the current patient model used for online treatment planning when there is not enough time to acquire a complete 3D MRI scan. One way of solving this is by deforming a full 3D MRI dataset acquired just before the start of the fraction based on changes registered by intelligently positioned one- or two-dimensional MRI images (Stemkens *et al.*, 2015). For safety, this method can be combined with a form of gating, which immediately stops the treatment delivery when large deviations, which invalidate the current patient model, are detected.

Instead of using gating as a safety measure, gating can also be used as a primary delivery mode within the MRL treatment cycle. This mode resides between the two timescales described before; for each fraction a new plan is generated for a favorable anatomy (i.e. the anatomy imaged during the gating window), but instead of adapting the treatment plan during delivery or delivering the pre-calculated plan in its entirety, the delivery is paused when the patient anatomy is considered unfavorable and continues when the favorable anatomy is restored. Tumor tracking, a method which dynamically moves the current segment shape along with the motion of the tumor, should also be possible

using the MRL. Before tumor tracking can be implemented, research questions regarding plan generation for tracked delivery and accurate translation of segment shapes in the presence of a non-flattened beam (used by the MRL) must be answered. Nevertheless, for both the gated and tracked IMRT delivery, MRI-guidance is the key ingredient for a successful radiation therapy treatment.

Although all of the above might suggest that a treatment simulation phase prior to the MRL cycle is not necessary anymore, the opposite is true. Not only should the anatomy of the patient be mapped during the simulation phase by 3D MRI images in order to determine the targets and OAR, but the optimal position of the one and two dimensional MRI images used to monitor the patient anatomy also needs to be determined. Furthermore, dynamic information such as tumor trajectories due to breathing should be investigated before the actual treatment starts, so that the information can be used as prior knowledge for choosing for example the best gating window or treatment planning strategy. Therefore, the simulation phase is needed to build a patient model which forms the basis of all patient anatomy and treatment adjustments during the MRL cycle.

The simulation phase is also important for determining the accuracy of the various MRI sequences for an individual patient, since MRI is prone to geometrical and intensity distortions (Bakker *et al.*, 1992; Moerland *et al.*, 1995). The registration and segmentation procedures can tested up to a point where even the MRI sequences are tailored to patient specific needs. Furthermore, in order to calculate accurate dose distributions, tissue density information is needed. Although these data can be obtained by segmenting the MRI into four tissue types (air, lung, soft tissue and fat) by using a combination of MRI sequences (Berker *et al.*, 2012) or via direct visualization of the bony structures using ultrashort TE sequences (Hsu *et al.*, 2013; Korhonen *et al.*, 2014), combining the MRI data with a corresponding CT is a valid solution for the most accurate means of obtaining the required Hounsfield data. The CT can also be used to extract structures such as the body contour, which is usually the structure most affected by the MRI distortions.

Finally, by simulating the upcoming fractions in terms of treatment planning, the impact of the ERE can be estimated. As shown in chapter 6, the critical effects do not occur in the high dose regions, i.e. in the crossfire of the beams, but mainly in the low dose areas which are typically covered by a single beam. Nevertheless, from a QA perspective it is good practice to detect initial plan setups which are too sensitive regarding possible ERE related problems before treatment instead of detecting them during treatment. When such a plan is identified, the impact of ERE can be reduced by adapting the base plan parameters.

The treatment cycle regime as described in this section can also be applied in current clinical practice, using a conventional linear accelerator along with the position verification tools mentioned in section 1.1.3. At our department we are investigating the use of VCS for hypofractionated prostate cancer treatment. This treatment gives high dose (72 Gy) to the whole prostate and an additional integrated boost up to 95 Gy to the primary lesions within the prostate in 5-7 fractions. Due to the high dose per fraction, it is not only necessary to compensate for prostate translations during treatment (as we

do for the current prostate treatment using 35 fractions), but also for rotations to avoid unacceptable rectal toxicity. Our goal is to automatically generate a new treatment plan for each fraction based on the translations and rotations determined from online detection of the fiducial gold markers (which are implanted into the prostate) using portal imaging and deliver the new plan directly to the patient. This work will give us experience performing online plan generation as well as with the specific workflow and QA procedures, which will be necessary when the MRL becomes fully operational, whilst enabling us to improving hypofractionated prostate cancer treatment on conventional linacs at the same time.

9.3 Image segmentation

An essential part of the MRL treatment cycle is the image segmentation phase. The VOI delineated during the simulation phase have to be identified quickly and accurately immediately after the patient has been positioned in the MRL. Since treatment couch adjustments are not possible due to the limited space in the bore of the MRL, the patient position reproducibility is estimated to be under $2.0\ \mathrm{cm}$ which is poor compared to current clinical standards. Therefore, even for relatively simple palliative treatments, MRI-based patient verification, and thus image segmentation, must be performed. For treatments using intrafraction plan adaptation, image segmentation is essential and, due to the time constraints involved, the need for automation is even more urgent.

The most common semi-automatic segmentation approach is manually adapting the contours after rigidly or non-rigidly registering a (manually) segmented simulation MRI (or a segmented MRI of the previous fraction) with a MRI of the current fraction, using intensity based registration methods based on for instance mutual information, cross correlation or optical flow. This method calls for fast, interactive and 3D reviewing and editing tools for the editor, especially when having multiple MRI sequences available which are tailored specifically for different parts of the patient anatomy. The advantage of this approach is that all delineations are reviewed by an editor, who is in the end responsible for the quality of the segmentation. Disadvantages include the vast amount of time it may consume, the associated increase of intrafraction motion as the patient is on the table during the lengthened treatment preparations, and the process has an high level of editor dependence regarding segmentation skills and knowledge.

More advanced segmentation approaches are the model-based or atlas-based segmentation methods. These methods assume that VOI have an approximately standard geometry, with only limited shape variation possible. One of the most attractive features of these methods is that all of the simulation phase data can be used; both intensity and segmentation information can be used to individualize the models for each patient. Drawbacks of these methods are that correctly initializing the underlying models for generic use is hard and the algorithms are usually not very fast.

The previous paragraphs describe methods which handle the acquisition of the images as a separate process from the image segmentation. In other words, the image acquisition is not specifically adapted for the registration/segmentation step afterwards. By designing MRI sequences which are tuned explicitly for a specialized registration al-

gorithm, the speed and accuracy of the registration process can be improved. This principle has been successfully demonstrated by Roujol *et al.* (2010, 2011) for of high-intensity focused ultrasound (HIFU). They show by calibrating their optical flow image registration with the real-time MRI sequences, they can track organ motion up to 10 frames a second. Using these high temporal MRI sequences will in general improve the quality of contour propagation since the anatomy changes between consecutive time points are usually limited.

The VOI generated by automatic image segmentation will need to be reviewed and manually edited, so tools must be available to quickly analyze and modify the VOI. Current contour-based editing is probably not ideal for performing such VOI manipulation operations, editing a single contour has only a very local effect, and in order to achieve a global change, many contours have to be edited. Interactive tools should therefore be developed which directly create or modify the 3D polygonal mesh representation of a VOI. Another option is to use points instead of contours to create a VOI mesh; the points are reconstructed by a surface reconstruction algorithm to form the VOI mesh (Amenta *et al.*, 2001). For regular regions of the VOI only a few points are needed to describe the surface, whereas less uniform regions will obviously require more points to adequately describe the shape. Another advantage is that the input points are not affected by arbitrary image slice orientations as is the case with contours; the points can be added to the VOI at any position the editor wishes. A drawback of this method is that when adding just a single point the reconstruction algorithm can calculate a very different VOI surface, due to the inherently ill-posted nature of the points-to-surface problem.

9.4 Online treatment planning

Just as image segmentation is very important, online treatment planning is also indispensable for every patient group treated on the MRL, since it should at least replace the physical couch shift used on regular linacs. Although a VCS can be performed by shifting the segment shapes according to the detected patient anatomy changes, we opted for a VCS based on plan re-optimization. Due to the fact that the MRL has a fixed collimator angle and a flatting filter free (FFF) beam, the segment shift based VCS can only handle small and specific perturbations of the patient anatomy correctly. The VCS, as it was introduced in chapter 7, does not have these limitations, but does need a reliable online TPS that is compatible with the MRI to successfully implement it. This new setup also means a whole new environment for which the current procedures for QA for plans and treatment delivery do not work anymore and have to be reassessed. These topics will be discussed in the next section.

Instead of rigidly transforming a pre-calculated dose distribution based on the current position of the target structure, the next logical step after implementing the VCS is to create a new treatment plan based on clinical constraints. This regime enhances the "library-of-plans" concept as discussed in the introduction of this thesis: instead of choosing from a fixed set of pre-calculated plans, a new plan is generated for the current fraction. In order to generate such a plan (or plans in the case of using multicriteria optimization) a full set of correct VOI have to be determined from the pre-fraction MRI

images, whereas a VCS can be performed based on information gathered from intensity based registration algorithms or surrogate structures such as anatomical landmarks and fiducial markers.

The next consideration is whether fixed or flexible constraints will be used during plan optimization. With fixed constraints, the optimization goal is to deliver the same dose per fraction to the target, without taking into account whether the patient anatomy is favorable or not. When using flexible constraints, the prescribed dose per fraction may vary within a certain tolerance. Using flexible constraints automatically means that when the anatomy is favorable, the fraction dose will increase and when it is unfavorable the dose will decrease, resulting in a better overall OAR sparing compared to using fixed constraints. Multicriteria plan optimization regimes that are Pareto optimal can be used to accommodate flexible constraints, as implemented for example in the iCycle TPS (Breedveld *et al.*, 2012; Voet *et al.*, 2013). However, the use of flexible constraints adds complexity to the plan optimization process since some form of additional dose tracking is needed to know whether the intended dose to the tumor has been reached and the treatment should be considered complete. When using an uniform dose per fraction, adding up the fractional doses should be sufficient to track the total dose, but in general a proper voxel-by-voxel dose accumulation is required. Dose accumulation typically involves non-rigidly registering the day-to-day MRI images, then accordingly deforming and summing the corresponding dose distributions. Instead of using the accumulated dose as a treatment termination criterion, it is more logical to use it as a bias dose during optimization; by doing this, all previously delivered (non-uniform) dose distributions are incorporated into the optimization process. This last strategy does imply that the dose accumulation process also is carried out when the patient is on the table of the MRL; before the accumulated dose can be used as a bias dose, it should be mapped to the current patient anatomy. When using the accumulated dose as just a termination trigger, this is not needed: the accumulated dose can be computed offline in between fractions, from which the corresponding flexible dose constraints can be derived for the next fraction.

So far only interfraction plan adaptation has been considered. Here we will discuss online treatment planning for intrafraction usage. Online intrafraction planning differs from gated or tracked treatment delivery as discussed earlier, in the sense that with intrafraction plan adaptation, segment shapes are generated during the actual treatment delivery. With gated delivery the segment shapes are known before delivery begins, which is also the case when tracking of the tumor is performed with a static field shape. This tracking mode is however hampered by the same limitations as a virtual couch shift that only shifts the segment shapes; it can only handle small and specific perturbations of the patient anatomy correctly. Therefore treatment planning for tracked delivery remains an open field of research. Intrafraction plan adaptation uses essentially the same MRL cycle as depicted in figure 9.1, but the cycle runs for each individual segment; the current patient anatomy is established, then a new segment is generated and subsequently delivered. Intrafraction plan adaptation therefore changes the current radiotherapy paradigm substantially; it replaces the deterministic fraction delivery by an non-deterministic one.

The change of approach introduced by intrafraction plan adaptation also means that an important part of the current sequencing scheme, the segment weight optimization (SWO), cannot be used anymore. In current TPS all sequencing algorithms use SWO to further minimize the difference between the optimal fluence distribution and the dose distribution which can be delivered by the linac. This step is performed explicitly as a final optimization step in more conventional sequencers; after the segment shapes are generated, the final MU count for each segment is established by SWO. Direct aperture optimizers (DAO) also use SWO but in an implicit manner during the optimization loop itself. Essentially, in order to use SWO, all segment shapes must be predetermined, which is not the case when a generated segment shape with a certain MU count is delivered to the patient. Therefore we are developing a sequencer which can be used to generate immediately deliverable segments without using SWO (Kontaxis *et al.*, 2015). We show that within the intrafraction MRL cycle regime (but not yet within the same timescale, computationally speaking), this sequencer converges for a stable patient anatomy within a few fractions towards the same dose distribution as a sequencer using SWO. Currently, we are investigating the behavior of the new sequencer when using moving patient anatomies and the initial results look very promising.

The current intrafraction sequencer generates step-and-shoot IMRT plans, but in the future we will also investigate whether VMAT IMRT can be implemented. The current intention is to view a single arc of a VMAT treatment as an analogy for a single segment of a step-and-shoot treatment. Furthermore, instead of using at most three arcs for a VMAT treatment, we will use a larger number of arcs, which makes the analogy even stronger, and is better suited to the technical design of the MRL with its high gantry rotation speed of up to $10\ \mathrm{RPM}$.

9.5 Quality assurance

Beside the technical challenges regarding image segmentation, treatment planning and treatment delivery, the QA environment in which the MRL treatment cycle will operate is different from current QA procedures. Due to the sequential nature of the current clinical workflow, the corresponding QA measures follow the same path at the same, relatively slow, timescale in order to guarantee an accurately delivered dose.

When aiming for an online MRL treatment, new QA procedures have to be developed to quickly assess the quality of the MRI acquisition, the image segmentation and registration, the treatment plan quality and dosimetric deliverability, and the linac control and calibration system. Given the online nature of the proposed MRL system, the new procedures will assess the quality of the overall process rather than the individual plans. By performing failure mode and effects analyses (FMEA), the critical steps of the MRL treatment cycle are identified and corresponding dedicated QA procedures are designed to assess the reliability of the system.

Regarding the QA of the MRI acquisition, Crijns *et al.* (2012a) show that distortion-free MRI imaging is feasible with the MRL. Treatment plan quality and/or deliverability and the machine control/calibration system QA is probably achievable in the near future; at our department most IMRT plans are directly delivered to the patient after exten-

sively commissioning of the TPS. The QA of real time machine control (Glitzner *et al.*, 2015; Fast *et al.*, 2014) and new procedures regarding absolute dosimetric calibration in a magnetic field (Smit *et al.*, 2013, 2014) are also progressing rapidly. The QA of the image segmentation and registration processes are, however, still in their infancy. Therefore the development of new image segmentation techniques will initially be combined with independent position verification using portal imaging and/or MRI compatible fiducial markers, in order to gain the much needed QA experience.

9.6 From first-in-man to beyond

At our department we are working hard towards the moment that the first patient is being treated with the MRL. We will test the MRL in a first-in-man study targeting a palliative, single fraction treatment of a spinal bone metastases patient. After the patient has been placed in the MRL, a MRI will be acquired and the CTV delineated by a physician on site. Then the TPS will automatically generate a plan based on a template, which contains specifically designed constraints for this treatment. The Hounsfield information for dose calculation will be provided by a pre-treatment CT which is rigidly registered to the acquired MRI (Hoogcarspel *et al.*, 2014). The quality of the registration will be manually assessed. After the plan is approved by the physician and the position of the patient is double-checked using portal imaging, the treatment plan will be delivered to the patient.

From this first treatment setup onward, we will start adding, replacing and removing components to or from the workflow to accommodate the MRL for other (more complex) treatment sites and fractionation schemes. For example, VCS and supervised automatic image segmentation will be added and CT-based planning will be replaced by MRI-based planning. Portal imaging will become obsolete, since position verification and plan adaptations will be based on the soft-tissue contrasts provided by the MRI. We will go from pre-fraction MRI scans to locate the tumor to intrafraction MRI sequences to follow the position of the tumor. We will move from interfraction to intrafraction plan adaptation and from supervised plan selection to unsupervised online plan alterations, from "human" monitored QA procedures to automatic QA procedures. All of this will change the radiotherapy paradigm from an offline MRI-aided to an online MRI-guided one, improving the effectiveness of external beam radiotherapy as a cancer therapy.

10

Samenvatting

Dit proefschrift beschrijft een aantal verbeteringen voor de behandeling van kanker door middel van radiotherapie. De eerste verbetering heeft te maken met de klassieke patientpositieverificatie die gebaseerd is op portal imaging. De andere belangrijke verbetering hangt samen met het toevoegen van MRI aan de huidige radiotherapiebehandeling. In het verlengde daarvan beschrijft dit proefschrift ook de eerste stappen naar daadwerkelijk online MRI-gestuurde radiotherapie.

Bij positieverificatiemethoden die gebaseerd zijn op portal imaging kan zich het probleem voordoen dat ieder afzonderlijke portal image van een segment van een (IMRT) bestralingsbundel te weinig informatie bevat om een goede botregistratie uit te kunnen voeren. In hoofdstuk 2 van dit proefschrift worden twee offline positieverificatiemethoden geïntroduceerd die ook in dit geval de botposities van de patiënt automatisch kunnen detecteren. Hierdoor zijn extra positieverificatiebundels niet meer nodig waardoor de behandeling minder lang duurt en de stralingsbelasting van de patiënt minder wordt. De eerste methode is de "stack matching method". Hierbij worden alle portal images van alle segmenten gestapeld tot een 3D volume, en dit volume wordt vervolgens tijdens de registratieprocedure gebruikt. De twee methode is the "averaged projection matching method". Deze methode is een versimpeling van de eerste methode, doordat het initieel gecreëerde 3D volume weer gereduceerd wordt tot een artificieel 2D plaatje. Daardoor wordt de registratie veel sneller zonder dat dat merkbaar ten koste gaat van de nauwkeurigheid. De methoden worden vergeleken met de standaard positieverificatiemethoden. Daaruit blijkt dat voor zowel fantoom- als patiëntstudies de resultaten vergelijkbaar zijn.

Hoofdstuk 3 beschrijft een softwarepakket waarmee tumoren beter kunnen worden ingetekend, doordat meerdere beeldvormende modaliteiten simultaan gebruikt kunnen worden. Het pakket is met name geschikt voor situaties waarin er meerdere MRI sequenties van een patiënt beschikbaar zijn, naast de standaard radiotherapie planning CT. Het systeem is op twee grondbeginselen gebaseerd. Ten eerste wordt iedere dataset in zijn originele vorm weergegeven (coördinaatsysteem, spatiële resolutie, voxelafmetingen en plakoriëntatie). Ten tweede kan er op alle orthogonale vlakken van iedere dataset worden ingetekend en de aanpassingen van de intekeningen worden direct zichtbaar op alle andere datasets. Hierdoor kan de gebruiker direct zien of de aanpassing consistent is met de andere modaliteiten. Het grootste verschil ten opzichte van andere

intekenpakketten is dat intekeningen naar de verschillende datasets worden overgezet in plaats van dat alle beeldvormende datasets naar één overkoepelend 3D grid wordt overgezet, waardoor specifieke contrasten verloren kunnen gaan.

Het gebruik van MRI-compatible goudmarkers wordt in hoofdstuk 4 bediscussieerd. Conventionele goudmarkers zijn slecht zichtbaar op de meeste MRI sequenties, waardoor de markers op een aparte CT gedetecteerd moeten worden. Dit zorgt ervoor dat er een extra CT-MRI registratie nodig is die daardoor ook een extra foutmarge in de hele voorbereidingsfase van een radiotherapiebehandeling veroorzaakt. We hebben een marker ontwikkeld die zowel op EPID als op MRI zichtbaar is, waardoor de CT-MRI registratiestap niet meer nodig is. De marker bestaat uit een stalen kern met een diameter van $0.3\ \mathrm{mm}$ met daaromheen een laagje goud. In totaal is de marker $5.0\ \mathrm{mm}$ lang en heeft een diameter van $1.0\ \mathrm{mm}$. De stalen kern zorgt ervoor dat de marker zichtbaar is op MRI en het gouden laagje eromheen zorgt voor de zichtbaarheid op EPID. Onderzocht is wat de interobserver variabiliteit is ten aanzien van de locatie van de marker in drie verschillende MRI sequenties: een bSSFP, een T1- en een T2-gewogen sequentie. Vijf ervaren observers hebben op alle sequenties de markerposities aangegeven en deze zijn vergeleken met de CT gebaseerde markerposities. Hieruit is geconcludeerd dat the bSSFP sequentie het meest geschikt is om zowel de prostaat als de markers te detecteren. De gemiddelde absolute afstand varieerde voor deze sequentie tussen de $0.16\ \mathrm{mm}$ en $0.30\ \mathrm{mm}$. Deze waarden zijn inclusief CT-MRI registratiefouten. Ook voor de andere MRI sequenties waren de afstanden klein: tussen $0.43\ \mathrm{mm}$ en $1.44\ \mathrm{mm}$. Dit betekent dat door gebruik te maken van deze goudmarkers de systematische fout van de totale behandeling kan worden verkleind.

Vanaf hoofdstuk 5 wordt het focus van dit proefschrift verlegd van offline MRI-ondersteunde radiotherapie naar online MRI-gestuurde radiotherapie. Als onderdeel daarvan wordt in hoofdstuk 5 een planning systeem geïntroduceerd voor de MRL. De MRL is in staat om voortdurend de anatomie van een patiënt volgen. Zo kunnen translaties, rotaties en deformaties van tumoren en omliggende gezonde weefsels in beeld worden gebracht, zelfs tijdens de radiotherapie behandeling. Om deze informatie te kunnen gebruiken om de behandeling aan te kunnen passen, is een IMRT heroptimalisatie routine nodig die snel genoeg is om dit te kunnen faciliteren. In dit hoofdstuk wordt zo'n systeem gepresenteerd. Het bestaat uit een GPU-gebaseerde Monte-Carlo dose engine (GPUMCD) en een snelle inverse dosis optimalisatie routine (FIDO). Het systeem is in staat om conformale IMRT plannen te genereren, ook als er een sterk magneetveld van $1.5\ \mathrm{T}$ aanwezig is. Verder laten we zien dat het systeem snel genoeg is om online een nieuw IMRT plan te kunnen maken en dat er geen invloed van het magneetveld zichtbaar is ten aanzien van plan kwaliteit en complexiteit. Daarnaast is gebleken dat dezelfde verzameling optimalisatie constraints leidt tot bijna identieke dosis verdelingen, onafhankelijk van de aanwezigheid van het $1.5\ \mathrm{T}$ magneetveld.

In hoofdstuk 6 wordt het effect van bewegende, bolvormige luchtholten op IMRT dosisverdelingen in magneetvelden van $0.35\ \mathrm{T}$ en $1.5\ \mathrm{T}$ bestudeerd door middel van Monte-Carlo simulaties. We tonen aan dat de effecten van het ERE rond dit soort holten met IMRT kunnen worden opgeheven. Echter, als er tijdens een fractie een luchtholte ontstaat of verdwijnt, dan is compensatie van het ERE niet mogelijk. In deze gevallen kan

gating of heroptimalisatie van het behandelingsplan uitkomst bieden. Ook is er onderzoek uitgevoerd ten aanzien van het gebruik van in 0 T geoptimaliseerde plannen, afgegeven in een 0.35 T en een 1.5 T omgeving. In het 0.35 T geval, wordt het ERE net zo goed gecompenseerd door het 0 T als door het 0.35 T geoptimaliseerde plan. In een 1.5 T omgeving, is het 1.5 T plan iets beter dan het 0 T plan voor statische luchtholten en luchtholten die random tijdens of tussen de fracties bewegen. Bij bewegende luchtholten met een baseline shift resulteert het 0 T plan in een betere dosisverdeling. Deze resultaten laten zien dat het ERE voornamelijk gecompenseerd wordt door opposing beam configuraties. IMRT kan voor nog betere compensatie zorgen, maar alleen als de luchtholte zich daadwerkelijk op de geplande positie bevindt.

Hoofdstuk 7 introduceert de eerste stap richting daadwerkelijk online MRI-gestuurde radiotherapie met de MRL. Als een patiënt met een conventioneel IMRT plan wordt bestraald, wordt er geprobeerd om de verschillen van de patiëntanatomie ten tijde van de planning CT en ten tijde van de behandeling te minimaliseren door de behandeltafel waarop de patiënt ligt te transleren en tot op zekere hoogte te roteren. Grote rotaties kunnen echter niet opgevangen worden op deze manier. In dit hoofdstuk wordt een nieuw concept geïntroduceerd: een online "virtual couch shift" (VCS). De dosisverdeling die vooraf berekend is wordt op basis van de gemeten translaties en rotaties op dezelfde wijze getransleerd en geroteerd en hiervoor wordt online en automatisch een nieuw behandelplan gegenereerd. Voor zowel een fantoom als voor een baarmoederhalskankerpatiënt laten we zien dat dit concept werkt voor zowel translaties als voor grote rotaties. De validatie vond plaats door DVH vergelijkingen en $2\%/2$ mm γ analyses. Als de verschillende aspecten binnen de klinische workflow kunnen worden geïmplementeerd, dan kan een VCS mogelijk beter presteren dan een fysieke tafelverplaatsing. Dit werk is uitgevoerd in het kader van de MRL, die naast translatie- en/of rotatieinformatie, ook deformaties van de patiëntanatomie kan detecteren. De VCS is dan ook de eerste stap richting volledige compensatie van alle anatomische veranderingen binnen een patiënt door middel van het online heroptimaliseren van een IMRT dosisverdeling.

Bibliography

Ahmad R., Hoogeman M.S., Quint S., Mens J.W., Osorio E.M. and Heijmen B.J. 2012 Residual setup errors caused by rotation and non-rigid motion in prone-treated cervical cancer patients after online CBCT image-guidance *Radiotherapy and Oncology* **103** 322–326

Ahnesjö A. 1989 Collapsed cone convolution of radiant energy for photon dose calculation in heterogeneous media *Medical Physics* **16** 577–592

Amenta N., Choi S. and Kolluri R. 2001 The power crust, unions of balls, and the medial axis transform *Computational Geometry: Theory and Applications* **19** 127–153

Antonuk L.E. 2002 Electronic portal imaging devices: a review and historical perspective of contemporary technologies and research *Physics in Medicine and Biology* **47** R31–R65

Bakker C.J.G., Moerland M.A., Bhagwandien R. and Beersma R. 1992 Analysis of machine-dependent and object-induced geometric distortions in 2DFT MR imaging *Magnetic Resonance Imaging* **10** 597–608

Bel A., Van Herk M., Bartelink H. and Lebesque J.V. 1993 A verification procedure to improve patient set-up accuracy using portal images *Radiotherapy and Oncology* **29** 253–260

Berker Y., Franke J., Salomon A., Palmowski M., Donker H.C., Temur Y., Mottaghy F.M., Kuhl C., Izquierdo-Garcia D., Fayad Z.A., Kiessling F. and Schulz V. 2012 MRI-based attenuation correction for hybrid PET/MRI systems: a 4-class tissue segmentation technique using a combined ultrashort-echo-time/Dixon MRI sequence *Journal of Nuclear Medicine* **53** 796–804

Boissonnat J.D. 1988 Shape reconstruction from planar cross sections *Computer Vision, Graphics, and Image Processing* **44** 1–29

Bol G.H., Hissoiny S., Lagendijk J.J.W. and Raaymakers B.W. 2012 Fast online Monte Carlo-based IMRT planning for the MRI linear accelerator *Physics in Medicine and Biology* **57** 1375–1385

Bol G.H., Kotte A.N.T.J., Van der Heide U.A. and Lagendijk J.J.W. 2009 Simultaneous multi-modality ROI delineation in clinical practice *Computer methods and programs in Biomedicine* **96** 133–140

Bol G.H., Lagendijk J.J.W. and Raaymakers B.W. 2013 Virtual couch shift (VCS): accounting for patient translation and rotation by online IMRT re-optimization *Physics in Medicine and Biology* **58** 2989–3000

Bol G.H., Lagendijk J.J.W. and Raaymakers B.W. 2015 Compensating for the impact of non-stationary spherical air cavities on IMRT dose delivery in transverse magnetic fields *Physics in Medicine and Biology* **60** 755–768

Bol G.H., Van der Heide U.A., Kotte A.N.T.J., van Vulpen M. and Lagendijk J.J.W. 2008 MRI-compatible fiducial gold markers for prostate cancer patients in *Radiotherapy and Oncology proc. ESTRO 27, Göteborg, Sweden* vol. 88, suppl 2, nr 1171 p. S374

Bol G.H., Van der Heide U.A., Nederveen A.J., Kotte A.N.T.J. and Lagendijk J.J.W. 2006 Patient position verification using small IMRT fields *Medical Physics* **33** 2344–2353

Breedveld S., Storchi P.R., Voet P.W. and Heijmen B.J. 2012 iCycle: Integrated, multicriterial beam angle, and profile optimization for generation of coplanar and noncoplanar IMRT plans *Medical Physics* **39** 951–963

Brown R.W., Norman Cheng Y.C., Haacke E.M., Thompson M.R. and Venkatesan R. 2014 *Magnetic Resonance Imaging: Physical Principles and Sequence Design* (Wiley-Blackwell) 2nd edn.

Cao D., Earl M.A., Luan S. and Shepard D.M. 2006 Continuous intensity map optimization (CIMO): a novel approach to leaf sequencing in step and shoot IMRT *Medical Physics* **33** 859–867

Ceylan C., Van der Heide U.A., Bol G.H., Lagendijk J.J.W. and Kotte A.N.T.J. 2005 Assessment of rigid multi-modality image registration consistency using the multiple sub-volume registration (msr) method *Physics in Medicine and Biology* **50**

Crijns S.P.M., Bakker C.J.G., Seevinck P.R., de Leeuw H., Lagendijk J.J.W. and Raaymakers B.W. 2012a Towards inherently distortion-free MR images for image-guided radiotherapy on an MRI accelerator *Physics in Medicine and Biology* **57** 1349–1358

Crijns S.P.M., Kok J.G.M., Lagendijk J.J.W. and Raaymakers B.W. 2011 Towards MRI-guided linear accelerator control: gating on an MRI accelerator *Physics in Medicine and Biology* **56** 4815–4825

Crijns S.P.M., Raaymakers B.W. and Lagendijk J.J.W. 2012b Proof of concept of MRI-guided tracked radiation delivery: tracking one-dimensional motion *Physics in Medicine and Biology* **57** 7863–7872

Daftari I., Aghaian E., O'Brien J.M., Dillon W. and Phillips T.L. 2005 3d mri-based tumor delineation of ocular melanoma and its comparison with conventional techniques *Medical Physics* **32** 3355–3362

De Boer H.C.J. and Heijmen B.J.M. 2001a A protocol for the reduction of systematic patient setup errors with minimal portal imaging workload *International Journal of Radiation Oncology, Biology and Physics* **50** 1350–1365

De Boer H.C.J., van Sörnsen de Koste J.R., Creutzberg C.L., Visser A.G., Levendag P.C. and Heijmen B.J.M. 2001b Electronic portal image assisted reduction of systematic set-up errors in head and neck irradiation *Radiotherapy and Oncology* **61** 299–308

De Meerleer G., Villeirs G., Bral S., Paelinck L., De Gersem W., Dekuyper P. and De Neve W. 2005 The magnetic resonance detected intraprostatic lesion in prostate cancer: planning and delivery of intensity-modulated radiotherapy *Radiotherapy and Oncology* **75** 325–333

Dehnad H., Nederveen A.J., Van der Heide U.A., Van Moorselaar R.J.A., Hofman P. and Lagendijk J.J.W. 2003 Clinical feasibility study for the use of implanted gold seeds in the prostate as reliable positioning markers during megavoltage irradiation *Radiotherapy and Oncology* **67** 295–302

Dempsey J.F., Benoit D., Fitzsimmons J.R., Haghighat A., Li J.G., Low D.A., Mutic S., Palta J.R., Romeijn H.E. and Sjoden G.E. 2005 A device for realtime 3D image-guided IMRT in *ASTRO Denver* 47^{th} Annual Meeting

Esthappan J., Mutic S., Malyapa R.S., Grigsby P.W., Zoberi I., Dehdashti F., Miller T.R., Bosch W.R. and Low D.A. 2004 Treatment planning guidelines regarding the use of CT/PET-guided IMRT for cervical carcinoma with positive paraaortic lymph nodes *International Journal of Radiation Oncology, Biology and Physics* **58** 1289–1297

Fallone B.G., Murray B., Rathee S., Stanescu T., Steciw S., Vidakovic S., Blosser E. and Tymofichuk D. 2009 First MR images obtained during megavoltage photon irradiation from a prototype integrated linac-MR system *Medical Physics* **36** 2084–2088

Fast M.F., Nill S., Bedford J.L. and Oelfke U. 2014 Dynamic tumor tracking using the Elekta Agility MLC *Medical Physics* **41** 111719

Feng M., Balter J.M., Normolle D., Adusumilli S., Cao Y., Chenevert T.L. and Ben-Josef E. 2009 Characterization of pancreatic tumor motion using cine MRI: surrogates for tumor position should be used with caution *International Journal of Radiation Oncology, Biology and Physics* **74** 884–891

Fielding A.L., Evans P.M. and Clark C.H. 2004 Verification of patient position and delivery of imrt by electronic portal imaging *Radiotherapy and Oncology* **73** 339–347

Foley J.D., van Dam A., Feiner S.K., Hughes J.F. and Philips R.L. 1994 *Introduction to Computer Graphics* (Reading, USA: Addison-Wesley)

Ford E.C., Mageras G.S., Yorke E. and Ling C.C. 2003 Respiration-correlated spiral CT: a method of measuring respiratory-induced anatomic motion for radiation treatment planning *Medical Physics* **30** 88–97

Gilhuijs K.G.A., Van de Ven P.J.H. and Van Herk M. 1996 Automatic three-dimensional inspection of patient setup in radiation therapy using portal images, simulator images, and computed tomography data *Medical Physics* **23** 389–399

Glitzner M., Crijns S.P., de Senneville B.D., Lagendijk J.J.W. and Raaymakers B.W. 2015 On the suitability of Elekta's Agility 160 MLC for tracked radiation delivery: closed-loop machine performance *Physics in Medicine and Biology* **60** 2005–2017

Goldman S.P., Chen J.Z. and Battista J.J. 2005 Feasibility of a fast inverse dose optimization algorithm for IMRT via matrix inversion without negative beamlet intensities *Medical Physics* **32** 3007–3016

Goldman S.P., Thurnbull D., Johnson C., Chen J.Z. and Battista J.J. 2009 Real-time fast inverse dose optimization for image guided adaptive radiation therapyâĂŞEnhancements to fast inverse dose optimization

(FIDO) *Journal of Applied Physics* **105** 102008

Grosu A.L., Piert M., Weber W.A., Jeremic B., Picchio M., Schratzenstaller U., Zimmermann F.B., Schwaiger M. and Molls M. 2005 Positron emission tomography for radiation treatment planning *Strahlentherapie und Onkologie* **181** 483–499

Hajnal J.V., Hawkes D.J. and Hill D.L.G. (eds.) 2001 *Medical Image Registration* chap. Non rigid registration: concepts, algorithms and applications, pp. 281–302 (Boca Raton, Florida, USA: CRC Press)

Harris E.J., McNair H.A. and Evans P.M. 2006 Feasibility of fully automated detection of fiducial markers implanted into the prostate using electronic portal imaging: a comparison of methods *International Journal of Radiation Oncology, Biology and Physics* **66** 1263–1270

Hill D.L.G., Batchelor P.G., Holden M. and J H.D. 2001 Medical image registration *Physics in Medicine and Biology* **46** R1–R45

Hissoiny S., Ozell B., Bouchard H. and Despres P. 2011a GPUMCD: A new GPU-oriented Monte Carlo dose calculation platform *Medical Physics* **38** 754–764

Hissoiny S., Raaijmakers A.J., Ozell B., Despres P. and Raaymakers B.W. 2011b Fast dose calculation in magnetic fields with GPUMCD *Physics in Medicine and Biology* **56** 5119–5129

Hoogcarspel S.J., Van der Velden J.M., Lagendijk J.J.W., van Vulpen M. and Raaymakers B.W. 2014 The feasibility of utilizing pseudo CT-data for online MRI based treatment plan adaptation for a stereotactic radiotherapy treatment of spinal bone metastases *Physics in Medicine and Biology* **59** 7383–7391

Hsu S.H., Cao Y., Huang K., Feng M. and Balter J.M. 2013 Investigation of a method for generating synthetic CT models from MRI scans of the head and neck for radiation therapy *Physics in Medicine and Biology* **58** 8419–8435

Hughes S., McClelland J., Chandler A., Adams M., Boutland J., Withers D., Ahmad S., Blackall J., Tarte S., Hawkes D. and Landau D. 2008 A comparison of internal target volume definition by limited four-dimensional computed tomography, the addition of patient-specific margins, or the addition of generic margins when planning radical radiotherapy for lymph node-positive non-small cell lung cancer *Clinical Oncology* **20** 293–300

Huisman H.J., Fütterer J.J., van Lin E.N., Welmers A., Scheenen T.W., van Dalen J.A., Visser A.G., Witjes J.A. and Barentsz J.O. 2005 Prostate cancer: precision of integrating functional MR imaging with radiation therapy treatment by using fiducial gold markers *Radiology* **236** 311–317

ICRU Report No. 50 1993 *Prescribing, recording and reporting photon beam therapy* (ICRU Bethesda Maryland)

Jaffray D.A., Yan D. and Wong J.W. 1999 Managing geometric uncertainty in conformal intensity-modulated radiation therapy *Seminars in Radiation Oncology* **9** 4–19

Jiang H., Seco J. and Paganetti H. 2007 Effects of Hounsfield number conversion on CT based proton Monte Carlo dose calculations *Medical Physics* **34** 1439–1449

Johansson A., Karlsson M. and Nyholm T. 2011 CT substitute derived from MRI sequences with ultrashort echo time *Medical Physics* **38** 2708–2714

Karlsson M., Karlsson M.G., Nyholm T., Amies C. and Zackrisson B. 2009 Dedicated magnetic resonance imaging in the radiotherapy clinic *International Journal of Radiation Oncology, Biology and Physics* **74** 644–651

Keall P. 2004 4-dimensional computed tomography imaging and treatment planning *Seminars in Radiation Oncology* **14** 81–90

Kerkhof E.M., Van der Put R.W., Raaymakers B.W., Van der Heide U.A., Van Vulpen M. and Lagendijk J.J.W. 2008 Variation in target and rectum dose due to prostate deformation: an assessment by repeated MR imaging and treatment planning. *Physics in Medicine and Biology* **53** 5623–5634

Khoo V.S. and Joon D.L. 2006 New developments in mri for target volume delineation in radiotherapy *British Journal of Radiology* **79** S2–15

Kirkby C., Stanescu T. and Fallone B.G. 2009 Magnetic field effects on the energy deposition spectra of MV photon radiation *Physics in Medicine and Biology* **54** 243–257

Kirkby C., Stanescu T., Rathee S., Carlone M., Murray B. and G F.B. 2008 Patient dosimetry for hybrid mri-radiotherapy systems *Medical Physics* **35** 1019–27

Kontaxis C., Bol G.H., Lagendijk J.J.W. and Raaymakers B.W. 2015 Towards adaptive IMRT sequencing for the MR-linac *Physics in Medicine and Biology* **60** 2493–2509

Korhonen J., Kapanen M., Keyrilainen J., Seppala T. and Tenhunen M. 2014 A dual model HU conversion from MRI intensity values within and outside of bone segment for MRI-based radiotherapy treatment planning

of prostate cancer *Medical Physics* **41** 011704

Lagendijk J.J.W. and Bakker C.J.G. 2000 MRI guided radiotherapy: a MRI based linear accelerator in *ESTRO Istanbul* 19th Annual Meeting

Lagendijk J.J.W., Raaymakers B.W., Raaijmakers A.J.E., Overweg J., Brown K.J., Kerkhof E.M., Van der Put R.W., Hårdemark B., Van Vulpen M. and Van der Heide U.A. 2008 MRI/linac integration *Radiotherapy and Oncology* **86** 25–29

Lagendijk J.J.W., Raaymakers B.W., Van Der Heide U.A., Topolnjak R., Dehnad H., Hofman P., Nederveen A.J., Schulz I.M., Welleweerd J. and Bakker C.J.G. 2002 Mri guided radiotherapy: Mri as position verification system for imrt in *Radiotherapy and Oncology* vol. 64 (Suppl. 1) pp. S75–76 Prague, Czech Republic European Society for Therapeutic Radiation Oncology

Lagerburg V., Moerland M.A., Seppenwoolde J.H. and Lagendijk J.J.W. 2008 Simulation of the artefact of an iodine seed placed at the needle tip in MRI-guided prostate brachytherapy *Physics in Medicine and Biology* **53** 59–67

Langen K.M. and Jones D.T.L. 2001 Organ motion and its management *International Journal of Radiation Oncology, Biology and Physics* **50** 265–278

Linthout N., Verellen D., Tournel K., Reynders T., Duchateau M. and Storme G. 2007 Assessment of secondary patient motion induced by automated couch movement during on-line 6 dimensional repositioning in prostate cancer treatment **83** 168–174

Lips I.M., Van der Heide U.A., Kotte A.N., van Vulpen M. and Bel A. 2009 Effect of translational and rotational errors on complex dose distributions with off-line and on-line position verification *International Journal of Radiation Oncology, Biology and Physics* **74** 1600–1608

Liu H.H., Mackie T.R. and McCullough E.C. 1997 A dual source photon beam model used in convolution/superposition dose calculations for clinical megavoltage x-ray beams *Medical Physics* **24** 1960–1974

Lötjönen J. 2003 Construction of patient-specific surface models from MR images: application to bioelectromagnetism *Comput Methods Programs Biomed* **72** 167–178

Lötjönen J.M., Järvinen V.M., Cheong B., Wu E., Kivistö S., Koikkalainen J.R., Mattila J.J., Kervinen H.M., Muthupillai R., Sheehan F.H. and Lauerma K. 2008 Evaluation of cardiac biventricular segmentation from multiaxis MRI data: a multicenter study *J Magn Reson Imaging* **28** 626–636

Low D.A., Harms W.B., Mutic S. and Purdy J.A. 1998 A technique for the quantitative evaluation of dose distributions *Medical Physics* **25** 656–661

Low D.A., Nystrom M., Kalinin E., Parikh P., Dempsey J.F., Bradley J.D., Mutic S., Wahab S.H., Islam T., Christensen G., Politte D.G. and Whiting B.R. 2003 A method for the reconstruction of four-dimensional synchronized CT scans acquired during free breathing *Medical Physics* **30** 1254–1263

Mackie T.R., Ahnesjö A., Dickof P. and Snider A. 1987 Development of a convolution/superposition method for photon beams in *The Use of Computers in Radiation Therapy* pp. 107–110 ICCR

Maes F., Collignon A., Vandermeulen D., Marchal G. and Suetens P. 1997 Multimodality image registration by maximization of mutual information *IEEE Transactions on Medical Imaging* **16** 187–198

McNair H.A., Hansen V.N., Parker C.C., Evans P.M., Norman A., Miles E., Harris E.J., Del-Acroix L., Smith E., Keane R., Khoo V.S., Thompson A.C. and Dearnaley D.P. 2008 A comparison of the use of bony anatomy and internal markers for offline verification and an evaluation of the potential benefit of online and offline verification protocols for prostate radiotherapy *International Journal of Radiation Oncology, Biology and Physics* **71** 41–50

Meijer G.J., Bruinvis I.A.D., Mijnheer B.J. and Lebesque J.V. 2000 A treatment planning method to correct dose distributions distored by setup verification fields *International Journal of Radiation Oncology, Biology and Physics* **46** 1319–1328

Meyer J., Wilbert J., Baier K., Guckenberger M., Richter A., Sauer O. and Flentje M. 2007 Positioning accuracy of cone-beam computed tomography in combination with a HexaPOD robot treatment table *International Journal of Radiation Oncology, Biology and Physics* **67** 1220–1228

Mijnheer B., Olszewska A., Fiorino C., Hartmann G., Knöös T., Rosenwald J.C. and Welleweerd H. 2004 *Quality assurance of treatment planning system - Practical examples for non-imrt photon beams* (Brussels, Belgium: ESTRO) ESTRO Booklet Nr. 7

Moerland M.A., Beersma R., Bhagwandien R., Wijrdeman H.K. and Bakker C.J.G. 1995 Analysis and correction of geometric distortions in 1.5 T magnetic resonance images for use in radiotherapy treatment planning *Physics in Medicine and Biology* **40** 1651–1664

Mohan R., Zhang X., Wang H., Kang Y., Wang X., Liu H., Ang K.K., Kuban D. and Dong L. 2005 Use of deformed intensity distributions for on-line modification of image-guided imrt to account for interfractional anatomic changes *International Journal of Radiation Oncology, Biology and Physics* **61** 1258–66

Moseley J. and Munro P. 1993 Display equalization: A new display method for portal images *Medical Physics* **20** 99–102

Moureau-Zabotto L., Touboul E., Lerouge D., Deniaud-Alexandre E., Grahek D., Foulquier J.N., Petegnief Y., Gres B., El Balaa H., Kerrou K., Montravers F., Keraudy K., Tiret E., Gendre J.P., Grange J.D., Houry S. and Talbot J.N. 2005 Impact of CT and 18F-deoxyglucose positron emission tomography image fusion for conformal radiotherapy in esophageal carcinoma *International Journal of Radiation Oncology, Biology and Physics* **63** 340–345

Murthy V., Master Z., Adurkar P., Mallick I., Mahantshetty U., Bakshi G., Tongaonkar H. and Shrivastava S. 2011 'Plan of the day' adaptive radiotherapy for bladder cancer using helical tomotherapy *Radiotherapy and Oncology* **99** 55–60

Nederveen A.J., Dehnad H., Van der Heide U.A., Van Moorselaar R.J.A., Hofman P. and Lagendijk J.J.W. 2002 Comparison of megavoltage position verification for prostate irradiation based on bony anatomy and implanted fiducials *International Journal of Radiation Oncology, Biology and Physics* (submitted)

Nederveen A.J., Dehnad H., Van der Heide U.A., Van Moorselaar R.J.A., Hofman P. and Lagendijk J.J.W. 2003 Comparison of megavoltage position verification for prostate irradiation based on bony anatomy and implanted fiducials *Radiotherapy and Oncology* **68** 81–88

Ng L. and Ibáñez L. 2003 *Narrow Band to Image Registration in the Insight Toolkit* vol. 2717 of *Lecture Notes in Computer Science* (Springer-Verlag GmbH)

Niu T., Sun M., Star-Lack J., Gao H., Fan Q. and Zhu L. 2010 Shading correction for on-board cone-beam CT in radiation therapy using planning MDCT images *Med Phys* **37** 5395–5406

Nutting C., Dearnaley D.P. and Webb S. 2000 Intensity modulated radiation therapy, a clinical review *British Journal of Radiology* **73** 459–469

Oborn B.M., Metcalfe P.E., Butson M.J. and Rosenfeld A.B. 2009 High resolution entry and exit Monte Carlo dose calculations from a linear accelerator 6 MV beam under the influence of transverse magnetic fields *Medical Physics* **36** 3549–3559

Oborn B.M., Metcalfe P.E., Butson M.J. and Rosenfeld A.B. 2010 Monte Carlo characterization of skin doses in 6 MV transverse field MRI-linac systems: effect of field size, surface orientation, magnetic field strength, and exit bolus *Medical Physics* **37** 5208–5217

Parker C.C., Damyanovich, Haycocks T., Haider M., Bayley A. and Catton C.N. 2003 Magnetic resonance imaging in the radiation treatment planning of localized prostate cancer using intra-prostatic fiducial markers for computed tomography co-registration *Radiotherapy and Oncology* **66** 217–224

Pfaffenberger A. 2013 *Dose Calculation Algorithms for Radiation Therapy with an MRI-Integrated Radiation Device* Ph.D. thesis German Cancer Research Center (DKFZ)

Pluim J.P.W., Maintz J.B.A. and Viergever M.A. 2003 Mutual-information-based registration of medical images: a survey. *IEEE Trans Med Imaging* **22** 986–1004

Raaijmakers A.J.E., Hårdemark B., Raaymakers B.W., Raaijmakers C.P.J. and Lagendijk J.J.W. 2007a Dose optimization for the MRI-accelerator: IMRT in the presence of a magnetic field *Physics in Medicine and Biology* **52** 7045–54

Raaijmakers A.J.E., Raaymakers B.W. and Lagendijk J.J.W. 2005a Integrating a MRI scanner with a 6 MV radiotherapy accelerator: Dose increase at tissue-air interfaces in a lateral magnetic field due to returning electrons *Physics in Medicine and Biology* **50** 1363–76

Raaijmakers A.J.E., Raaymakers B.W., Van der Meer S. and Lagendijk J.J.W. 2007b Integrating a mri scanner with a 6 mv radiotherapy accelerator: impact of the surface orientation on the entrance and exit dose due to the transverse magnetic field. *Physics in Medicine and Biology* **52** 929–39

Raaijmakers A.J.E., Raaymakers B.W. and W L.J.J. 2005b Integrating a MRI scanner with a 6 MV radiotherapy accelerator: dose increase at tissue-air interfaces in a lateral magnetic field due to returning electrons *Physics in Medicine and Biology* **50** 1363–1376

Raaymakers B.W., de Boer J.C., Knox C., Crijns S.P., Smit K., Stam M.K., van den Bosch M.R., Kok J.G. and Lagendijk J.J.W. 2011 Integrated megavoltage portal imaging with a 1.5 T MRI linac *Physics in Medicine and Biology* **56** N207–214

Raaymakers B.W., Lagendijk J.J.W., Overweg J., Kok J.G.M., Raaijmakers A.J.E., Kerkhof E.M., Van der Put R.W., Meijsing I., Crijns S.P.M., Benedosso F., Van Vulpen M., De Graaff C.H.W., Allen J. and Brown K.J.

2009 Integrating a 1.5 T MRI scanner with a 6 MV accelerator: proof of concept. *Physics in Medicine and Biology* **54** N229–237

Raaymakers B.W., Raaijmakers A.J.E., Kotte A.N.T.J., Jette D. and Lagendijk J.J.W. 2004 Integrating a MRI scanner with a 6 MV radiotherapy accelerator: dose deposition in a transverse magnetic field *Physics in Medicine and Biology* **49** 4109–4118

Rijkhorst E.J., Lakeman A., Nijkamp J., de Bois J., van Herk M., Lebesque J.V. and Sonke J.J. 2009 Strategies for online organ motion correction for intensity-modulated radiotherapy of prostate cancer: prostate, rectum, and bladder dose effects *International Journal of Radiation Oncology, Biology and Physics* **75** 1254–1260

Rong Y., Smilowitz J., Tewatia D., Tome W.A. and Paliwal B. 2010 Dose calculation on kV cone beam CT images: an investigation of the Hu-density conversion stability and dose accuracy using the site-specific calibration *Medical Dosimetry* **35** 195–207

Roujol S., Ries M., Moonen C. and Denis de Senneville B.D. 2011 Automatic nonrigid calibration of image registration for real time MR-guided HIFU ablations of mobile organs *IEEE Transactions on Medical Imaging* **30** 1737–1745

Roujol S., Ries M., Quesson B., Moonen C. and Denis de Senneville B. 2010 Real-time MR-thermometry and dosimetry for interventional guidance on abdominal organs *Magnetic Resonance in Medicine* **63** 1080–1087

Sanderson S. 2010 Armadillo: An open source c++ linear algebra library for fast prototyping and computationally intensive experiments Tech. rep. NICTA Australia

Schiffner D.C., Gottschalk A.R., Lometti M., Aubin M., Pouliot J., Speight J., Hsu I.C., Shinohara K. and Roach M. 2007 Daily electronic portal imaging of implanted gold seed fiducials in patients undergoing radiotherapy after radical prostatectomy *International Journal of Radiation Oncology, Biology and Physics* **67** 610–619

Smit K., Sjoholm J., Kok J.G., Lagendijk J.J.W. and Raaymakers B.W. 2014 Relative dosimetry in a 1.5 T magnetic field: an MR-linac compatible prototype scanning water phantom *Physics in Medicine and Biology* **59** 4099–4109

Smit K., van Asselen B., Kok J.G., Aalbers A.H., Lagendijk J.J.W. and Raaymakers B.W. 2013 Towards reference dosimetry for the MR-linac: magnetic field correction of the ionization chamber reading *Physics in Medicine and Biology* **58** 5945–5957

Smith W.L., Lewis C., Bauman G., Rodrigues G., D'Souza D., Ash R., Ho D., Venkatesan V., Downey D. and Fenster A. 2007 Prostate volume contouring: a 3D analysis of segmentation using 3DTRUS, CT, and MR *International Journal of Radiation Oncology, Biology and Physics* **67** 1238–1247

Stemkens B., Tijssen R.H., de Senneville B.D., Heerkens H.D., van Vulpen M., Lagendijk J.J.W. and van den Berg C.A.T. 2015 Optimizing 4-Dimensional Magnetic Resonance Imaging Data Sampling for Respiratory Motion Analysis of Pancreatic Tumors *International Journal of Radiation Oncology, Biology and Physics*

Studholme C., Hill D.L.G. and Hawkes D.J. 1999 An overlap invariant entropy measure of 3D medical image alignment *Pattern Recognition* **32** 71–86

Van de Bunt L., Van der Heide U.A., Ketelaars M., De Kort G.A.P. and Jürgenliemk-Schulz I.M. 2006 Conventional, conformal and intensity-modulated radiation therapy treatment planning of external beam radiotherapy for cervical cancer: the impact of tumor regression *International Journal of Radiation Oncology, Biology and Physics* **64** 189–196

Van der Heide U.A., Kotte A.N.T.J., Dehnad H., Hofman P., Lagenijk J.J.W. and van Vulpen M. 2007 Analysis of fiducial marker-based position verification in the external beam radiotherapy of patients with prostate cancer *Radiotherapy and Oncology* **82** 38–45

Van der Wielen G.J., Mutanga T.F., Incrocci L., Kirkels W.J., Vasquez Osorio E.M., Hoogeman M.S., Heijmen B.J. and de Boer H.C. 2008 Deformation of prostate and seminal vesicles relative to intraprostatic fiducial markers *International Journal of Radiation Oncology, Biology and Physics* **72** 1604–1611

Van Herk M., Remeijer P., Rasch C. and Lebesque J.V. 2000 The probability of correct target dosage: dose-population histograms for deriving treatment margins in radiotherapy *International Journal of Radiation Oncology, Biology and Physics* **47** 1121–1135

Van Lin E.N., van der Vight L., Huizenga H., Kaanders J.H. and Visser A.G. 2003 Set-up improvement in head and neck radiotherapy using a 3D off-line EPID-based correction protocol and a customised head and neck support. *Radiotherapy and Oncology* **68** 137–148

Villeirs G.M., Van Vaerenbergh K., Vakaet L., Bral S., Claus F., De Neve W.J., Verstraete K.L. and De Meerleer G.O. 2005 Interobserver delineation variation using CT versus combined CT + MRI in intensity-modulated radiotherapy for prostate cancer *Strahlentherapie und Onkologie* **181** 424–430

Voet P.W., Dirkx M.L., Breedveld S., Fransen D., Levendag P.C. and Heijmen B.J. 2013 Toward fully automated multicriterial plan generation: a prospective clinical study *International Journal of Radiation Oncology, Biology and Physics* **85** 866–872

Webb S. 2001 *Intensity-modulated radiation therapy* Medical Sience Series (Bristol, UK: IOP Publishing Ltd)

Webb S. 2003 Use of quantitative index of beam modulation to characterize dose conformality: illustration by a comparison of full beamlet IMRT, few segment IMRT (fsIMRT) and conformal unmodulated radiotherapy *Physics in Medicine and Biology* **48** 2051–2062

Webb S. 2005 *Contemporary IMRT - Developing physics and clinical implementation* (London, UK: Institute of Physics Publishing) 1st edn.

Wells W.M.r., Viola P., Atsumi H., Nakajima S. and Kikinis R. 1996 Multi-modal volume registration by maximization of mutual information *Medical Image Analysis* **1** 35–51 Case Reports

Winkler A., Hefner A. and Georg D. 2005 Dose-response characteristics of an amorphous silicon epid *Medical Physics* **32** 3095–3105

Wolthaus J.W.H., Sonke J.J., Van Herk M., Belderbos J.S.A., Rossi M.M.G., Lebesque J.V. and Damen E.M.F. 2008 Comparison of different strategies to use four-dimensional computed tomography in treatment planning for lung cancer patients *International Journal of Radiation Oncology, Biology and Physics* **70** 1229–1238

Yang Y.M. and Bednarz B. 2013 Consistency evaluation between EGSnrc and Geant4 charged particle transport in an equilibrium magnetic field *Physics in Medicine and Biology* **58** N47–N58

Thesis publications

Bol G.H., Hissoiny S., Lagendijk J.J.W. and Raaymakers B.W. 2012 Fast online Monte Carlo-based IMRT planning for the MRI linear accelerator *Physics in Medicine and Biology* **57** 1375–1385

Bol G.H., Kotte A.N.T.J., Van der Heide U.A. and Lagendijk J.J.W. 2009 Simultaneous multi-modality ROI delineation in clinical practice *Computer methods and programs in Biomedicine* **96** 133–140

Bol G.H., Lagendijk J.J.W. and Raaymakers B.W. 2013 Virtual couch shift (VCS): accounting for patient translation and rotation by online IMRT re-optimization *Physics in Medicine and Biology* **58** 2989–3000

Bol G.H., Lagendijk J.J.W. and Raaymakers B.W. 2015 Compensating for the impact of non-stationary spherical air cavities on IMRT dose delivery in transverse magnetic fields *Physics in Medicine and Biology* **60** 755–768

Bol G.H., Van der Heide U.A., Kotte A.N.T.J., van Vulpen M. and Lagendijk J.J.W. 2008 MRI-compatible fiducial gold markers for prostate cancer patients in *Radiotherapy and Oncology proc. ESTRO 27, Göteborg, Sweden* vol. 88, suppl 2, nr 1171 p. S374

Bol G.H., Van der Heide U.A., Nederveen A.J., Kotte A.N.T.J. and Lagendijk J.J.W. 2006 Patient position verification using small IMRT fields *Medical Physics* **33** 2344–2353

Other publications

Bol G.H., Hissoiny S., Lagendijk J.J.W. and Raaymakers B.W. 2012 Fast monte-carlo based IMRT planning for the MRI linear accelerator (MRL) in *Radiotherapy and Oncology proc. ESTRO 31, Barcelona, Spain* vol. 103, suppl 1, nr OC-0553 p. S221

Bol G.H., Kotte A.N.T.J. and Lagendijk J.J.W. 2003 jVolumetool: an image evaluation, registration, and delineation system for radiotherapy *Physica Medica* **XIX** 80

Ceylan C., Van der Heide U.A., Bol G.H., Lagendijk J.J.W. and Kotte A.N.T.J. 2005 Assessment of rigid multi-modality image registration consistency using the multiple sub-volume registration (msr) method *Physics in Medicine and Biology* **50**

Kontaxis C., Bol G.H., Lagendijk J.J.W. and Raaymakers B.W. 2015 Towards adaptive IMRT sequencing for the MR-linac *Physics in Medicine and Biology* **60** 2493–2509

Moman M.R., Van der Heide U.A., Kotte A.N.T.J., van Moorselaar R.J., Bol G.H., Franken S.P. and van Vulpen M. 2010 Long-term experience with transrectal and transperineal implantations of fiducial gold markers in the prostate for position verification in external beam radiotherapy; feasibility, toxicity and quality of life *Radiotherapy and Oncology* **96** 38–42

Schippers M.G., Bol G.H., de Leeuw A.A., Van der Heide U.A., Raaymakers B.W., Verkooijen H.M. and Jurgenliemk-Schulz I.M. 2014 Position shifts and volume changes of pelvic and para-aortic nodes during IMRT for patients with cervical cancer *Radiotherapy and Oncology* **111** 442–445

Struikmans H., Wárlám-Rodenhuis C., Stam T., Stapper G., Tersteeg R.J., Bol G.H. and Raaijmakers C.P. 2005 Interobserver variability of clinical target volume delineation of glandular breast tissue and of boost volume in tangential breast irradiation. *Radiotherapy and Oncology* **76** 293–299

Van Roermund J.G., Hinnen K.A., Tolman C.J., Bol G.H., Witjes J.A., Bosch J.L., Kiemeney L.A. and van Vulpen M. 2011 Periprostatic fat correlates with tumour aggressiveness in prostate cancer patients *BJU International* **107** 1775–1779

Dankwoord

Het is lastig om iedereen met wie ik de afgelopen jaren heb samengewerkt persoonlijk te bedanken, dus bij dezen wil ik om te beginnen diegenen bedanken die verder in dit dankwoord niet genoemd worden. Mede door jullie (artsen, klinisch fysici, imaging fysici, fysisch medewerkers, versnellertechnici, ICT-ers, unithoofden, (specialistisch) laboranten, AIO's, ANIO's, OIO's, KLIFIO's, secretaressen, doktersassistenten, administratief medewerkers en schoonmakers) vind ik het fijn om op onze afdeling te werken en dat hoop ik dan ook na mijn promotie nog lang voort te zetten.

Als eerste wil ik Jan Lagendijk apart noemen in dit dankwoord. Jan, bedankt voor het vertrouwen dat je me gaf toen je me destijds hebt aangenomen. Ik heb veel bewondering voor je vooruitstrevendheid en optimisme. Dank voor alle vrijheid die ik van je kreeg om ideeën uit te laten groeien tot klinische toepassingen.

Beste Bas, ik vond het heel fijn om zo lang je kamergenoot te zijn geweest. Naast alle gezelligheid, vond ik het een voorrecht om mee te maken hoe je van arme hyperthermie AIO bent doorgestoomd naar je nieuw verworven professorschap. Ik vind het dan ook een eer om je eerste "echte" promovendus te zijn, en ik kijk uit naar alle MRL gerelateerde projecten die we de komende jaren gaan doen.

Uulke, bedankt voor je begeleiding van het eerste deel van dit proefschrift en voor het vertrouwen dat je gaf om eigen software in de kliniek in te zetten. De manier waarop je je voor alle facetten van het fysica werk inzet, waardeer ik zeer.

Alexis, we kennen elkaar al vanaf mijn afstudeerperiode, en sinds die tijd is het altijd prettig geweest om samen te werken. Dank voor de goede discussies rondom software en onderzoek, en de gezellige installatieprocedures net na vijven. Thijs en Nienke willen je ook graag bedanken voor al het speelgoed dat hun kant op gekomen is.

Sjoerd, fijn dat je de laatste jaren ons team bent komen versterken. Je veelzijdigheid ten aanzien van zo'n beetje alles waardeer ik enorm.

Bram, de afgelopen jaren hebben we veel en prettig op het gebied van de planning samengewerkt. Je kennis ten aanzien van dose engines en planoptimalisatie is onmisbaar geweest voor de ontwikkeling van MRLTP.

Ook het *i*MRL-team wil ik hier noemen: Christel, Eline, Gonda, Ilse en Lieke. Op weg naar de klinische introductie van de MRL!

Sara, thanks for correcting all the Dutch English sentences of the thesis, I really appreciate all your help.

Beste Heike, bedankt voor het maken van de omslag van dit proefschrift, het is prachtig geworden!

Beste Marco, fijn dat we al sinds de lagere school hele goede vrienden zijn en ik vind het dan ook erg leuk dat je paranimf bent tijdens de verdediging. Je humor en trouw waardeer ik zeer.

Mijn ouders, mijn zus en paranimf Ageeth, dank voor de onvoorwaardelijke steun en liefde die ik van jullie heb mogen ontvangen.

Lieve Tineke, jouw betekenis voor mijn leven is niet te beschrijven. Ik hoop dat we nog heel lang van elkaar, van Thijs, Nienke en alles wat Hij ons geeft, mogen genieten.

Gijs

Curriculum Vitae

Gijsbert Herman Bol was born on March 13th, 1979 in Meerkerk, The Netherlands. In 1997 he graduated from secondary school at Altena College in Sleeuwijk. From 1997 to 2001, he studied Medical Computer Science at Utrecht University. In September 2000, he started his graduation project at the radiotherapy department of the University Medical Center Utrecht. The title of his Master's thesis was "Manual Tissue Delineation and Safety Margins in Radiotherapy".

After graduating (cum laude), he continued working at the radiotherapy department as a computer scientist, where he implemented dedicated research and clinical software for treatment planning, tumor and OAR delineation, and data management. Besides this, he was given the opportunity to initiate his own research project, which resulted in this thesis.

Gijsbert continues working on various clinical and research projects, especially regarding automatic treatment planning and sequencing for conventional linacs and the MRL.

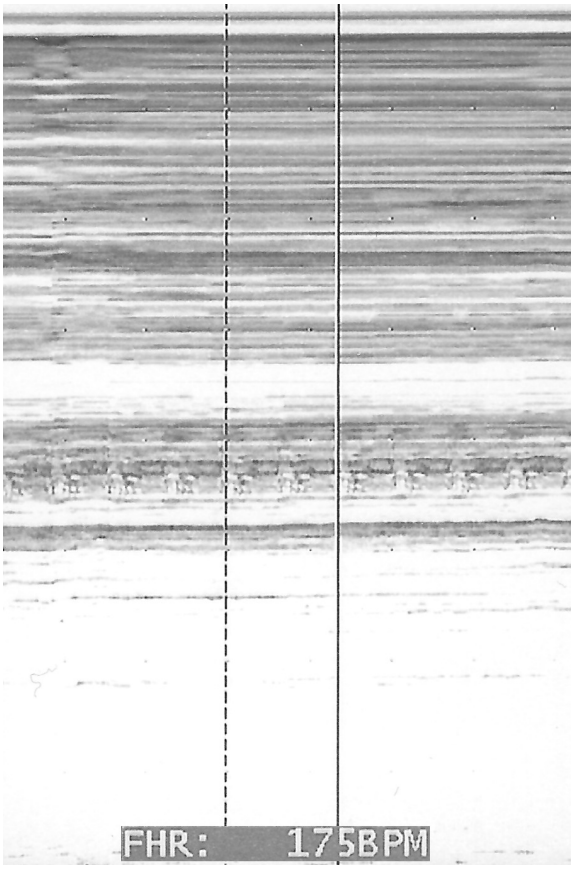
FHR: 175BPM